Performance Analysis of Segmentation Techniques for Iris Recognition System

A thesis submitted in partial fulfillment of the

requirements for the award of the Degree of

MASTER of ENGINEERING

in

ELECTRONICS AND COMMUNICATION ENGINEERING

Submitted by:

SURJEET SINGH

Roll No. 800861017

Under the guidance of:

Dr. KULBIR SINGH

Assistant Professor, ECED

DEPARTMENT OF ELECTRONICS AND COMMUNICATION ENGINEERING

THAPAR UNIVERSITY

PATIALA-147004, Punjab, INDIA.

June 2010

CERTIFICATE

I, Surjeet Singh hereby certify that the work which is being presented in this thesis entitled **"Performance Analysis of Segmentation Techniques for Iris Recognition System"** by me in partial fulfillment of the requirements for the award of degree of Master of Engineering in Electronics and Communication from Thapar University, Patiala is an authentic record of my own work carried under the supervision of Dr. Kulbir Singh.

The matter presented in this thesis has not been submitted in any University/Institute for the award of Master of Engineering.

(Surjeet Singh)
Signature of student

Date: 12/06/2010

This is certified that the above statement made by the candidate is correct to the best of my knowledge.

(Dr. Kulbir Singh)
(Supervisor)
Date: 12/06/2010

(Dr. A K Chatterjee)
Head of Department
ECED, Thapar University, Patiala

Date: 6.7.10

(Dr. R.K. Sharma)
Dean of Academic Affairs
Thapar University, Patiala

Date: 7/7/10

ACKNOWLEDGMENT

This report is completed with prayers of many and love of my family and friends. However, there are a few people that I would like to specially acknowledge and extend my heartfelt gratitude who have made the completion of this report possible .With the biggest contribution to this report; I would like to thank my guide **Dr. Kulbir Singh** had given me his full support in guiding me with stimulating suggestions and encouragement to go ahead in all the time of thesis work.

I am also thankful to **Dr. A. K. Chatterjee**, Head, Electronics and Communication Engineering department, for the providing us with adequate infrastructure in carrying the work.

At last but not the least my gratitude towards my parents, I would also like to thank God for not letting me down at the time of crisis and showing me the silver lining in the dark clouds.

(Surjeet Singh)

ABSTRACT

A biometric system provides automatic identification of an individual based on a unique feature or characteristic possessed by the individual. Iris recognition is regarded as the most reliable and accurate biometric identification system available.

Iris recognition systems capture an image from an individual's eye. The iris in the image is then segmented and normalized for feature extraction process. The performance of iris recognition systems highly depends on segmentation and normalization. For instance, even an effective feature extraction method would not be able to obtain useful information from an iris image that is not segmented or normalized properly. This thesis is to enhance the performance of segmentation and normalization processes in iris recognition systems to increase the overall accuracy.

The iris recognition system based on the Daugman's integrodifferential equation and Hough transform is implemented. The system is able to localise the circular iris and pupil region, occluding eyelids and eyelashes, and reflections. The extracted iris region was then normalised into a rectangular block with constant dimensions to account for imaging inconsistencies. Finally, the phase data from one-dimensional log-Gabor filters was extracted and quantised to four levels to encode the unique pattern of the iris into a bit-wise biometric template. The Hamming distance was employed for classification of iris templates, and two templates were found to match if a test of statistical independence was failed.

The previous iris segmentation approaches assume that the boundary of pupil is a circle. However, according to our observation, circle cannot model this boundary accurately. To improve the quality of segmentation, a novel active contour method based on Level Set Evolution without re-initialization is proposed to detect the irregular boundary of pupil. The method can successfully detect all the pupil boundaries in the CASIA database and increase the segmentation accuracy by almost 17%.

CONTENTS

List of Figures

List of Tables

Chapter 1: Introduction

Reliable personal recognition is critical to many processes. Nowadays, modern societies give higher relevance to systems that contribute to the increase of security and reliability, essentially due to terrorism and other extremism or illegal acts. In this context, the use of biometric systems has been increasingly encouraged by public and private entities in order to replace or improve traditional security systems. Basically, the aim is to establish an identity based on who the person is, rather than on what the person possesses or what the person remembers (e.g., an ID card or a password).

Pattern recognition - the act of taking in raw data and making an action based on the category of the pattern [1] - has been performed by humans for the last thousands of years in order to assure survival. In the computer science compass, it constitutes a field within the machine learning area and contributed in the last decades for the solution of many of our daily problems (e.g., character and speech recognition, medical diagnosis, DNA sequence identification, computer virus and spyware detection).

Biometrics can be seen from a pattern recognition perspective, where some physiological or physical subjects data is captured in order to output their respective identity. Considering the recent mandates of several governments for the nationwide use of biometrics, it constitutes a grand challenge for the field itself. Pattern recognition systems have never been tried at such large nor have dealt with such a wide use of sensitive personal information [2].

1.1 Biometrics

Searching for a definition of biometrics in both specialized and general information sources, leads to several variants, among which are:

- The study of automated methods for uniquely recognizing humans based upon one or more intrinsic physical or behavioral traits [3].

- A method of verifying an individual’s identity based on measurements of the individual’s physical features or repeatable actions where those features and/or actions are both unique to that individual and measurable [4].

- Biometrics is the science and technology of measuring and analyzing biological data. In information technology, biometrics refers to technologies that measure and analyze human body characteristics, such as fingerprints, eye retinas and irises, voice patterns, facial patterns and hand measurements, for authentication purposes [5].

- Biometrics is the science of measuring physical properties of living beings using suitable body characteristics [6].

- Any automatically measurable, robust and distinctive physical characteristic or personal trait that can be used to identify an individual or verify the claimed identity of an individual [7]

As can be seen, notions of biological, measuring and recognition are common to any definition, and point to the most relevant characteristics behind the term. From our viewpoint, biometrics can be regarded as the automated measurement and enumeration of biological characteristics, in order to obtain a plausible quantitative value that, with high confidence, can distinguish between individuals.

Although less automatized, biometrics has been used - at least - for centuries. In the 14th century, the Portuguese writer João de Barros reported its first known application. He wrote that Chinese merchants stamped children's palm print and footprints on paper with identification purposes [3]. Also, it is believed that the ancient civilizations of Egypt and China performed some type of biometric recognition.

In the western world, until the late 1800s the automatic recognition of individuals was largely done using "photographic memory". In 1883, the French police and anthropologist Alphonse Bertillon developed an anthropometric system, known as Bertillonage [8], to fix the problem of identification of convicted criminals. As illustrated by Figure 1.1, this was a quite complex procedure that could take up to twenty minutes and is considered the first scientific system widely used to identify criminals [3]. Its basis was the measurement of certain lengths and widths of the head and body and the recording of individual markings, such as tattoos and scars. However this system's faded when it was discovered that some people share the same measures and several people could be treated as one.

The failure of Bertillonage motivated the use of fingerprinting, which is presently almost standardized worldwide. In 1880, the British scientific journal Nature published an article by Henry Faulds and William James describing the uniqueness and permanence of fingerprints. This motivated the design of the first elementary fingerprint recognition system by Sir Francis Galton and improved by Sir Edward R. Henry. Having quickly disseminated, the first fingerprint system in the United States was inaugurated by the New York State Prison Department in 1903 and the first known convicted due to fingerprint evidences was reported in 1911 [9].

Presently, due to increasing concerns associated with security and the war on terrorism, biometrics has considerably increased its relevance. It has moved from a single and almost standardized trait (fingerprint) to the use of more than ten distinct traits. An increasing number of companies, either private or governmental, either with military or civil purposes, invest an enormous amount of human and financial resources into the development of biometric systems. New methods are constantly being proposed and the prices for the hardware and the software technology are continuously falling, making the application of biometrics systems more feasible to low and mid-level budgets. Furthermore, biometrics technology can be seen as a return to the ways of nature, since from centuries humans perform its distinction based in physical and physiological features, such as the facial structure or voice.

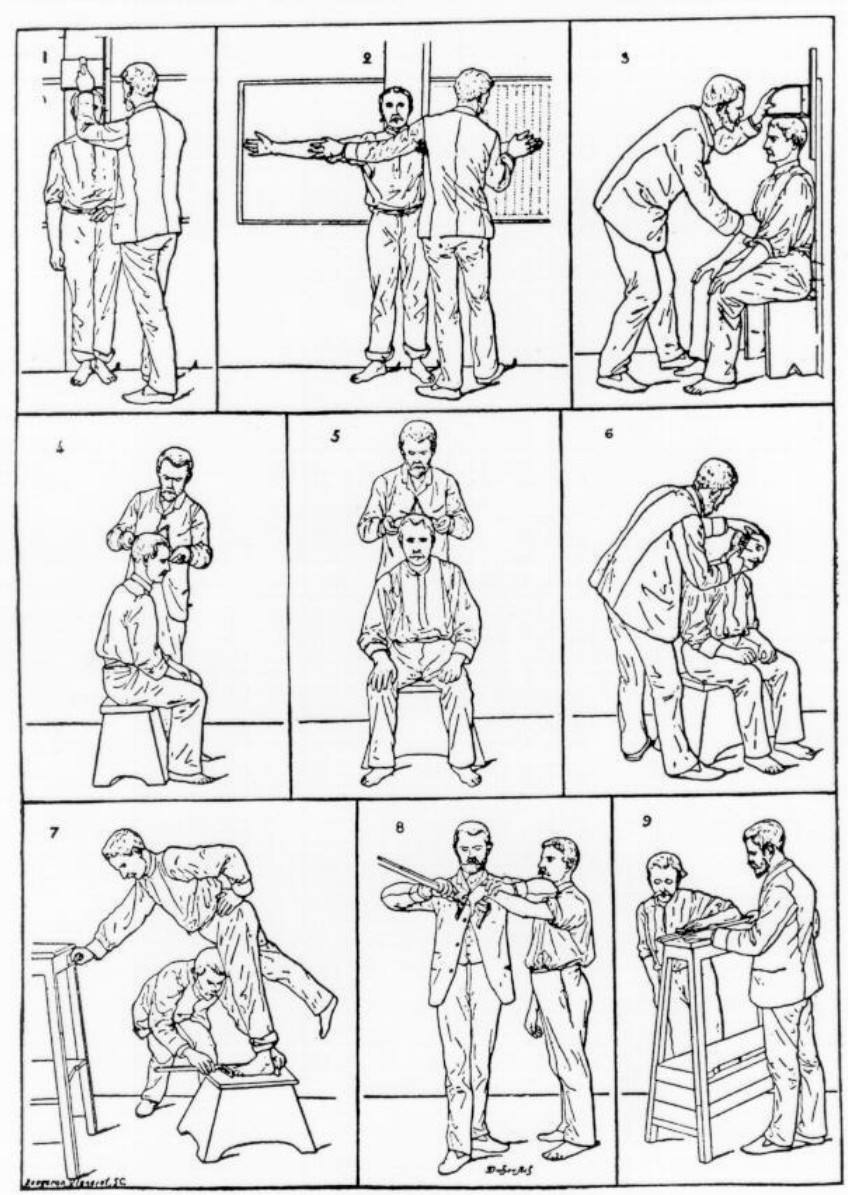

Figure 1.1: Anthropometric system by Alphonse Bertillon [8].

1.2 Modes of Functioning

Independently of the used trait, the biometric applications follow the procedure illustrated in Figure 1.2. The process begins by the data capturing, where the biometric sample is acquired. Next, through the feature extraction a biometric signature is created, that is further compared with a specific or several biometric signatures registered in the database. These are commonly designated as biometric templates and were collected during the enrolment process and correspond to a verified subject identity. If the comparison between biometric signatures has enough similarity, it is assumed that both of these were extracted from the same person, otherwise, they must have been extracted from different persons.

The number of comparisons between the biometric sample and templates determines basic distinctions among the two modes of performing biometric recognition: verification and identification.

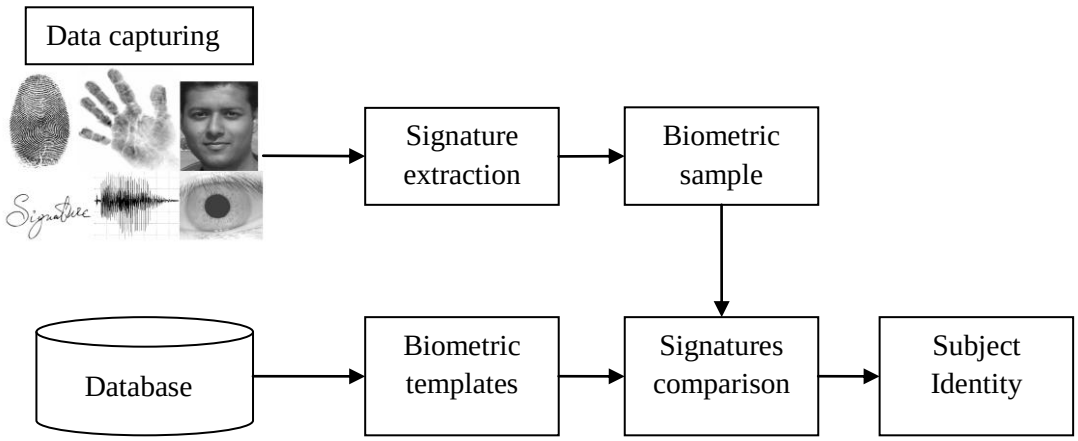

Figure 1.2: Typical stages of a biometric recognition process.

In the verification mode, also named as positive recognition, the system verifies the authenticity of a claimed enrolled identity, trying to answer the question: is this person who he/she claims to be? This requires that, together with the biometric sample, the subject's id must be given to the recognition algorithm. Further, the comparison between the biometric template correspondent to that identity and the sample is performed. If the similarity is high enough, the claimed identity is accepted, meaning that both biometric signatures were extracted from the same person. Otherwise, the identity is denied, meaning that the enrolled and the sample signatures were extracted from different subjects.

The identification mode, often named as negative recognition, tries to answer the question: who is this person?, or sometimes: is this person in the database? After acquiring the required data and extracting the biometric sample, a comparison is made with the N enrolled identities, in order to find the identity from which the sample was collected. In this mode, it is usual to output a list of the k most probable identities of a biometric sample.

1.3 Classification of Biometric Systems

Biometric systems can be classified according to six perspectives, as a function of the characteristics of the recognition procedure itself:

Overt / covert: If the user is aware about the acquisition of his biometric data, the application is defined as overt; otherwise, is defined as covert. This is clearly one of the most concerning characteristics of a biometric system, regarding the privacy issue.

Habituated / non-habituated: When the majority of the people that interacts with the biometric system are every-day users, the recognition is performed in the habituated mode. If the average frequency of use from each user is low, the recognition is performed in the non-habituated mode. This is relevant to the degree of cooperation and training demanded from the users.

Attended / non-attended: If the user is observed and guided by supervisors during the process, the biometric recognition is performed attended; if not, the use is considered non-attended. Obviously, the easy-of-use of the recognition system is much more relevant in the non-attended mode.

Standard / non-standard environment: When all the conditions can be controlled and the recognition takes place indoors within constrained conditions, it is considered that the recognition is performed within a standard environment; if not, the use is called in non-standard environment.

Public / private: If the users are not employees of the organization that owns the recognition system, the application is public; if the users are employees, the application is called private.

Open / closed: If the system uses completely proprietary formats, the application is considered closed. Otherwise, when the system is able to exchange data with others, it is called open and, once again, privacy and legal issues should be addressed.

1.4 Biometric Traits

This section briefly discusses common traits that are presently used for biometric purposes. Although there is some discussion about the potential use of other traits as biometric basis, the presented traits are those with higher acceptability by the research community and have commercial applications based in it, which increases its credibility in the biometric compass.

1.4.1 Fingerprints

The patterns of friction ridges and valleys on an individual's fingertips are unique to that individual. For decades, law enforcement has been classifying and determining identity by matching key points of ridge endings and bifurcations. Fingerprints are unique for each finger of a person including identical twins. One of the most commercially available biometric technologies, fingerprint recognition devices for desktop and laptop access are now widely available from many different vendors at a low cost. With these devices, users no longer need to type passwords – instead, only a touch provides instant access.

1.4.2 Face Recognition

The identification of a person by their facial image can be done in a number of different ways such as by capturing an image of the face in the visible spectrum using an optical camera or by using the infrared patterns of facial heat emission. Facial recognition in visible light typically model key features from the central portion of a facial image. Using a wide assortment of cameras, the visible light systems extract features from the captured image(s) that do not change over time while avoiding superficial features such as facial expressions or hair. Several approaches to modeling facial images in the visible spectrum are Principal Component Analysis, Local Feature Analysis, neural networks, elastic graph theory, and multi-resolution analysis. Some of the challenges of facial recognition in the visual spectrum include reducing the impact of variable lighting and detecting a mask or photograph. Some facial recognition systems may require a stationary or posed user in order to capture the

image, though many systems use a real-time process to detect a person's head and locate the face automatically. Major benefits of facial recognition are that it is non-intrusive, hands-free, continuous and accepted by most users. Facial recognition uses distinctive facial features, including upper outlines of eye sockets, areas around cheekbones, the sides of the mouth and the location of the nose and eyes. Most technologies avoid areas of the face near the hairline so that hairstyle changes won't affect recognition.

1.4.3 Hand and Finger Geometry

These methods of personal authentication are well established. Hand recognition has been available for over twenty years. To achieve personal authentication, a system may measure either physical characteristics of the fingers or the hands. These include length, width, thickness and surface area of the hand. One interesting characteristic is that some systems require a small biometric sample (a few bytes). Hand geometry has gained acceptance in a range of applications. It can frequently be found in physical access control in commercial and residential applications, in time and attendance systems and in general personal authentication applications. This method relies on devices that measure the length and angles of individual fingers. Although more user-friendly than retinal scans, it's still cumbersome.

1.4.4 Palmprint

Similarly to the widely used fingerprints, the palms of the human hands contain unique patterns of ridges and valleys. Since a palm is larger then a finger, a palmprint is expected to be even more distinguishable than a fingerprint.

Palmprint scanners need to capture a larger area with similar quality as fingerprint scanners, which makes them more expensive. Typically, the analysis of the palm’s principal lines, wrinkles, and textures is performed. These line structures are stable over the human lifetime and normally people do not feel uneasy to have their palmprint images captured.

Therefore, palmprint recognition offers promising future for medium-security access control system. Although this is not as stabilized and matured as the fingerprint technology, several research studies have been made with the purpose of extracting higher discriminating features from the palmprint information. Presently, there are two popular approaches to palmprint recognition. One transforms palmprint images into specific transformation domains and apply texture-based analysis methods (Gabor filters, wavelets decompositions). The other approach applies a technology close to the one used for fingerprint: extract the main lines and creases from the palm and further perform the comparison between the minutia information (e.g., through graph matching).

Compared to other biometric traits, the facts that a higher level of cooperation is demanded to users and the required physical contact between the users and the capturing device, should be regarded as disadvantages. Also, the fact that the human hand is a fundamental tool for the majority of the people increases the probability of physical damages or diseases.

1.4.5 Iris Recognition

This recognition method uses the iris of the eye which is the colored area that surrounds the pupil. Iris patterns are thought unique. The iris patterns are obtained through a video-based image acquisition system. Iris scanning devices have been used in personal authentication applications for several years. Systems based on iris recognition have substantially decreased in price and this trend is expected to continue. The technology works well in both verification $(1:1)$ and identification $(1:N)$ modes (in systems performing one-to-many searches in a database). Current systems can be used even in the presence of eyeglasses and contact lenses. The technology is not intrusive. It does not require physical contact with a scanner. Iris recognition has been demonstrated to work with individuals from different ethnic groups and nationalities.

1.4.6 Retina Recognition

The human retina is a thin tissue compose d of neural cells that is located in the posterior portion of the eye. Because of the complex structure of the capillaries that supply the retina with blood, each person's retina is unique. The network of blood vessels in the retina is so complex that even identical twins do not share a similar pattern. Although retinal patterns may be altered in cases of diabetes, glaucoma, retinal degenerative disorders or cataracts, the retina typically remains unchanged from birth until death. Due to its unique and unchanging nature, the retina appears to be the most precise and reliable biometric. Advocates of retinal scanning have concluded that it is so accurate that its error rate is estimated to be only one in a million. A biometric identifier known as a retinal scan is used to map the unique patterns of a person's retina. The blood vessels within the retina absorb light more readily than the surrounding tissue and are easily identified with appropriate lighting. A retinal scan is performed by casting an undetectable ray of low-energy infrared light into a person’s eye as they look through the scanner's eyepiece. This beam of light outlines a circular path on the retina. Because retinal blood vessels are more sensitive to light than the rest of the eye, the amount of reflection fluctuates. The results of the scan are converted to computer code and stored in a database.

1.4.7 Vein Geometry:

As with irises and fingerprints, a person's veins are completely unique. Twins don't have identical veins, and a person's veins differ between their left and right sides. Many veins are not visible through the skin, making them extremely difficult to counterfeit or tamper with. Their shape also changes very little as a person ages. To use a vein recognition system, you simply place your finger, wrist, palm or the back of your hand on or near the scanner. A camera takes a digital picture using near-infrared light. The hemoglobin in your blood absorbs the light, so veins appear black in the picture. As with all the other biometric types, the software creates a reference template based on the shape and location of the vein structure. Scanners that analyze vein geometry are completely different from vein scanning tests that happen in hospitals. Vein scans for medical purposes usually use radioactive

particles. Biometric security scans, however, just use light that is similar to the light that comes from a remote control.

1.4.8 Keystroke

The technology, which measures the time for which keys are held down, as well as the length between strokes, takes advantage of the fact that most computer users evolve a method of typing which is both consistent and idiosyncratic – especially for words used frequently such as a user name and password. When registering, the user types his or her details nine times so that the software can generate a profile. Future login attempts are measured against the profile which, the current claim is that it can recognize the same user's keystrokes with 99 per cent accuracy, using what is known as a "behavioral biometric."

1.4.9 Signature

Biometric signature recognition systems will measure and analyze the physical activity of signing, such as the stroke order, the pressure applied and the speed. Some systems may also compare visual images of signatures, but the core of a signature biometric system is behavioral, i.e. how it is signed rather than visual, i.e. the image of the signature.

1.4.10 Voice or Speech

Voice or speech recognition is the ability of a machine or program to receive and interpret dictation, or to understand and carry out spoken commands. Strictly speaking, voice is also a physiological trait because every person has a different pitch, but voice recognition is mainly based on the study of the way a person speaks, commonly classified as behavioral.

1.4.11 Cognitive Biometrics

Recently, a new trend has been developed that merges human perception to computer database in a brain-machine interface. This approach has been referred to as cognitive biometrics. Cognitive biometrics is based on specific responses of the brain to stimuli, which could be used to trigger a computer database search. Currently, cognitive biometrics systems are being developed to use brain response to odour stimuli facial perception and mental performance for search at ports and high security areas. These systems are based on use of functional transcranial Doppler (fTCD) and functional transcranial Doppler spectroscopy (fTCDS) to obtain brain responses, which are used to match a target odor, a target face or target performance profile stored in a computer database. Thus, the precision of human perception provides the data to match that stored in the computer with improve sensitivity of the system.

1.5 Factors Influencing Biometric Traits

According to Matyas Jr. and Riha [10], every biometric system depends on the features, whether genotypic or phenotypic it is based on. Similarly to Daugman [11], authors divide the biometric traits into two types. Genotypic refers to the traits that are defined by the genetic makeup of the individual and do not change over time. Phenotypic refers to the actual

expression of a feature, through the interaction of genotype, its development and surrounding environment.

According to these, all biometric traits can be placed somewhere along the continuous line with genotypic and phenotypic endpoints, with some traits placed firmly at either extreme (e.g., signature dynamics at the phenotypic extreme) and others somewhere in the middle (e.g., face). The origin of the biometric traits is relevant due to its influence on the systems' error rates. For instance, the dynamics of the phenotypic features over time strongly increases the false rejection rates, while the fact that identical twins share their genetic code sets limits upon the false acceptances.

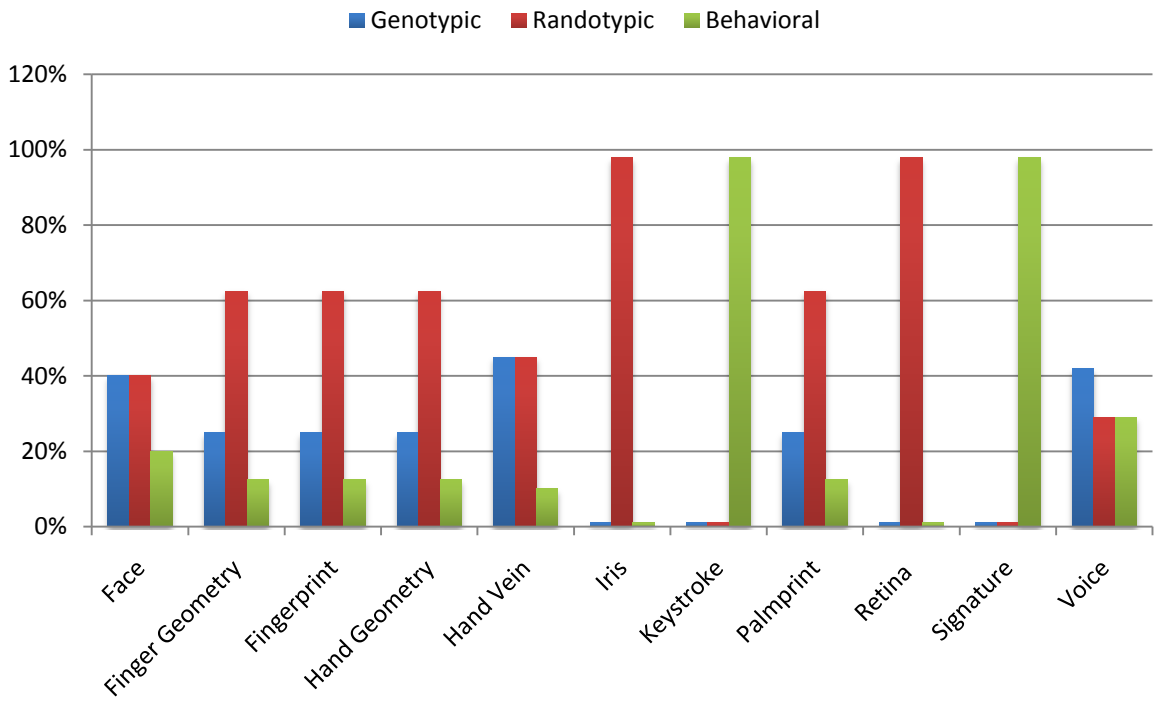

Figure 1.3: Factors of influence of the biometric traits.

Fried [12] and A. Bromba [6] classified the origin of the biometric traits into three different types: genotypic are traits that are defined by the genetic individual constitution, randotypic are those formed early in the development of the embryo, and claimed that the shape of these are distributed randomly through the entire population. Usually the latter are considered the most valuable features for biometric purposes due to the necessity of absolute uniqueness feature sets per subject. Finally, behavioral traits are those aspects that a subject develops through training or repeated learning. The analysis of these variants enabled us to establish a parallelism between the phenotypic and randotypic-behavioral trait types. The latter can be seen as two sub classes of the former and specify the type of interaction between subject and environment. If it was formed with subject conscientiousness, it is behavioral, otherwise is randotypic.

1.6 Comparison Between the Most Common Biometrics Traits

Following the proposal of Jain et al. [13], biometric systems can be evaluated regarding seven parameters: uniqueness, universality, permanence, collectability, performance, acceptability and circumvention.

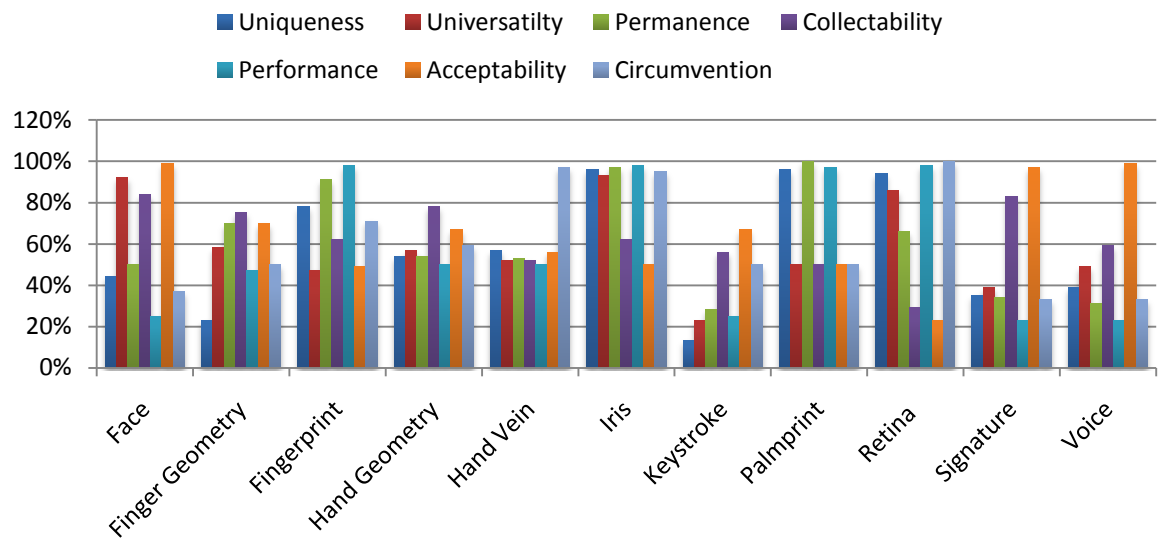

Figure 1.4: Comparison between the most common biometric traits (adapted and averaged from [14], [15], [6], [16], [17], [18] and [19]).

The uniqueness, often designated as accuracy, distinctiveness or singleness, is probably the most relevant characteristic of a biometric trait. It measures the degree of dissimilarity of the trait between individuals and its capacity of being separable. This feature strongly determines the probability of false acceptances by the system. Universality measures the scope of the trait, the number of people where it occurs. Obviously, the optimal biometric trait should occur in as many people as possible. Permanence is the quality of being immutable over time, measuring the probability of the biometric trait suffering significant changes over lifetime. This parameter has strong impact in the false rejection rates of the system. Collectability or measurability, is the characteristic that expresses the technical and humane easiness in the capture of the relevant trait information. This value plays a role in the users' comfort, which can easily dictate between the biometric system adoption or rejection. The performance as to do with the time required to perform the biometric recognition, once the data is captured. It is relevant in order to distinguish between the computational requirements of the recognition process. Acceptability or intrusiveness, is a measure related with socio-cultural users' concerns, as well as with privacy concerns associated with the data capturing. Finally, the circumvention measures how easy it is to counterfeit the system, which has high relevance in the security compass.

Figure 1.4 contains a comparison between the most common biometric traits. The classification of each item is denoted in percentage and "100%" and "0%" correspond respectively to the best and worst values in any of the items. Each value was obtained

through averaging and weighting of the classifications proposed in [14], [15], [6], [16], [17], [18] and [19].

For the purposes of our work, one of the most important features is the ability to perform covert recognition, which can be performed by the fingerprint, face, iris and palmprint. Among these, iris must be enhanced, as it provides higher uniqueness and circumvention values.

Apart from being the biometric trait with highest average value between the seven analyzed parameters (84.42%), its simultaneous high levels for uniqueness, permanence, universality and circumvention turned the iris into the most appropriate for our work and a natural choice towards the biometric iris recognition.

1.7 Thesis objective

The objectives of thesis are:

- To study about iris anatomy, different techniques of iris segmentation, normalization feature extraction and comparison.
- Segmentation (locating the iris region in an eye image) is to be done by implementing Daugman's integrodifferential equation, Hough transform and active contour based methods.
- Normalisation (creating a dimensionally consistent representation of the iris region) is to be done by using Daugman's rubber sheet model.
- Feature encoding (creating a template containing only the most discriminating features of the iris), will be done using one-dimensional log-Gabor filters.
- To implement prominent iris recognition algorithms in MATLAB®. The system is to be composed of a number of sub-systems, which correspond to each stage of iris recognition. The input to the system will be an eye image, and the output will be an iris template, which will provide a mathematical representation of the iris region.

1.8 Thesis Layout

The thesis has been organized in the following chapters.

Chapter 2 Literature Survey: This chapter gives an overview of eye & iris anatomy, iris recognition system, segmentation, normalization, feature encoding, feature matching and some prominent iris recognition methods.

Chapter 3 Segmentation and Normalization: This chapter discuss in detail Daugman's, Hough transform and discrete circular active contour segmentation methods. Normalization methods based on Daugman's model, Image registration and Virtual circles is also discussed with emphasis on Daugman's rubber sheet model.

Chapter 4 Feature Encoding and Matching: Different feature encoding algorithms are discussed with emphasis on 1D Log-Gabor filters. Feature matching based on Hamming distance is also discussed in detail.

Chapter 5 Results: The outcome of various segmentation techniques, normalization method, feature encoding and matching are compared.

Chapter 6 Conclusion: Enlists the important conclusion of the thesis.

Chapter 2: Literature Survey

2.1 Eye and Iris Anatomy

In this sub-section we start with the description of the human eye anatomy, followed by a highly detailed description of the iris, which is the most relevant part of the eye for the purposes of our work.

2.1.1 Eye Anatomy

Figure 2.1 schematizes the most relevant parts of the human eye. As with the majority of the mammals, the eye is roughly globular in shape and hollow and can be divided into two main segments anterior and posterior which are surrounded by a leathery envelope that acts as a protection: the sclera. This is a tough and fibrous tissue consisting of highly compacted and interweaved fibers and bands. When seen from the front, sclera is commonly, and incorrectly, referred to as the white of the eye.

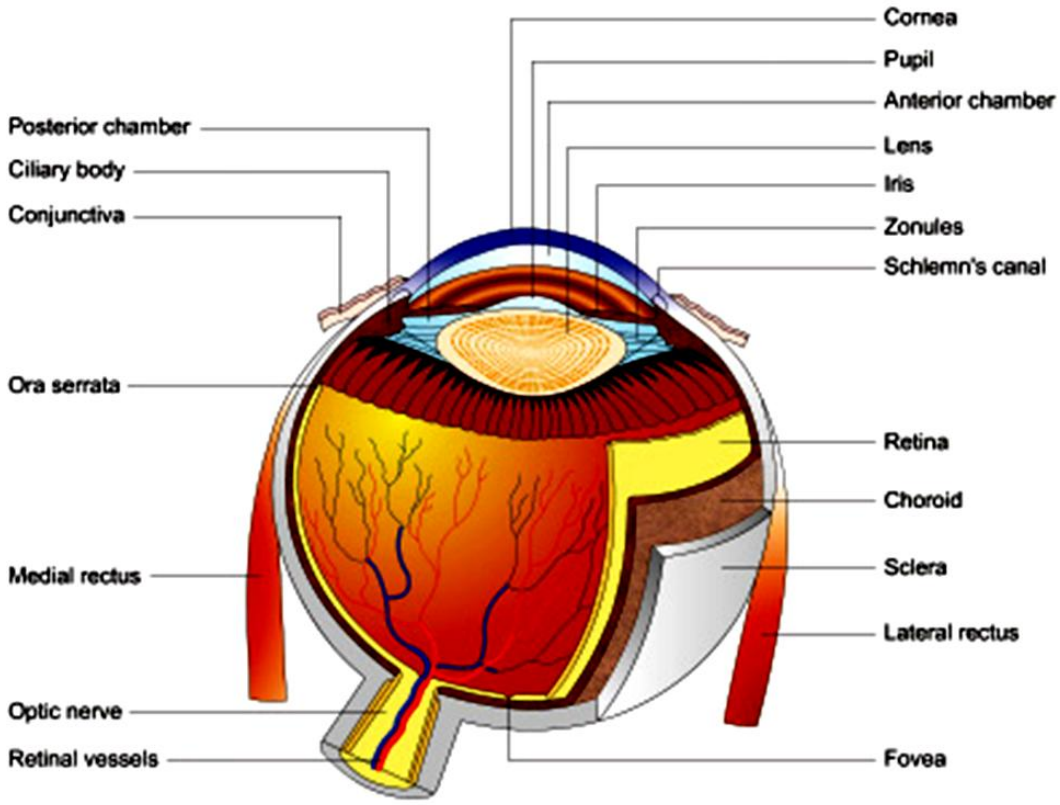

Figure 2.1: Anatomy of the human eye. [20]

Regarding the anterior eye segment, it extends internally from the anterior hyaloid face forward and is externally demarcated by the limbus. It includes the structures in front of the vitreous humor: the cornea, iris, ciliary body and lens. The cornea acts as a window at the front of the eye and provides about 85% of the focusing power of the eye. It is made up of a tissue similar to that of sclera, with the relevant exception of having no blood vessels. Just beneath the cornea is a fluid-filled space called the anterior chamber, which bathes the whole

of the anterior segment providing nourishment and removal products to the lens and cornea. The ciliary body is the source of the above mentioned fluid and houses the muscular fibers that enable the eye to focus. Overlying the lens, there is a structure with an opening in the whole: the iris. It is made of an elastic tissue and its function is to control the amount of light that enters the iris whole: the pupil. Behind the iris is the lens, which role consists in assuring that the light rays some to a sharp focus on the retina.

The posterior eye segment comprises the back two-thirds of the eye and includes the vitreous humor, retina, choroid and optic nerve. The first is the clear aqueous solution that fills the space between the lens and the retina, which is a thin layer of nervous tissue supplied with oxygen and cleaned by the choroid - that is responsible for gathering the light and perform its conversion to the electrical signals that are sent through the optic nerve to the brain. This process gives us the sense of light and the ability to see and interpret shapes, colours and dimensions.

2.1.2 Iris Anatomy

The iris is a thin, circular structure located anterior to the lens, often compared to a diaphragm of an optical system. The centre aperture, the pupil, actually is located slightly nasal and inferior to the iris centre. Pupil size regulates retinal illumination. The diameter can vary from 1 mm to 9 mm depending on lighting conditions. The pupil is very small (miotic) in brightly lit conditions and fairly large (mydriatic) in dim illumination. The average diameter of the iris is 12 mm, and its thickness varies. It is thickest in the region of the collarette, a circular ridge approximately 1.5 mm from the pupillary margin. This slightly raised jagged ridge was the attachment site for the fetal pupillary membrane during embryologic development. The collarette divides the iris into the pupillary zone, which encircles the pupil, and the ciliary zone, which extends from the collarette to the iris root (Figure 2.2). The color of these two zones often differs.

The pupillary margin of the iris rests on the anterior surface of the lens and, in profile, the iris has a truncated cone shape such that the pupillary margin lies anterior to its peripheral termination, the iris root (Figure 2.3). The root, approximately 0.5 mm thick, is the thinnest part of the iris and joins the iris to the anterior aspect of the ciliary body. The iris divides the anterior segment of the globe into anterior and posterior chambers, and the pupil allows the aqueous humor to flow from the posterior into the anterior chamber with no resistance.

2.2 Histologic Features of Iris

The iris can be divided into four layers: (1) the anterior border layer, (2) stroma and sphincter muscle, (3) anterior epithelium and dilator muscle, and (4) posterior epithelium.

2.2.1 Anterior Border Layer

The surface layer of the iris, the anterior border layer, is a thin condensation of the stroma. In fact, some do not consider this to be a separate layer. It is composed of fibroblasts, pigmented melanocytes, and collagen fibrils. The highly branching processes of the cells interweave to

form a meshwork in which the fibroblasts are on the surface and the melanocytes are located below. The thickness of the melanocyte layer may vary throughout the iris, with accumulations of melanocytes forming elevated frecklelike masses, evident in the anterior border layer. The density and arrangement of the meshwork differ among irises and are contributing factors in iris color. The collagen fibrils are arranged in radial columns that are seen easily as white fibers in light-colored irises.

The anterior border layer is absent at the oval-shaped iris crypts. Near the root, extensions of this layer form finger-shaped iris processes that can attach to the trabecular meshwork. The number of these processes varies, but they usually do not impede aqueous outflow. The anterior border layer ends at the root.

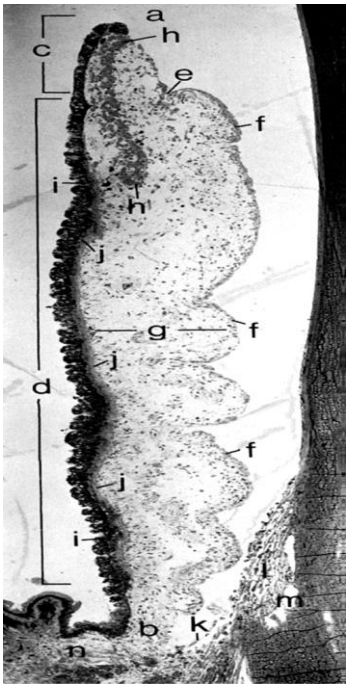

Figure 2.2: Light micrograph of the iris and anterior chamber. The cornea, anterior chamber angle, trabecular meshwork, canal of Schlemm, and part of the ciliary body are included. Anterior and posterior iris contraction furrows are accentuated by slight dilation of pupil. Pupil and pupillary ruff are at a, and iris root is at b. Pupillary portion of iris is at c, and ciliary portion is at d. Collarette (e) and minor arterial circle of the iris lie at the junction of these two portions. Cellular anterior border layer (f) is distinct from loosely arranged stromal tissue (g). Sphincter muscle lies in the stroma (h). Posterior iris shows posterior (i) and anterior (j) epithelium; the latter forms the dilator muscle. Anterior chamber angle shows part of a uveal band (k). Trabecular meshwork (l) and canal of Schlemm (m) lie external to chamber angle. Ciliary body and its muscle are posterior to iris (n). [21]

2.2.2 Iris Stroma and Sphincter Muscle

The connective tissue stroma is composed of pigmented and nonpigmented cells, collagen fibrils, and extensive ground substance. The pigmented cells include melanocytes and clump cells, whereas the nonpigmented cells are fibroblasts, lymphocytes, macrophages, and mast cells. Although melanocytes and fibroblasts have many branching processes, the cells are widely spaced in the stroma, so their branches do not form a meshwork. Clump cells are large, round, darkly pigmented cells and are variously described as “displaced

neuroectodermal cells" or more likely "altered macrophages." Clump cells usually are located in the pupillary portion of the stroma, often near the sphincter muscle.

The iris arteries are branches of a circular vessel, the major circle of the iris, located in the ciliary body near the iris root. The iris vessels usually follow a radial course from the iris root to the pupil margin. These vessels were historically thought to have an especially thick tunica adventitia and have been called "thick walled blood vessels." Improved histologic staining has shown, however, that the bundles of collagen fibrils encircling the vessels are continuous with the collagen network of the stroma and not part of the actual vessel wall. This fibril network anchors the vessels in place and protects them from kinking and compression during extensive iris movement in miosis and mydriasis. An incomplete circular vessel, the minor circle of the iris, is located in the iris stroma in the region of the collarette and is a remnant of embryologic development. The iris capillaries are not fenestrated and form part of the blood-aqueous barrier. The iris stroma is continuous with the stroma of the ciliary body.

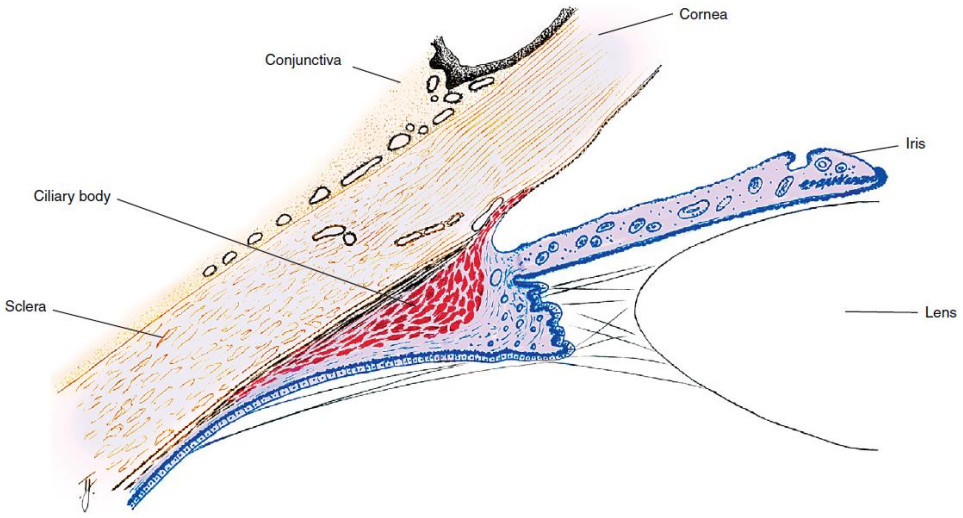

Figure 2.3: Periphery of anterior segment of the globe. [21]

The sphincter muscle lies within the stroma and is composed of smooth-muscle cells joined by tight junctions. As its name implies, the sphincter is a circular muscle 0.75 to 1 mm wide, encircling the pupil and located in the pupillary zone of the stroma (Figure 2.4). The sphincter muscle is anchored firmly to adjacent stroma and retains its function even if severed radially. Contraction of the sphincter causes the pupil to constrict in miosis. The muscle is innervated by the parasympathetic system.

2.2.3 Anterior Epithelium and Dilator Muscle

Posterior to the stroma are two layers of epithelium. The first of these, the epithelial layer lying nearest to the stroma, is the anterior iris epithelium, which is composed of the unique myoepithelial cell. The apical portion is pigmented cuboidal epithelium joined by tight junctions and desmosomes, whereas the basal portion is composed of elongated, contractile,

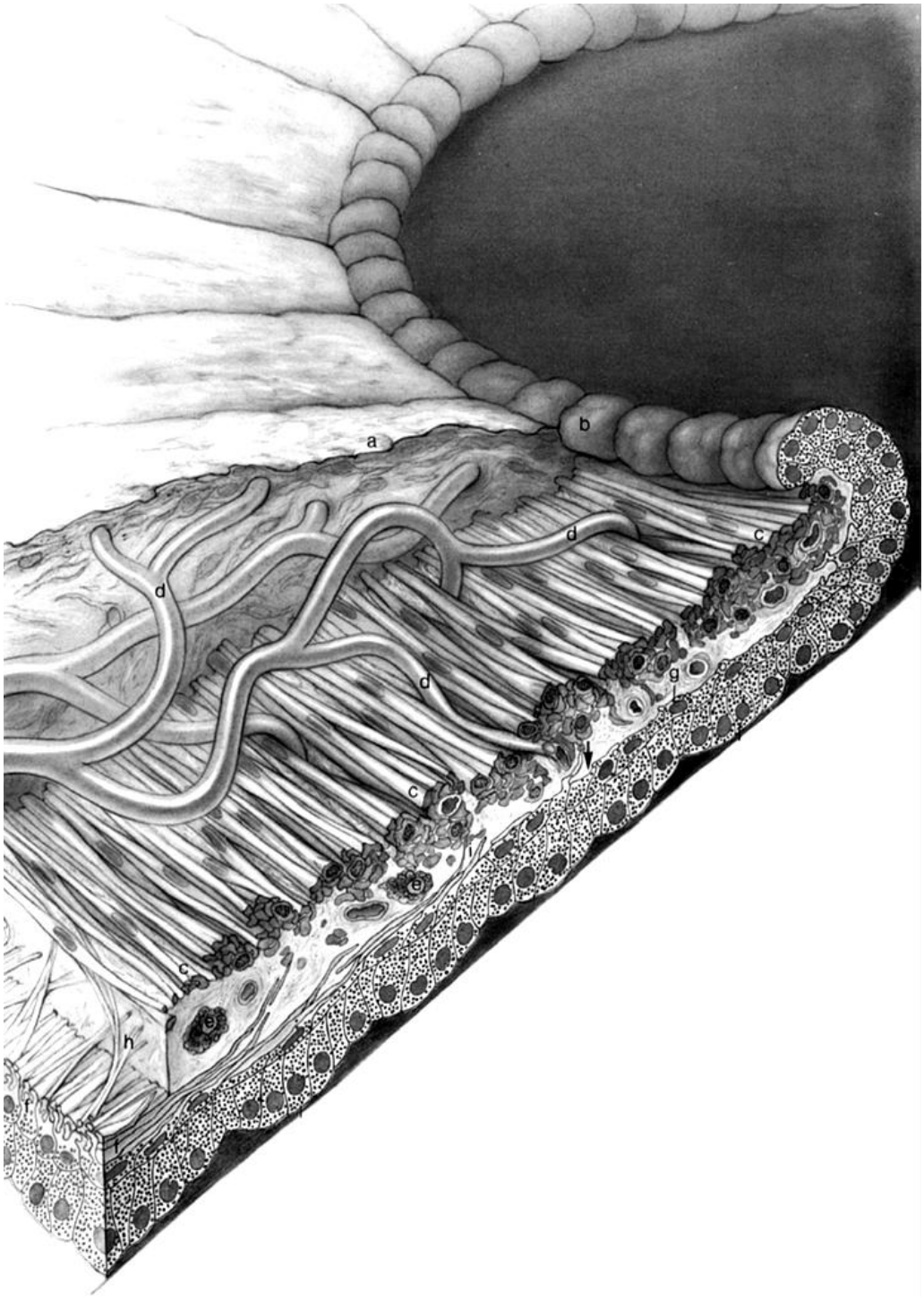

Figure 2.4: Pupillary portion of the iris. Dense cellular anterior border layer (a) terminates at pigment ruff (b) in pupillary margin. Sphincter muscle is at c. The arcades (d) from the minor circle of iris extend toward pupil and through sphincter muscle. Sphincter muscle and iris epithelium are close to each other at the pupillary margin. Capillaries, nerves, melanocytes, and clump cells (e) are found within and around the muscles. The three to five layers of dilator muscle (f) gradually diminish in number until they terminate behind midportion of sphincter muscle (arrow), leaving low, cuboidal epithelial cells (g) to form the anterior epithelium of papillary margin. Spurlike extensions from dilator muscle form Michel's spur (h) and Fuchs' spur (i), which extend anteriorly to blend with sphincter muscle. Posterior epithelium (j) is formed by tall columnar cells with basally located nuclei. Its apical surface is contiguous with apical surface of anterior epithelium. [21]

smooth muscle processes. The muscle fibers extend into the stroma, forming three to five layers of dilator muscle joined by tight junctions.

The dilator muscle is present from the iris root to a point in the stroma below the midpoint of the sphincter. Near the termination of the dilator muscle, small projections insert into the stroma or, more accurately, into the sphincter (Figure 2.4). Because the fibers are arranged radially, contraction of the dilator muscle pulls the pupillary portion toward the root, thereby enlarging the pupil in mydriasis. The dilator is sympathetically innervated.

The anterior epithelium continues to the papillary margin as cuboidal epithelial cells, and the epithelium continues posteriorly as the pigmented epithelium of the ciliary body.

2.2.4 Posterior Epithelium

The second epithelial layer posterior to the stroma is the posterior iris epithelium, a single layer of heavily pigmented, approximately columnar cells joined by tight junctions and desmosomes. In the periphery the posterior iris epithelium begins to lose its pigment as it continues into the ciliary body as the nonpigmented epithelium. A thin basement membrane covers the basal aspect of this cellular layer, lining the posterior chamber. The anterior and posterior iris epithelial layers are positioned apex to apex, a result of events during embryologic development. Apical microvilli extend from both surfaces, and desmosomes join the two apical surfaces. The epithelial cells curl around from the posterior iris to the anterior surface at the papillary margin, forming the pigmented pupillary ruff (or frill), which encircles the pupil; this normally has a serrated appearance (Figure 2.4).

2.3 Anterior Iris Surface

Thin, radial, collagenous columns or trabeculae are evident in lightly pigmented irises. Thicker, radially oriented, branching trabeculae encircle depressions or openings in the surface called crypts. Crypts are located on both sides of the collarette (Fuchs' crypts) and near the root (peripheral crypts). They allow the aqueous quick exit and entrance into spaces in the iris stroma as the volume of the iris changes with iris dilation and contraction.

Circular contraction folds, evident on the anterior surface of the ciliary zone, result from tissue moving toward the iris root during pupillary dilation. Figure 2.5 shows the topography of the anterior and posterior iris surfaces. [21]

2.4 Posterior Iris Surface

The posterior surface of the iris is fairly smooth, but when viewed with magnification, small circular furrows are evident near the pupil. Radial contraction furrows (of Schwalbe) are located in the pupillary zone, and the deeper structural furrows (of Schwalbe) run throughout the ciliary zone and continue into the ciliary body as the valleys between the ciliary processes. Also found on the posterior surface are circular contraction folds similar to those seen on the anterior surface.[21]

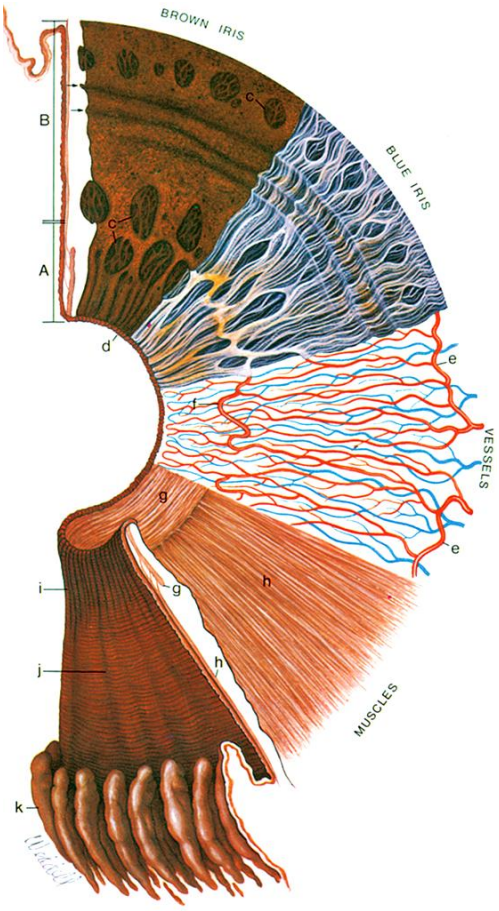

Figure 2.5: Surfaces and layers of the iris. Beginning at the upper left and proceeding clockwise, the iris cross-section shows the papillary (A) and ciliary portions (B), and the surface view shows a brown iris with its dense, matted anterior border layer. Circular contraction furrows are shown (arrows) in the ciliary portion of the iris. Fuchs' crypts (c) are seen at either side of the collarette in the pupillary and ciliary portion and peripherally near the iris root. The pigment ruff is seen at the pupillary edge (d). The blue iris surface shows a less dense anterior border layer and more prominent trabeculae. The iris vessels are shown beginning at the major arterial circle in the ciliary body (e). Radial branches of the arteries and veins extend toward the pupillary region. The arteries form the incomplete minor arterial circle (f), from which branches extend toward the pupil, forming capillary arcades. The sector below it demonstrates the circular arrangement of the sphincter muscle (g) and the radial processes of the dilator muscle (h). The posterior surface of the iris shows the radial contraction furrows (i) and the structural folds of Schwalbe (j). Circular contraction folds also are present in the ciliary portion. The pars plicata of the ciliary body is at (k). [21]

2.5 Iris Color

Iris color depends on the arrangement and density of connective tissue components in the anterior border layer and stroma, melanocyte density, and pigment density within the melanocyte. An iris appears blue for the same reason that the sky is blue; the wavelength seen results from light scatter caused by the arrangement and density of the connective tissue components. Other colors are caused by the amount of light absorption, which depends on the pigment density within the melanocytes. If the iris is heavily pigmented, the anterior surface appears brown and smooth, even velvety, whereas in a lighter iris, the collagen trabeculae are evident and the color ranges from greys to blues to greens depending on the density of pigment and collagen.

A freckle or a nevus is an area of hyperpigmentation, an accumulation of melanocytes, and frequently is seen in the anterior border layer. In all colored irises, the two epithelial layers are heavily pigmented. Only in the albino iris do the epithelial layers lack pigment.

2.6 Typical Stages of Iris Recognition

Figure 2.6 illustrates the typical stages of iris recognition systems. In spite of the specificities of the different proposals, they share the given structure. The initial stage deals with iris segmentation. This process consists in localizing the iris inner (pupillary) and outer (scleric) borders, assuming either circular or elliptical shapes for both of the borders.

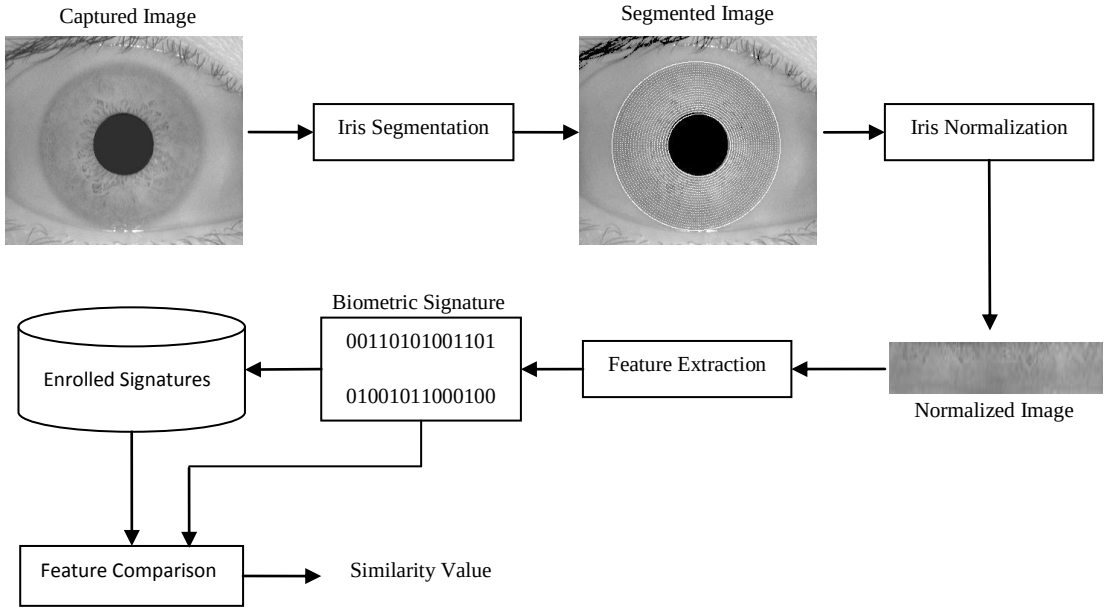

Figure 2.6: Typical stages of the iris recognition.

In order to compensate the variations in the pupil size and in the image capturing distances, it is common to translate the segmented iris region into a fixed length and dimensionless polar coordinate system. This stage is usually accomplished through the method proposed by Daugman [22].

Regarding feature extraction, iris recognition approaches can be divided into three major categories: phase-based methods (e.g., [22]), zero-crossing methods (e.g., [23]) and texture analysis based methods (e.g., [24]).

Finally, the comparison between iris signatures is made, producing a numeric dissimilarity value. If this value is higher than a threshold, the system outputs a non-match, meaning that each signature belongs to different irises. Otherwise, the system outputs a match, meaning that both signatures were extracted from the same iris.

Having overview the main stages of iris recognition and mentioned some of the most relevant approaches, in the next sub-sections, we describe some usual approaches to perform each of the above identified stages.

2.6.1 Iris Segmentation

In 1993, J. Daugman [22] presented one of the most relevant methods, constituting the basis of the majority of the functioning systems. Regarding the segmentation stage, this author introduced an integrodifferential operator to find both the iris inner and outer borders. This operator remains actual and was proposed in 2004 with minor differences by Nishino and Nayar [25].

Similarly, Camus andWildes [26] and Martin-Roche et al. [27] proposed integrodifferential operators that search the N3 space, with the objective of maximizing the equations that identify the iris borders.

Wildes [24] proposed iris segmentation through a gradient based binary edge-map construction followed by circular Hough transform. This is the most common method, that has been proposed with minor variants by Cui et al. [28], Huang et al.[29], Kong and Zhang[30], Ma et al.[31], [32] and [33].

Liam et al. [34] proposed one interesting method essentially due to its simplicity. This method is based in thresholds and in the maximization of a simple function, in order to obtain two ring parameters that correspond to iris inner and outer borders.

Du et al. [35] proposed the iris detection method based on the prior pupil segmentation. The image is further transformed into polar coordinates and the iris outer border is detected as the largest horizontal edge resultant from Sobel filtering. However, this approach may fail in case of non-concentric iris and pupil, as well as for very dark iris textures.

Morphologic operators were applied by Mira and Mayer [36] to obtain iris borders. They detected the pupillary and scleric borders by applying thresholding, image opening and closing.

Based on the assumption that the pixels' intensity of the captured image can be well represented by a mixture of three Gaussian distributions, Kim et al. [37] proposed the use of Expectation Maximization [38] algorithm to estimate the respective distribution parameters. They expected that 'Dark', 'Intermediate' and 'Bright' distributions contain the pixels corresponding to the pupil, iris and reflections areas.

2.6.2 Iris Normalization

2.6.2.1 Daugman Rubber Sheet

Due to the varying size of the pupil and of the distance and angle of the image capturing framework, the size of the captured irises can have high variations, increasing the complexity of the recognition task. Robust representations for pattern recognition must be invariant to

changes in the size, position, and orientation of the patterns. In the iris recognition compass, this requires a representation of the iris data invariant to the dimension of the captured image. This is influenced by the distance between the eye and the capturing device, by the camera optical magnification factor and by the iris orientation, caused by torsional eye rotation and camera angles. As described in [20], the invariance to all of these factors can be achieved through the translation of the captured data into a double dimensionless polar coordinate system. As Figure 2.7 illustrates, this translation process is based both in polar (θ) and radial (r) variables.

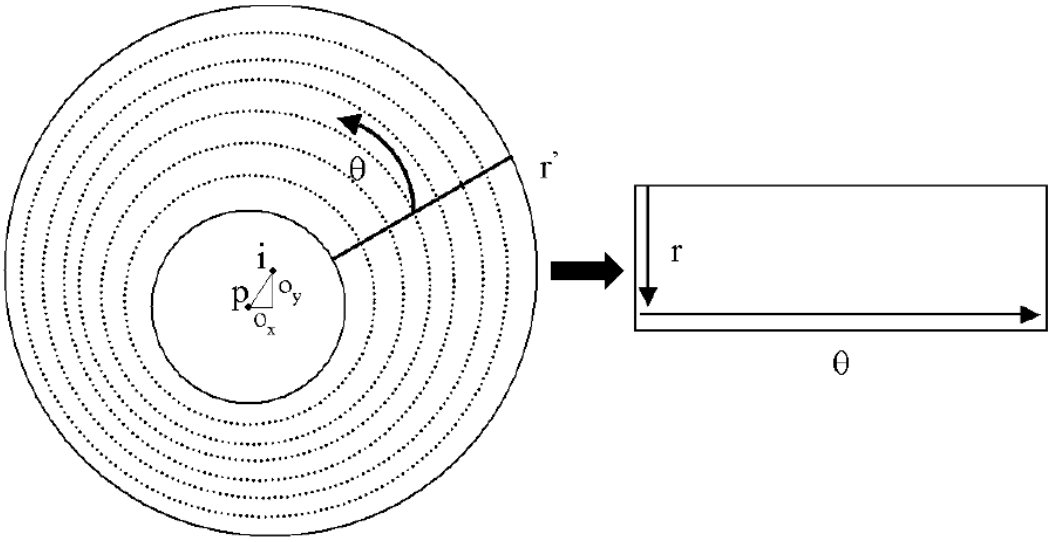

Figure 2.7: Normalization of the iris image through the Daugman rubber sheet.

The rubber sheet model assigns to each point on the iris, regardless of its size and pupillary dilation, a pair of real coordinates (r, θ), where r is on the unit interval $[0, 1]$ and (θ) is an angle in $[0, 2\pi]$. The remapping of the iris image $I(x, y)$ from raw Cartesian coordinates (x, y) to the dimensionless non concentric polar coordinate system (r, θ) can be represented as:

$$I\big(x(r,\theta), y(r,\theta)\big) \rightarrow I(r,\theta) \qquad (2.1)$$

where $x(r, \theta)$ and $y(r, \theta)$, are defined as linear combinations of both the set of papillary boundary points $\big(x_p(\theta), y_p(\theta)\big)$ and the set of limbus boundary points along the outer perimeter of the iris $\big(x_s(\theta), y_s(\theta)\big)$ bordering the sclera, which are detected in the iris segmentation stage, as:

$$\begin{cases} x(r,\theta) = (1-r) * x_p(\theta) + r * x_s(\theta) \\ y(r,\theta) = (1-r) * y_p(\theta) + r * y_s(\theta) \end{cases} \qquad (2.2)$$

2.6.2.2 Image Registration

The Wildes et al. system employs an image registration technique, which geometrically warps a newly acquired image, $I_a(x, y)$ into alignment with a selected database image

$I_d(x, y)$[4]. When choosing a mapping function $\big(u(x, y), v(x, y)\big)$ to transform the original coordinates, the image intensity values of the new image are made to be close to those of corresponding points in the reference image. The mapping function must be chosen so as to minimise

$$\int_x \int_y \big(I_d(x, y) - I_a(x - u, y - v)\big)^2 \, dx \, dy \tag{2.3}$$

While being constrained to capture a similarity transformation of image coordinates (x, y) to (x', y'), that is

$$\begin{pmatrix} x' \\ y' \end{pmatrix} = \begin{pmatrix} x \\ y \end{pmatrix} - sR(\phi) \begin{pmatrix} x \\ y \end{pmatrix} \tag{2.4}$$

With s a scaling factor and $R(\phi)$ a matrix representing rotation by ϕ. In implementation, given a pair of iris images I_a and I_d, the warping parameters s and ϕ are recovered via an iterative minimisation procedure [24].

2.6.2.3 Virtual Circles

In the Boles [23] system, iris images are first scaled to have constant diameter so that when comparing two images, one is considered as the reference image. This works differently to the other techniques, since normalisation is not performed until attempting to match two iris regions, rather than performing normalisation and saving the result for later comparisons. Once the two irises have the same dimensions, features are extracted from the iris region by storing the intensity values along virtual concentric circles, with origin at the centre of the pupil. A normalisation resolution is selected, so that the number of data points extracted from each iris is the same. This is essentially the same as Daugman's rubber sheet model, however scaling is at match time, and is relative to the comparing iris region, rather than scaling to some constant dimensions. Also, it is not mentioned by Boles, how rotational invariance is obtained.

2.6.3 Feature Extraction

As stated above, from the viewpoint of feature extraction, recognition approaches can be divided into three major categories: phase-based methods (e.g., Daugman [22]), zero-crossing methods (e.g., Boles and Boashash [23] and Roche et al. [27]) and texture analysis based methods (e.g., Wildes [24], Kim et al. [37] and Ma et al. [31]).

Daugman [22] uses multiscale quadrature wavelets to extract texture phase information and obtain an iris signature with 2048 binary components. Once again, this proposal acted as basis for others with minor differences, as Ma et al. [39].

To characterize the iris texture, Boles and Boashash [23] computed the zero-crossing representation of a 1D wavelet at different resolutions of concentric circles. Wildes [24] proposed the characterization of the iris texture through a Laplacian pyramid with 4 different levels (scales).

One of the most common approaches consist in the dyadic wavelet decomposition either using Haar, Mallat or other mother wavelets. This can be found in several proposals, among which are Ali and Hassanien [40], Ma et al. [41] and Lim et al. [42].

Other creative approaches can be found in Huang et al. [43], that used the values resultant of the independent coefficient analysis to characterize the iris texture. Muron et al. [44] proposed the codification of the whole information through the power of the Fourrier spectrum.

Du et al. [35] proposed feature extraction through the computation of invariant local texture patterns. Nam et al. [45] proposed the study of the directional properties of the image in order to create a binary signature, through the analysis of the image's second derivatives.

2.6.4 Feature Comparison

Although the method chosen to compare between iris signature is highly conditioned by the feature extraction strategy, the feature comparison is generally performed through the use of distance metrics: Hamming (e.g., Daugman [22], Tisse et al. [46]), Euclidean (e.g., Huang et al. [47]), Weighted Euclidean (e.g. Ma et al. [31]) or methods based on signal correlation (Wildes [24]).

More specific proposals were given by Lim et al. [42], through the utilization of a competitive learning neural network to achieve classification and by Ma et al. [41], through a modified nearest neighbour to compare the acquired and the enrolled samples and assign the proper entity.

2.7 Some Relevant Iris Recognition Methods

In the following sub-sections we describe with detail some of the most relevant iris recognition methods. Apart from the Daugman's method that acts as the basis and main comparison term for other proposals we describe the methods proposed by Wildes [24] and Tan et al. [48]. The choice of these methods was motivated by the analysis of the iris recognition literature and by the description of the algorithms with commercial applications [49].

2.7.1 Daugman's Method

As described in [22], the Daugman's recognition method is composed by the following stages:

2.7.1.1 Iris Segmentation.

The author describes an integrodifferential operator that searches for the maximal difference between the average intensity of circumferences with consecutive radius values.

2.7.1.2 Normalization.

After the segmentation of both iris borders, to compensate the variations in the size of the pupil, we translated the images to dimensionless polar coordinate system through a process known as the Daugman Rubber Sheet [22].

2.7.1.3 Feature Extraction.

The iris data encoding was accomplished through the use of two dimensional Gabor filters. These spatial filters have the form:

$$G(x,y) = e^{-\pi[(x-x_0)^2/\alpha^2+(y-y_0)^2\beta^2]} \cdot e^{-2\pi i[u_0(x-x_0)+v_0(y-y_0)]} \quad (2.5)$$

Where (x_0, y_0) defines the position in the image, (α, β) s the filter width and length and (u_0, v_0) specify the modulation, with spatial frequency $w_0 = \sqrt{u_0^2 + v_0^2}$ and direction $\theta_0 = \tan^{-1}(u_0/v_0)$.

The real parts of the 2-D Gabor filters are truncated to be zero volume and achieve illumination invariance. For each resulting bit the sign of the real and imaginary parts from quadrature image projections is analyzed and, through quantization, assigned binary values: 1 and 0 respectively for positive and negative projection values.

2.7.1.4 Feature Comparison.

The feature extraction binarization process allows the utilization of the Hamming distance as the similarity measure for two iris signatures. Given two binary sets with N bits: $A = \{a_1, \ldots, a_N\}$ and $B = \{b_1, \ldots, b_N\}$, the Hamming distance is:

$$HD(A,B) = \frac{1}{N} * \sum_{i=1}^{N} a_i \otimes b_i \quad (2.6)$$

being $a \otimes b$ the logical XOR operation. Thus, for two completely equal and different signatures, the value of the Hamming distance will be respectively 0 and 1.

2.7.2 Wildes Method

In [24], Wildes describes a machine vision system for noninvasive biometric assessment. It is divided into three parts: image acquisition, image segmentation and image matching.

2.7.2.1 Image Acquisition.

Due to its relatively small dimensions, the author considered the image acquisition as one of the major challenges for automated iris recognition. First, it is stressed the importance of acquiring iris images with sufficient resolution and sharpness to support recognition. Second, the requirement of good contrast in the iris pattern, without resorting to a level of illumination that annoys the subject. The captured images must be centred and the artifact (e.g. specular reflections and optical aberrations) should be eliminated as much as possible. Based in these

concerns, the author describes an optical framework for the iris capturing from a distance of 20 cm. using a 80 mm. lens.

2.7.2.2 Iris Localization.

Image acquisition will capture the iris as part of a larger image that also contains data corresponding to the region surrounding the eye. Therefore, it is important to localize that portion of the acquired image that corresponds to the iris. The author performs its contour fitting in two steps. First, the image intensity information is converted into a binary edge-map. Second, the edge points vote to instantiate particular contour parameter values. The edge-map is recovered through a gradient-based edge detection, that consists of thresholding the magnitude of the image intensity gradient convolved with a two-dimensional Gaussian Kernel G defined by:

$$G(x,y) = \frac{1}{2\pi\sigma^2} e^{-\frac{(x-x_0)^2+(y-y_0)^2}{2\sigma^2}} \tag{2.7}$$

where (x_0, y_0) is the centre of the kernel and σ its standard deviation. In order to incorporate directional tuning, the image intensity derivatives are weighted to favour certain ranges of orientation prior to taking the magnitude. Figure 2.8 illustrates edgemaps with (Figure 2.8a) and without (Figure 2.8b) orientation favors.

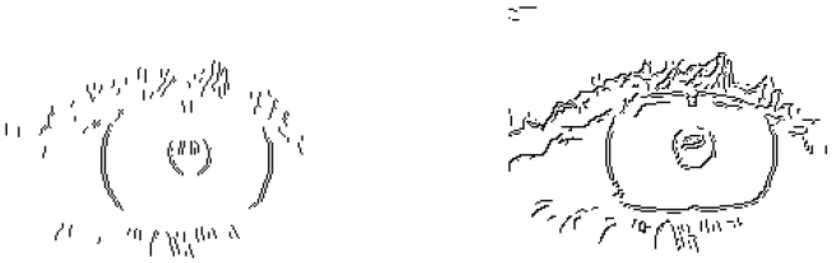

(a)Edge-map with vertical orientation favor (b) Edge-map without orientation favors.

Figure 2.8: Morphology of the human eye.

Regarding the detection of the limbic boundary, the derivatives are weighted to be selective for vertical edges, as the probability for the detection of edges correspondent to eyelids is minor. The voting procedure is realized via the circular Hough transform, defined as:

$$H(x_c, y_c, r) = \sum_{j=1}^{n} h(x_j, y_j, x_c, y_c, r) \tag{2.8}$$

where

$$h(x_j, y_j, x_c, y_c, r) = \begin{cases} 1 \ \ if \ g(x_j, y_j, x_c, y_c, r) = 0 \\ 0 \ otherwise \end{cases} \tag{2.9}$$

and

$$g(x_j, y_j, x_c, y_c, r) = (x_j - x_c)^2 + (y_j - y_c)^2 - r^2 \quad (2.10)$$

The triple parameter that maximizes H is a reasonably choice to represent the contours of interest, the iris inner and outer borders. Regarding the upper and lower eyelids, they are fitted in a similar fashion using parameterized parabolic arcs in place of the circle parametrization $g(x_j, y_j, x_c, y_c, r)$.

2.7.2.3 Pattern Matching.

After the identification of the region correspondent to the iris, the final task is to decide if the captured pattern matches a previously enrolled. The author decomposes this task in four parts: alignment, representation, comparison and decision.

- **Alignment.** The author uses an image registration technique to compensate scaling and rotation. It geometrically warps a newly acquired image, $I_a(x, y)$ into alignment with a selected database image $I_d(x, y)$. When choosing a mapping function $(u(x, y), v(x, y))$ to transform the original coordinates, the image intensity values of the new image are made to be close to those of corresponding points in the reference image. The mapping function must be chosen so as to minimise
  - $\int_x \int_y (I_d(x, y) - I_a(x - u, y - v))^2 \, dx \, dy \quad (2.11)$

  While being constrained to capture a similarity transformation of image coordinates (x, y) to (x', y'), that is
  - $\begin{pmatrix} x' \\ y' \end{pmatrix} = \begin{pmatrix} x \\ y \end{pmatrix} - sR(\phi) \begin{pmatrix} x \\ y \end{pmatrix} \quad (2.12)$

  With s a scaling factor and $R(\phi)$ a matrix representing rotation by ϕ. In implementation, given a pair of iris images I_a and I_d, the warping parameters s and ϕ are recovered via an iterative minimisation procedure.

- **Representation.** An isotropic band-pass decomposition is proposed, derived from application of Laplacian of Gaussian filters to the image data. These filters can be defined as:

$$-\frac{1}{\pi\sigma^4}\left(1 - \frac{\rho^2}{2\sigma^2}\right) e^{-\frac{\rho^2}{2\sigma^2}} \quad (2.13)$$

  where σ is the standard deviation of the Gaussian and ρ is the radial distance of the point to the filter center. This procedure can be implemented through a Laplacian pyramid. Given an image I, it is iteratively convolved with a low pass filter and down sampled by a factor of two in each dimension. This multi scale representation of the image is used as the biometric iris signature. Oppositely to the Daugman's system, this representation is

derived directly from the filtered image for size on the order of the dimension of the captured iris image.

- **Comparison.** In this stage a procedure based on the normalized correlation between both iris signatures is used. Let A_1 and A_2be two arrays of size $n \times m$. Also, let μ_1 and μ_2 be respectively the mean of A_1 and A_2 and σ_1 and σ_2 be the standard deviation of A_1 and A_2. The normalized correlation can be defined as:

$$\frac{1}{nm\sigma_1\sigma_2}\sum_{i=1}^{n}\sum_{j=1} n(A_1(i,j)-\mu_1)(A_2(i,j)-\mu_2) \tag{2.14}$$

  The author applies the correlations over small 8×8 blocks in each of the four spatial frequency bands resultant from the Laplacian pyramid representation. Further, these values are combined into a single value via the median statistic, yielding four goodness-of-match values.

- **Decision.** This stage combines the previously obtained four values into a single accept/reject judgement, through the Fisher linear discriminant. Let n be the number of samples q_i (four comparisons between multi scale measurements), n_A of which are authentics and n_I from impostors. Fisher's linear discriminant defines a weight vector w such that the ratio of intra- and inter-class variance is maximized for the transformed samples $w^T q$. Let μ_A and μ_I be the $d-$dimensional mean values respectively for $q \in A$ and $q \in I$. A measure of variance within a class C can be given by a scatter matrix with form:

$$S_C = \sum_{q \in C}(q-\mu C)(q-\mu C)^T \tag{2.15}$$

  In this case, the total within class scatter is given by $S_{intra} = S_A + S_I$. A corresponding measure of the variance between classes can be defined in terms of the scatter matrix $S_{inter} = (\mu_A - \mu_I)(\mu_A - \mu_I)^T$. Thus, the following expression describes the ratio of intra- and inter-class variance of the transformed samples wq:

$$\frac{w^T S_{inter} w}{w^T S_{intra} w} \tag{2.16}$$

  Finally, the w that maximizes this ratio is given by:

$$w = S_{intra}^{-1}(\mu_A - \mu_I) \tag{2.17}$$

  In order to apply this discriminant to the classification task a separation point must be defined. Values above this point will be taken as derived from class A and values below this point will be taken as derived from class I. The author takes the separation point as the midpoint between the transformed means of the samples from A and I, which can be proven to be optimal if the probabilities of the measurements given either class have normal distributions and equal variance.

2.7.3 Ma et al. Method

Ma et al. [48] described an iris recognition algorithm based in the characterization of key local variations. It is composed of five main stages:

2.7.3.1 Iris Localization.

The authors approximate both the pupillary and scleric borders as circles. The procedure starts by roughly iris region finding followed by the exact computation of the parameters correspondent to both iris borders, according to a procedure similar to that of Wildes' [24] proposal.

2.7.3.2 Iris Normalization.

In order to compensate the variations in pupil size and in image capturing distance, authors apply the normalization process to the segmented iris image described by Daugman [22].

2.7.3.3 Image Enhancement.

Since there is a non-uniform brightness and low contrast of the normalized iris images, the authors perform image enhancement based in the subtraction of the estimated background illumination of small blocks (32×32) of the image. Such processing compensates for the non-uniform illumination.

2.7.3.4 Feature Extraction.

Considering the characteristics of the iris as a sort of transient signals, authors construct a set of 1-D intensity signals, according to the following equation:

$$S_i = \frac{1}{M}\sum_{j=1}^{M} I_{(i-1)*M+j}, i = 1, \dots, N \tag{2.18}$$

where I is the normalized image of $K \times L$ and I_x denotes the x^{th} row of the image. M is the total number of rows used to form S_i and N is the total number of 1-D signals. Each signal is a combination of M successive horizontal scan lines of the image, reflecting its local variations along the horizontal direction. Further, authors used the dyadic wavelet decomposition and the Mallat as mother-wavelet. Analyzing the local minimums and maximums of the resultant signal at the analyzed scales, the authors observed that each pair of local extremum points corresponds to faint characteristics variations in the original iris image. For each signal S_i, the position of those points at two scales are concatenated to form the corresponding features:

$$f_i = \{d_1, \dots, d_m, d_{m+1}, \dots, d_{m+n}, p_1, p_2\} \tag{2.19}$$

where m and n are respectively the number of components from both scales and d_i denote the position of the local variations in the 1-D signal. p_i represents the type of the first

extremum point at each scale. Further, the features correspondent to different scales (intensity signals) are concatenated in the feature vector f:

$$f = \{f_1, f_2, \ldots, f_N\}$$

where N is the total number of 1-D intensity signals.

2.7.3.5 Matching.

This stage is accomplished through a two-step approach:

- The original feature vector is expanded into binary form. At each position, the components p_i are set to 1 or -1 according to the type of extremum point. Authors set the maximums to 1 in the binary sequence and the minimums to -1, building a binary feature vector given by:

  $$Ef = \{Ef_1, Ef_2, \ldots, Ef_N\}$$

  where Ef_i denotes the binary expansion of feature component f_i.

- The similarity between two binary sequences is computed through the XOR function, given by:

  $$D = \frac{1}{N}\sum_{i=1}^{N}\frac{1}{2L}\sum j = 1^2\left(EF^1_{(i,j)} \otimes EF^2_{(i,j)}\right) \quad (2.20)$$

  where Ef^1 and Ef^2 denote two different binary feature vectors, $\otimes$ is the "XOR" operator, L is the length of the binary sequence and N is the total number of 1-D intensity signals.

2.8 Iris Image Database

The biometrics research and development demands the analysis of human data. Obviously, it is unrealistic to perform the test of algorithms in data captured on-the-fly, due to the enormous uneasiness that this would imply. Moreover, the fair comparison between recognition methods demands similar input data to valorize and contextualize their results. Therefore, when it comes to the test of recognition methods, standard biometric databases assume high relevance and become indispensable to the development process.

Iris recognition has been an active research topic of the Institute of Automation from the Chinese Academy of Sciences. Having concluded about a lack of iris data for algorithm testing, they developed the CASIA image database. Apart from being the oldest, this database is clearly the most known and widely used by the majority of the researchers.

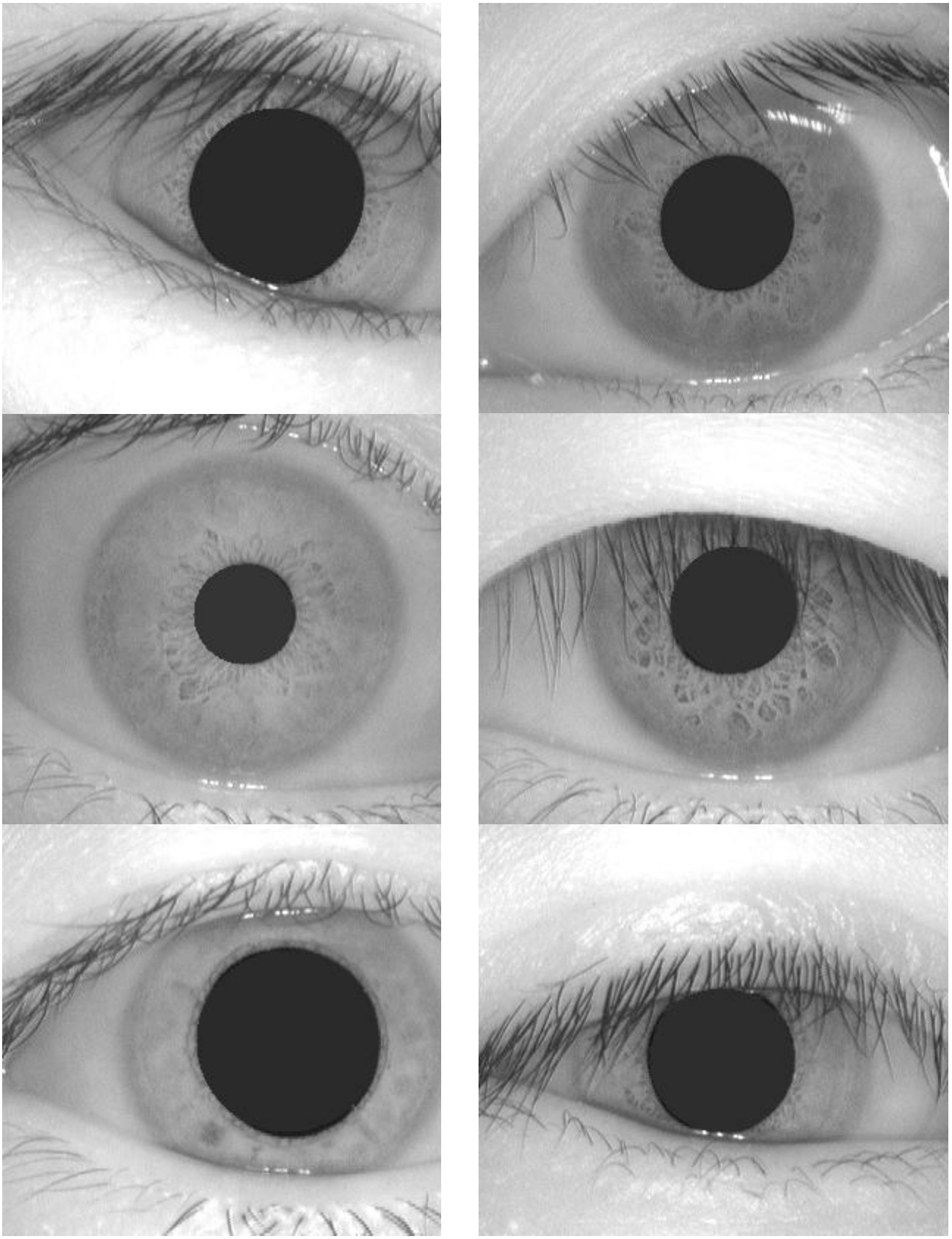

Figure 2.9: Examples of iris images from the CASIA database.

CASIA iris image database (version 1.0) includes 756 iris images from 108 eyes, hence 108 classes. For each eye, 7 images are captured in two sessions, where three samples are collected in the first and four in the second session. Similarly to the above described database, its images were captured within an highly constrained capturing environment, which conditioned the characteristics of the resultant images. They present very close and homogeneous characteristics and their noise factors are exclusively related with iris obstructions by eyelids and eyelashes. Moreover, the post process of the images filled the pupil regions with black pixels, which some authors used to facilitate the segmentation task. From our viewpoint, this significantly decreased the utility of the database in the evaluation of robust iris recognition methods.

Chapter 3: Segmentation and Normalization

Image segmentation can be defined as the partitioning of an image into several components. It is an important stage of any automated image processing system, essentially because it is the basis for any further operations, such as description or recognition. In the pattern recognition domain, segmentation is the assignment of each pixel to an image region, which can be regarded as a typical classification problem.

3.1 Iris Segmentation

The first stage of iris recognition is to isolate the actual iris region in a digital eye image. The iris region, can be approximated by two circles, one for the iris/sclera boundary and another, interior to the first, for the iris/pupil boundary. The eyelids and eyelashes normally occlude the upper and lower parts of the iris region. Also, specular reflections can occur within the iris region corrupting the iris pattern. A technique is required to isolate and exclude these artefacts as well as locating the circular iris region.

The success of segmentation depends on the imaging quality of eye images. Images in the CASIA iris database do not contain specular reflections due to the use of near infra-red light for illumination. The segmentation stage is critical to the success of an iris recognition system, since data that is falsely represented as iris pattern data will corrupt the biometric templates generated, resulting in poor recognition rates.

Well-known methods such as the Integrodifferential, Hough transform and active contour models have been successful techniques in detecting the boundaries. In the following section, these methods are described with their Implementation in MATLAB®.

3.2 Daugman's Method

This is by far the most cited method [22] in the iris recognition literature. It is licensed to Iridian Technologies who turned it into the basis of 99.5% of the commercial iris recognition systems. It was proposed in 1993 and was the first method effectively implemented in a working biometric system. The author assumes both pupil and iris with circular form and applies the following integrodifferential operator:

$$\max_{r,x_0,y_0} \left| G_\sigma(r) * \frac{\delta}{\delta r} \oint_{r,x_0,y_0} \frac{I(x,y)}{2\pi r} ds \right| \tag{3.1}$$

This operator searches over the image domain $(x, y)$for the maximum in the blurred (by a Gaussian Kernel $G_\sigma(r)$ partial derivative with respect to increasing radius r, of the normalized contour integral of $I(x, y)$ along a circular arc ds of radius r and center coordinates (x_0, y_0). In other words, this method searches in the $\mathbb{N}^3$ space for the circumference center and radius with highest derivative values comparing to circumferences of neighbour radius. As showed in section, this process proved to be very effective on images with enough separability between iris, pupil and sclera intensity values. However, we

observed that it frequently fails when the images do not have sufficient intensity separability, specially between the iris and the sclera regions.

At first the blurring factor σ is set for a coarse scale of analysis so that only the very pronounced circular transition from iris to (white) sclera is detected. Then after this strong circular boundary is more precisely estimated, a second search begins within the confined central interior of the located iris for the fainter pupillary boundary, using a finer convolution scale σ and a smaller search range defining the paths (x_0, y_0, r)contour integration. In the initial search for the outer bounds of the iris, the angular arc of contour integration ds is restricted in range to two opposing 90^0cones centered on the horizontal meridian, since eyelids generally obscure the upper and lower limbus of the iris. Then in the subsequent interior search for the pupillary boundary, the arc of contour integration ds in operator (3.1) is restricted to the upper 270^0 in order to avoid the corneal specular reflection that is usually superimposed in the lower 90^0 cone of the iris from the illuminator located below the video camera. Taking the absolute value in (3.1) is not required when the operator is used first to locate the outer boundary of the iris, since the sclera is always lighter than the iris and so the smoothed partial derivative with increasing radius near the limbus is always positive. However, the pupil is not always darker than the iris, as in persons with normal early cataract or significant back-scattered light from the lens and vitreous humor; applying the absolute value in (3.1) makes the operator a good circular edge-finder regardless of such polarity-reversing conditions. With σ automatically tailored to the stage of search for both the pupil and limbus, and by making it correspondingly finer in successive iterations, the operator defined in (3.1) has proven to be virtually infallible in locating the visible inner and outer annular boundaries of irises.

For rapid discrete implementation of the integrodifferential operator in (3.1), it is more efficient to interchange the order of convolution and differentiation and to concatenate them, before computing the discrete convolution of the resulting operator with the discrete series of undersampled sums of pixels along circular contours of increasing radius. Using the finite difference approximation to the derivative for a discrete series in n,

$$\frac{\partial G_\sigma(r)}{\partial r} \approx G_\sigma^1(n) = \frac{1}{\Delta r} G_\sigma(n\Delta r) - \frac{1}{\Delta r} G_\sigma\big((n-1)\Delta r\big) \tag{3.2}$$

where Δr is a small increment in radius, and replacing the convolution and contour integrals with sums, we can derive through these manipulations an efficient discrete operator (3) for finding the inner and outer boundaries of an iris where $\Delta\theta$ is the angular sampling interval along the circular arcs, over which the summed $I\,(x\,, y)$ pixel intensities represent the contour integrals expressed in (3.1).

$$\max_{n\Delta r, x_0, y_0} \left| \frac{1}{\Delta r} \sum_k \left\{ \Big(G_\sigma\big((n-k)\Delta r\big) - G_\sigma\big((n-k-1)\Delta r\big) \Big) \times \sum_m I[(k\Delta r \cos(m\Delta\theta) + x_0\,), (k\Delta r \sin(m\Delta\theta) + y x_0\,)] \right\} \right| \tag{3.3}$$

$$\max_{n\Delta r, x_0, y_0} \left| \sum_k \{ \left(G_\sigma\big((n-k)\Delta r\big) - G_\sigma\big((n-k-1)\Delta r\big) \right) \right.$$
$$\times \sum_m I[(k\Delta r \cos(m\Delta\theta) + x_0), (k\Delta r \sin(m\Delta\theta) + y x_0)]$$
$$\left. / \Delta r \sum_m I\big[\big((k-2)\Delta r \cos(m\Delta\theta) + x_0\big), \big((k-2)\Delta r \sin(m\Delta\theta) + y x_0\big)\big] \right\} | \quad (3.4)$$

A nonlinear enhancement of this operator makes it more robust for detecting the inner boundary of the iris. Because the circular edge that defines the pupillary boundary is often very faint, especially in dark-eyed persons, it is advantageous to divide each term in the convolution summation over k in (3.3) by a further contour integral around a smaller radius $(k-2)\Delta r$. This divisor becomes very small and stable as the parameters $(n\Delta r, x_0, y_0)$ of contour integration become wellmatched to the true location and size of the pupil, and this helps the resulting sum of ratio terms (3.4) to achieve a distinctive maximum that reliably locates the pupillary boundary. In essence, dividing by the second contour integral exploits the fact that the interior of the pupil is generally both homogeneous and dark. This creates a suddenly very small divisor when the parameters $(n\Delta r, x_0, y_0)$ are optimal for the true pupil, thus producing a sharp maximum in the overall search operator (3.4).

Using multigrid search with gradient ascent over the image domain (x, y) for the center coordinates and initial radius of each series of contour integrals, and decimating both the incremental radius interval Δr and the angular sampling interval $\Delta\theta$ in successively finer scales of search spanning four octaves, these iris locating operations become very efficient without loss of reliability.

3.3 Hough Transform

Hough transform is a standard image analysis tool for finding curves that can be defined in a parametrical form such as lines, polynomials and circles. The recognition of a global pattern is achieved using the local patterns. For instance, recognition of a circle can be achieved by considering the strong edges in an image as the local patterns and searching for the maximum value of a circular Hough transform.

Wildes et al. [24], Kong and Zhang [30], Tisse et al. [46] and Ma et al. [31] use Hough transform to localize irises. The localization method, similar to Daugman's method, is also based on the first derivative of the image. In the proposed method by Wildes, an edge map of the image is first obtained by thresholding the magnitude of the image intensity gradient:

$$|\nabla G(x, y) * I(x, y)| \quad (3.5)$$

Where $\nabla \equiv (\partial/\partial x, \partial/\partial y)$ and $G(x, y) = \frac{1}{2\pi\sigma^2} e^{-\frac{(x-x_0)^2+(y-y_0)^2}{2\sigma^2}}$. $G(x, y)$ is a Gaussian smoothing function with scaling parameter σ to select the proper scale of edge analysis.

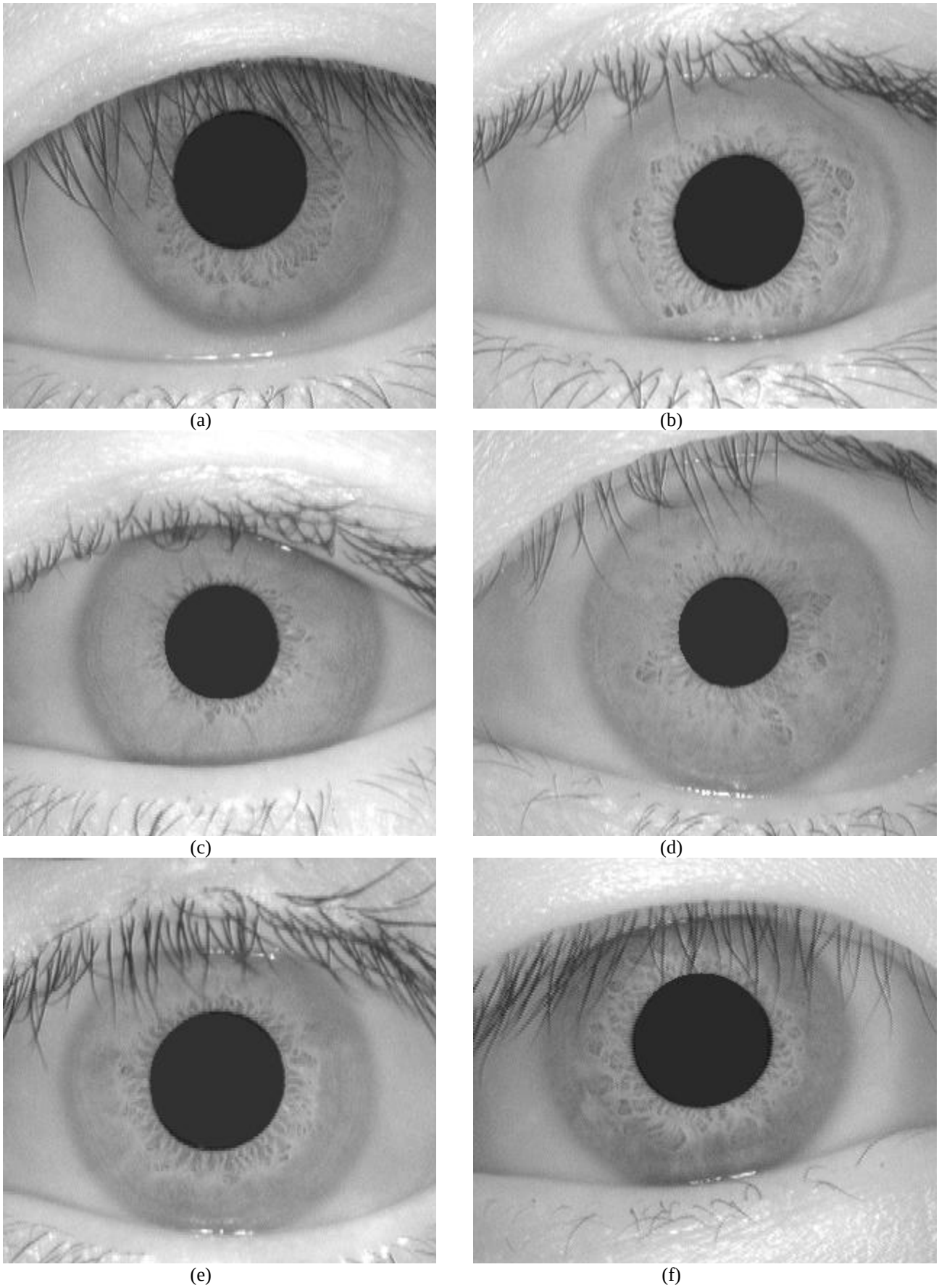

(a) (b) (c) (d) (e) (f)

Figure 3.1: Sample CASIA database Images

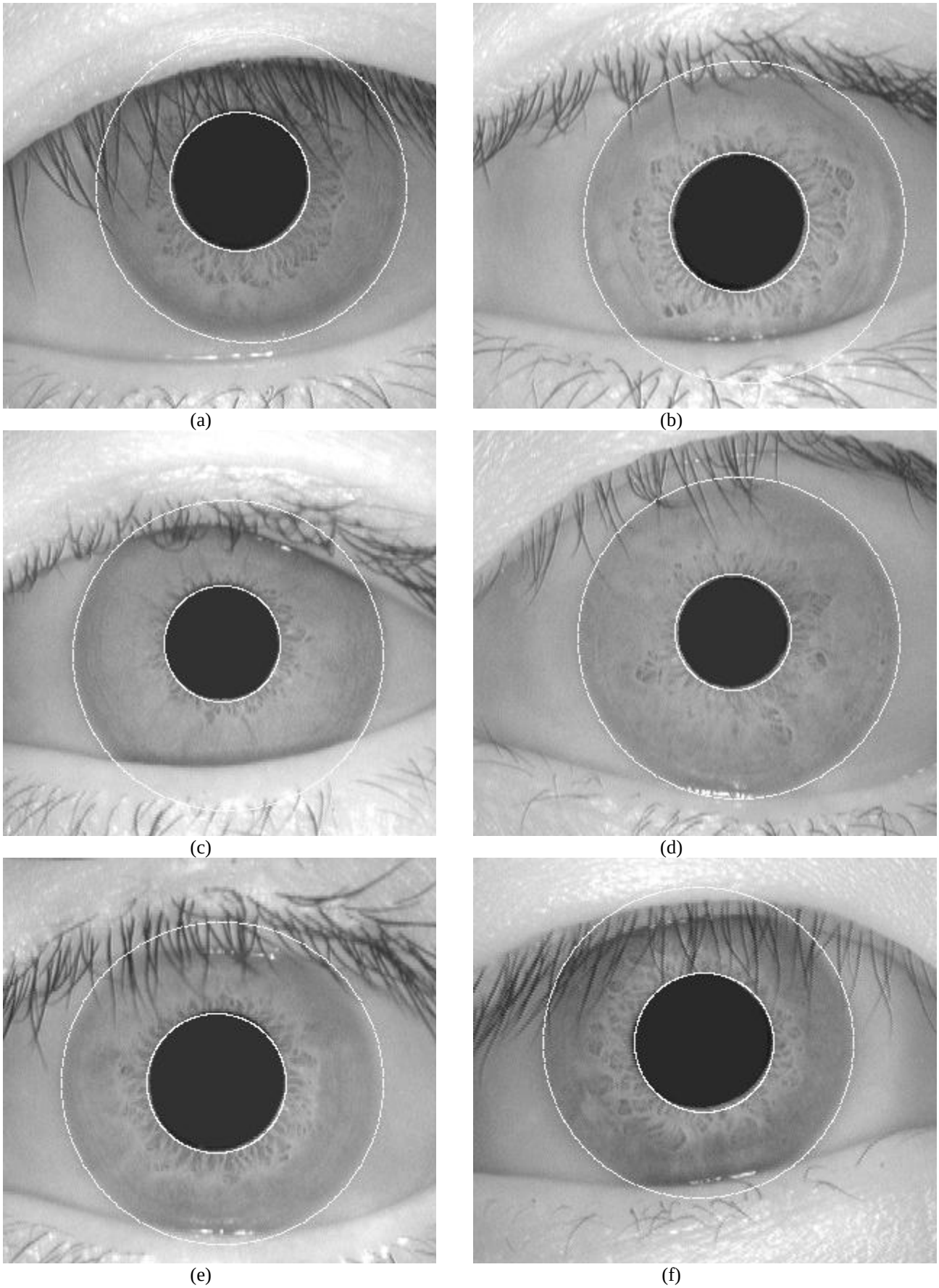

(a) (b)

(c) (d)

(e) (f)

Figure 3.2: Segmented images using Daugman's method.

The edge map is then used in a voting process to maximize the defined Hough transform for the desired contour. Considering the obtained edge points as $(x_j, y_j), j = 1,2, \dots, n$, a Hough transform can be written as:

$$H(x_c, y_c, r) = \sum_{j=1}^{n} h(x_j, y_j, x_c, y_c, r) \tag{3.6}$$

where

$$h(x_j, y_j, x_c, y_c, r) = \begin{cases} 1 \ if \ g(x_j, y_j, x_c, y_c, r) = 0 \\ 0 \ otherwise \end{cases} \tag{3.7}$$

The limbus and pupil are both modeled as circles and the parametric function g is defined as:

$$g(x_j, y_j, x_c, y_c, r) = (x_j - x_c)^2 + (y_j - y_c)^2 - r^2 \tag{3.8}$$

Assuming a circle with the center (x_c, y_c) and radius r, the edge points that are located over the circle result in a zero value of the function. The value of g is then transformed to 1 by the h function, which represents the local pattern of the contour. The local patterns are then used in a voting procedure using the Hough transform, H, in order to locate the proper pupil and limbus boundaries. In order to detect limbus, only vertical edge information is used. The upper and lower parts, which have the horizontal edge information, are usually covered by the two eyelids. The horizontal edge information is used for detecting the upper and lower eyelids, which are modeled as parabolic arcs.

We implemented this method in MATLAB® by first employing Canny edge detection to generate an edge map. Gradients were biased in the vertical direction for the outer iris/sclera boundary, as suggested by Wildes et al. [24]. Vertical and horizontal gradients were weighted equally for the inner iris/pupil boundary.

The range of radius values to search for was set manually, depending on the database used. For the CASIA database, values of the iris radius range from 90 to 150 pixels, while the pupil radius ranges from 28 to 75 pixels. In order to make the circle detection process more efficient and accurate, the Hough transform for the iris/sclera boundary was performed first, then the Hough transform for the iris/pupil boundary was performed within the iris region, instead of the whole eye region, since the pupil is always within the iris region. After this process was complete, six parameters are stored, the radius, and x and y centre coordinates for both circles.

Eyelids were isolated by first fitting a line to the upper and lower eyelid using the linear Hough transform. A second horizontal line is then drawn, which intersects with the first line at the iris edge that is closest to the pupil. This process is illustrated in Figure 3.3 and is done for both the top and bottom eyelids. The second horizontal line allows maximum isolation of eyelid regions. Canny edge detection is used to create an edge map, and only horizontal gradient information is taken. The linear Hough transform is implemented using the MATLAB® Radon transform, which is a form of the Hough transform. If the maximum

in Hough space is lower than a set threshold, then no line is fitted, since this corresponds to non-occluding eyelids. Also, the lines are restricted to lie exterior to the pupil region, and interior to the iris region. A linear Hough transform has the advantage over its parabolic version, in that there are less parameters to deduce, making the process less computationally demanding. For isolating eyelashes in the CASIA database a simple thresholding technique was used, since analysis reveals that eyelashes are quite dark when compared with the rest of the eye image.

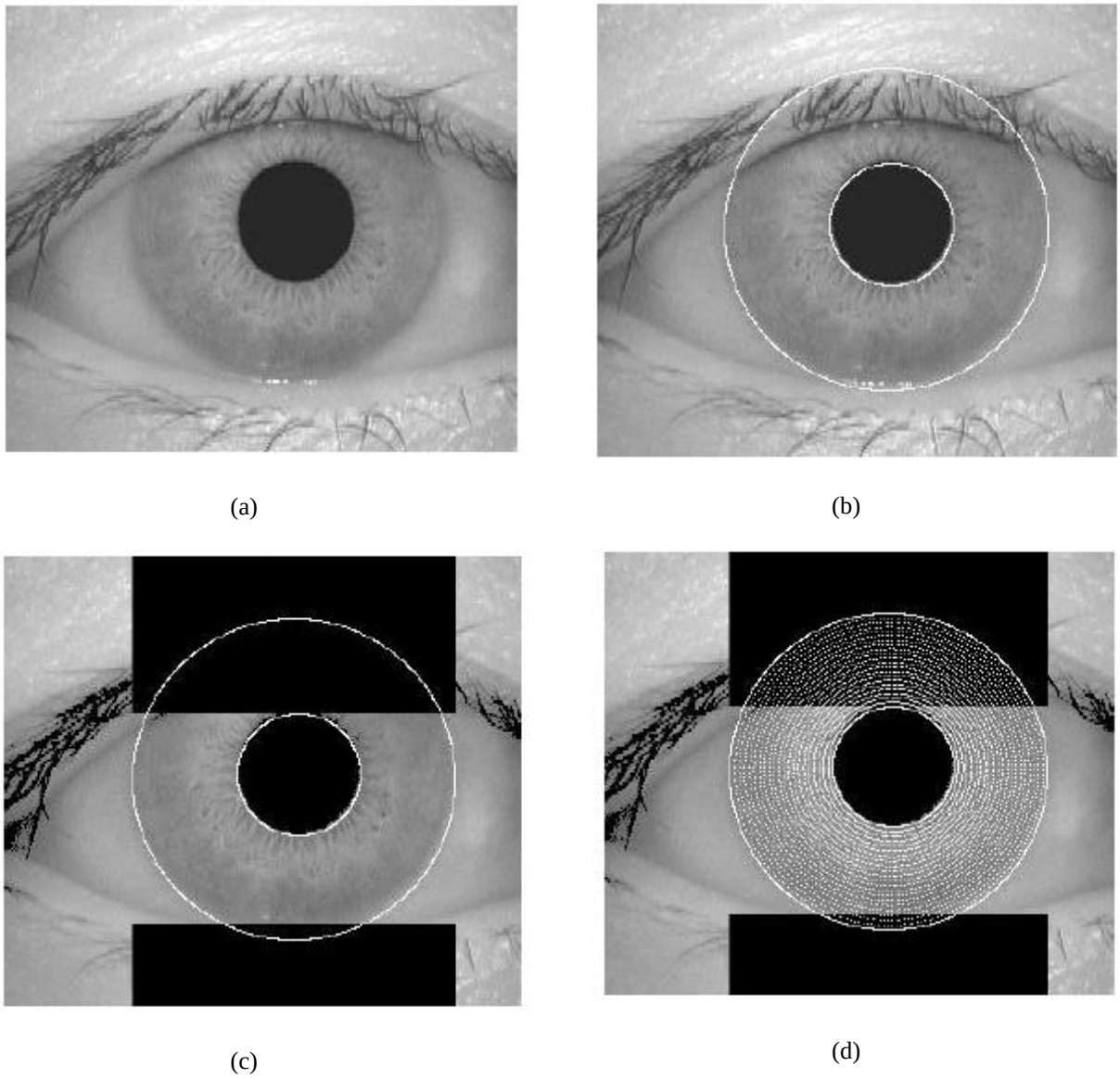

(a) (b)

(c) (d)

Figure 3.3: (a) original eye image, (b) Segmented image, (c) and (d) eyelids and eyelashes isolation.

3.4 Discrete Circular Active Contours

Ritter proposed an active contour model to localize iris in an image [50]. The model detects pupil and limbus by activating and controlling the active contour using two defined forces: internal and external forces. The internal forces are responsible to expand the contour into a

perfect polygon with a radius δ larger than the contour average radius. The internal force, $F_{int,i}$,applied to each vertex, V_i, is defined as:

$$F_{int,i} = \bar{V}_i - V_i \tag{3.9}$$

where $\bar{V}_i$ is the expected position of the vertex in the perfect polygon. The position of $\bar{V}_i$ can be obtained with respect to C_r, the average radius of the current contour, and the contour center, $C = (C_x, C_y)$. The center of a contour is defined as:

$$C = (x_C, y_C) = \frac{1}{n}\sum_{i=1}^{n} V_i \tag{3.10}$$

which is the average position of all contour vertices. The average radius of the contour is defined as:

$$C_r = \frac{1}{n}\sum_{i=1}^{n} \|V_i - C\| \tag{3.11}$$

which is the average distance of all the vertices from the defined center point. The position of the vertices of the expected perfect polygon is then obtained as:

$$\bar{V}_i = \left(C_x + (C_r + \delta)\cos(2\pi i/n\,),\, C_y + (C_r + \delta)\sin(2\pi i/n)\right) \tag{3.12}$$

where n is the total number of vertices.

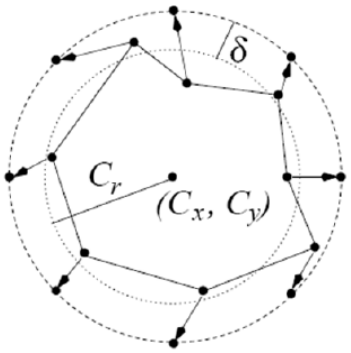

Figure 3.4: The internal forces of the Discrete Circular Active Contour

The internal forces are designed to expand the contour and keep it circular. The force model assumes that pupil and limbus are globally circular, rather than locally, to minimize the undesired deformations due to specular reflections and dark patches near the pupil boundary.

The contour detection process of the model is based on the equilibrium of the defined internal forces with the external forces. The external forces are obtained from the grey level intensity values of the image and are designed to push the vertices inward. The magnitude of the external forces is defined as:

$$\left\|F_{ext,i}\right\| = I(V_i) - I\left(V_i + \hat{F}_{ext,i}\right) \tag{3.13}$$

where $I(V_i)$ is the grey level value of the nearest neighbour to V_i. $\hat{F}_{ext,i}$ is the direction of the external force for each vertex and it is defined as a unit vector given by:

$$\hat{F}_{ext,i} = \frac{C - V_i}{\|C - V_i\|} \tag{3.14}$$

Therefore, the external force over each vertex can be written as:

$$F_{ext,i} = \left\|F_{ext,i}\right\|\hat{F}_{ext,i} \tag{3.15}$$

The movement of the contour is based on the composition of the internal and external forces over the contour vertices. Replacement of each vertex is obtained iteratively by:

$$V_i(t+1) = V_i(t) + \beta F_{int,i} + (1-\beta)F_{ext,i} \tag{3.16}$$

where β is a defined weight that controls the pace of the contour movement and sets the equilibrium condition of internal and external forces. The final equilibrium is achieved when the average radius and center of the contour becomes the same as the one in m iterations ago.

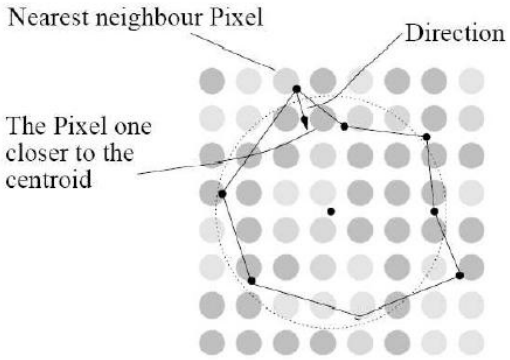

Figure 3.5: The external forces of the Discrete Circular Active Contour.

3.4.1 Level Set Evolution Without Re-Initialization.

We proposed a new segmentation method based on Chunming Li's [66] method. In recent years, a large body of work on geometric active contours, i.e., active contours implemented via level set methods, has been proposed to address a wide range of image segmentation problems in image processing and computer vision. Level set methods were first introduced by Osher and Sethian for capturing moving fronts. Active contours were introduced by Kass, Witkins, and Terzopoulos for segmenting objects in images using dynamic curves. The existing active contour models can be broadly classified as either parametric active contour models or geometric active contour models according to their representation and implementation. In particular, the parametric active contours are represented explicitly as parameterized curves in a Lagrangian framework, while the geometric active contours are represented implicitly as level sets of a two-dimensional function that evolves in an Eulerian framework.[51]

In implementing the traditional level set methods, it is numerically necessary to keep the evolving level set function close to a signed distance function. Re-initialization, a technique for periodically re-initializing the level set function to a signed distance function during the evolution, has been extensively used as a numerical remedy for maintaining stable curve evolution and ensuring usable results. However, as pointed out by Gomes and Faugeras, re-initializing the level set function is obviously a disagreement between the theory of the level set method and its implementation. Moreover, many proposed re-initialization schemes have an undesirable side effect of moving the zero level set away from its original location. It still remains a serious problem as when and how to apply the re-initialization. So far, the re-initialization procedure has often been applied in an ad-hoc manner. [51]

Chunming Li presented a new variational formulation that forces the level set function to be close to a signed distance function, and therefore completely eliminates the need of the costly re-initialization procedure. Its variational energy functional consists of an internal energy term and an external energy term, respectively. The internal energy term penalizes the deviation of the level set function from a signed distance function, whereas the external energy term drives the motion of the zero level set to the desired image features such as object boundaries. The resulting evolution of the level set function is the gradient flow that minimizes the overall energy functional. Due to the internal energy, the level set function is naturally and automatically kept as an approximate signed distance function during the evolution. Therefore, the re-initialization procedure is completely eliminated. The proposed variational level set formulation has three main advantages over the traditional level set formulations. First, a significantly larger time step can be used for numerically solving the evolution PDE, and therefore speeds up the curve evolution. Second, the level set function could be initialized as functions that are computationally more efficient to generate than the signed distance function. Third, the proposed level set evolution can be implemented using simple finite difference scheme, instead of complex upwind scheme as in traditional level set formulations. The proposed algorithm has been applied to CASIA images with promising results. In particular it appears to perform robustly in the presence of weak boundaries.

In the following sections, we give necessary background, describe Chunming Li's method and its implementation, and provide experimental results that show the overall characteristics and performance of this method.

3.4.1.1 Traditional Level Set Methods

In level set formulation of moving fronts (or active contours), the fronts, denoted by C, are represented by the zero level set $C(t) = \{(x, y)|\phi(t, x, y) = 0\}$ of a level set function $\phi(t, x, y)$. The evolution equation of the level set function ϕ can be written in the following general form:

$$\frac{\partial \phi}{\partial t} + F|\nabla \phi| = 0 \tag{3.17}$$

which is called level set equation. The function F is called the speed function. For image segmentation, the function F depends on the image data and the level set function ϕ.

In traditional level set methods, the level set function ϕ can develop shocks, very sharp and/or flat shape during the evolution, which makes further computation highly inaccurate. To avoid these problems, a common numerical scheme is to initialize the function ϕ as a signed distance function before the evolution, and then "reshape" (or "re-initialize") the function ϕ to be a signed distance function periodically during the evolution. Indeed, the re-initialization process is crucial and cannot be avoided in using traditional level set methods. [51]

3.4.1.2 Drawbacks Associated with Re-initialization

Re-initialization has been extensively used as a numerical remedy in traditional level set methods [5–7]. The standard re-initialization method is to solve the following re-initialization equation

$$\frac{\partial \phi}{\partial t} = sign(\phi_0)(1 - |\nabla \phi|) \tag{3.18}$$

where ϕ_0 is the function to be re-initialized, and $sign(\phi_0)$ is the sign function. There has been copious literature on re-initialization methods, and most of them are the variants of the above PDE-based method. Unfortunately, if ϕ_0 is not smooth or ϕ_0 is much steeper on one side of the interface than the other, the zero level set of the resulting function ϕ can be moved incorrectly from that of the original function. Moreover, when the level set function is far away from a signed distance function, these methods may not be able to re-initialize the level set function to a signed distance function. In practice, the evolving level set function can deviate greatly from its value as signed distance in a small number of iteration steps, especially when the time step is not chosen small enough.

So far, re-initialization has been extensively used as a numerical remedy for maintaining stable curve evolution and ensuring desirable results. From the practical viewpoints, the re-initialization process can be quite complicated, expensive, and have subtle side effects. Moreover, most of the level set methods are fraught with their own problems, such as when and how to re-initialize the level set function to a signed distance function. There is no simple answer that applies generally to date.

3.4.1.3 General Variational Level Set Formulation with Penalizing Energy

As discussed before, it is crucial to keep the evolving level set function as an approximate signed distance function during the evolution, especially in a neighbourhood around the zero level set. It is well known that a signed distance function must satisfy a desirable property of $|\nabla\phi| = 1$. Conversely, any function ϕ satisfying $|\nabla\phi|$=1 is the signed distance function plus a constant [19]. Naturally, we propose the following integral

$$P(\emptyset) = \int_{\Omega} \frac{1}{2}(|\nabla\phi| - 1)^2 dxdy \tag{3.19}$$

as a metric to characterize how close a function ϕ is to a signed distance function in $\Omega \subset \Re^2$ This metric will play a key role in Chunming Li's variational level set formulation. With the above defined functional $P(\phi)$, we propose the following variational formulation

$$\mathcal{E}(\phi) = \mu P(\phi) + \mathcal{E}_m(\phi) \tag{3.20}$$

where $\mu > 0$ is a parameter controlling the effect of penalizing the deviation of ϕ from a signed distance function, and $\mathcal{E}_m(\phi)$ is a certain energy that would drive the motion of the zero level curve of ϕ. We denote by $\frac{\partial\mathcal{E}}{\partial\phi}$ the Gateaux derivative (or first variation) of the functional $\mathcal{E}$, and the following evolution equation:

$$\frac{\partial\emptyset}{\partial t} = -\frac{\partial\varepsilon}{\partial\emptyset} \tag{3.21}$$

is the gradient flow that minimizes the functional $\mathcal{E}$. For a particular functional $\mathcal{E}(\phi)$ defined explicitly in terms of ϕ, the Gateaux derivative can be computed and expressed in terms of the function ϕ and its derivatives.

We will focus on applying the variational formulation in (3.20) to active contours for image segmentation, so that the zero level curve of ϕ can evolve to the desired features in the image. For this purpose, the energy $\mathcal{E}_m$will be defined as a functional that depends on image data, and therefore we call it the external energy. Accordingly, the energy $P(\phi)$ is called the internal energy of the function ϕ since it is a function of ϕ only.

During the evolution of ϕ according to the gradient flow (3.21) that minimizes the functional (3.20), the zero level curve will be moved by the external energy $\mathcal{E}_m$. Meanwhile, due to the penalizing effect of the internal energy, the evolving function ϕ will be

automatically maintained as an approximate signed distance function during the evolution according to the evolution (3.21). Therefore the re-initialization procedure is completely eliminated in the proposed formulation. This concept is demonstrated further in the context of active contours next.

3.4.1.4. Variational Level Set Formulation of Active Contours without Re-initialization

In image segmentation, active contours are dynamic curves that moves toward the object boundaries. To achieve this goal, we explicitly define an external energy that can move the zero level curve toward the object boundaries. Let I be an image, and g be the edge indicator function defined

$$g = \frac{1}{1 + |\nabla G_\sigma * I|^2} \tag{3.22}$$

where G_σ is the Gaussian kernel with standard deviation σ. We define an external energy for a function $\phi(x, y)$ as below

$$\mathcal{E}_{g,\lambda,\nu}(\phi) = \lambda \mathcal{L}_g(\phi) + \nu A_g(\phi) \tag{3.23}$$

where $\lambda > 0$ and ν are constants, and the terms $\mathcal{L}_g(\phi)$ and $A_g(\phi)$ are defined by

$$\mathcal{L}_g(\phi) = \int_\Omega g\delta(\phi)|\nabla\phi| dxdy$$

$$A_g(\phi) = \int_\Omega gH(-\phi) dxdy \tag{3.24}$$

respectively, where δ is the univariate Dirac function, and H is the Heaviside function. Now, we define the following total energy functional

$$\mathcal{E}(\phi) = \mu P(\phi) + \mathcal{E}_{g,\lambda,\nu}(\phi) \tag{3.25}$$

The external energy $\mathcal{E}_{g,\lambda,\nu}$drives the zero level set toward the object boundaries, while the internal energy $\mu P(\phi)$ penalizes the deviation of ϕ from a signed distance function during its evolution. To understand the geometric meaning of the energy, $\mathcal{L}_g(\phi)$we suppose that the zero level set of ϕ can be represented by a differentiable parameterized curve $C(p)$, $p \in [0, 1]$. It is well known that the energy functional $\mathcal{L}_g(\phi))$ computes the length of the zero level curve of ϕ in the conformal metric $ds = g\big(C(p)\big)\big|C'(p)\big|dp$. The energy functional $A_g(\phi)$ in (3.24) is introduced to speed up curve evolution. Note that, when the

function g is constant 1, the energy functional in (3.24) is the area of the region $\Omega_{\phi}^{-} = \{(x,y)|\phi(x,y) < 0\}$ [17]. The energy functional $A_g(\phi)$ in (3.24) can be viewed as the weighted area of Ω_{ϕ}^{-}. The coefficient ν of A_g can be positive or negative, depending on the relative position of the initial contour to the object of interest. For example, if the initial contours are placed outside the object, the coefficient ν in the weighted area term should take positive value, so that the contours can shrink faster. If the initial contours are placed inside the object, the coefficient ν should take negative value to speed up the expansion of the contours.

By calculus of variations , the Gateaux derivative (first variation) of the functional $\mathcal{E}$ in (3.25) can be written as

$$\frac{\partial \mathcal{E}}{\partial \phi} = -\mu\left[\Delta\phi - div\left(\frac{\nabla\phi}{|\nabla\phi|}\right)\right] - \lambda\delta(\phi)div(g\frac{\nabla\phi}{|\nabla\phi|} - \nu g\delta(\phi) \tag{3.26}$$

where Δ is the Laplacian operator. Therefore, the function ϕ that minimizes this functional satisfies the Euler-Lagrange equation $\frac{\partial \mathcal{E}}{\partial \phi} = 0$.The steepest descent process for minimization of the functional $\mathcal{E}$ is the following gradient flow:

$$\frac{\partial \phi}{\partial t} = \mu\left[\Delta\phi - div\left(\frac{\nabla\phi}{|\nabla\phi|}\right)\right] - \lambda\delta(\phi)div(g\frac{\nabla\phi}{|\nabla\phi|} - \nu g\delta(\phi) \tag{3.27}$$

this gradient flow is the evolution equation of the level set function in the proposed method.

The second and the third term in the right hand side of (3.27) correspond to the gradient flows of the energy functional $\mathcal{L}_g(\phi)$ and $\nu A_g(\phi)$, respectively, and are responsible of driving the zero level curve towards the object boundaries. To explain the effect of the first term, which is associated to the internal energy $\mu P(\phi)$, we notice that the gradient flow

$$\Delta\phi - div\left(\frac{\nabla\phi}{|\nabla\phi|}\right) = div\left[\left(1 - \frac{1}{|\nabla\phi|}\right)\nabla\phi\right] \tag{3.28}$$

has the factor $\left(1 - \frac{1}{|\nabla\phi|}\right)$ as diffusion rate. If $|\nabla\phi| > 1$, the diffusion rate is positive and the effect of this term is the usual diffusion, i.e. making ϕ more even and therefore reduce the gradient $|\nabla\phi|$. If $|\nabla\phi| < 1$, the term has effect of reverse diffusion and therefore increase the gradient.

This complete algorithm was implemented in MATLAB® for iris segmentation (Figure3.6). Initial contour was specified by using 'roipoly' command of MATLAB®, then level set evolution was done.

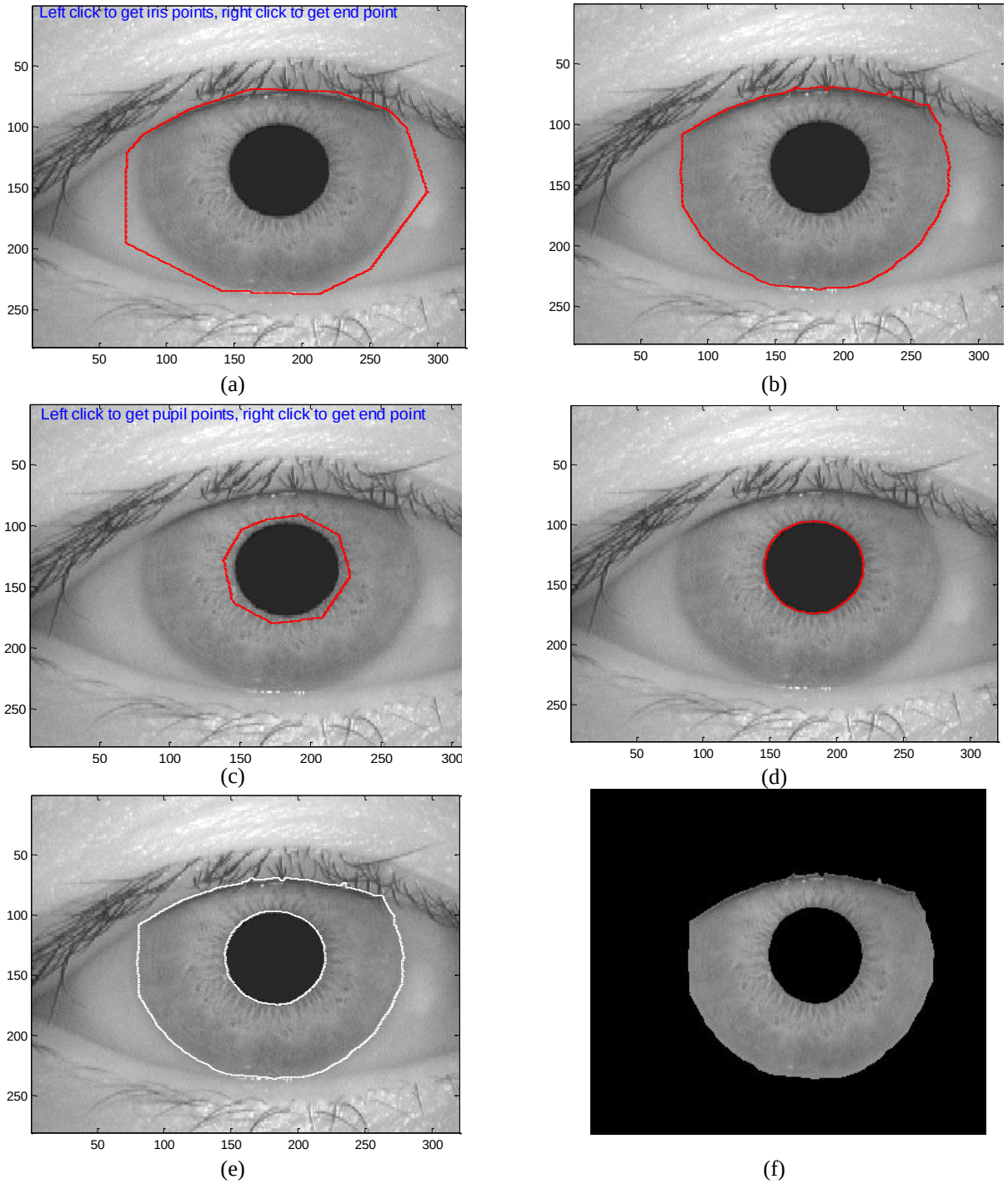

Figure 3.6: (a) Selected iris mask (b) iris/sclera boundary (c) selected pupil mask (d) iris/pupil boundary (e) segmented image (f) iris region.

3.5 Normalisation

Once the iris region is successfully segmented from an eye image, the next stage is to transform the iris region so that it has fixed dimensions in order to allow comparisons. The dimensional inconsistencies between eye images are mainly due to the stretching of the iris caused by pupil dilation from varying levels of illumination. Other sources of inconsistency include, varying imaging distance, rotation of the camera, head tilt, and rotation of the eye within the eye socket. The normalisation process will produce iris regions, which have the same constant dimensions, so that two photographs of the same iris under different conditions will have characteristic features at the same spatial location.

Another point of note is that the pupil region is not always concentric within the iris region, and is usually slightly nasal. This must be taken into account if trying to normalise the 'doughnut' shaped iris region to have constant radius.

3.5.1 Daugman Rubber Sheet

Due to the varying size of the pupil and of the distance and angle of the image capturing framework, the size of the captured irises can have high variations, increasing the complexity of the recognition task. Robust representations for pattern recognition must be invariant to changes in the size, position, and orientation of the patterns. In the iris recognition compass, this requires a representation of the iris data invariant to the dimension of the captured image. This is influenced by the distance between the eye and the capturing device, by the camera optical magnification factor and by the iris orientation, caused by torsional eye rotation and camera angles. As described in [22], the invariance to all of these factors can be achieved through the translation of the captured data into a double dimensionless polar coordinate system. As Figure 3.7 illustrates, this translation process is based both in polar (θ) and radial (r) variables.

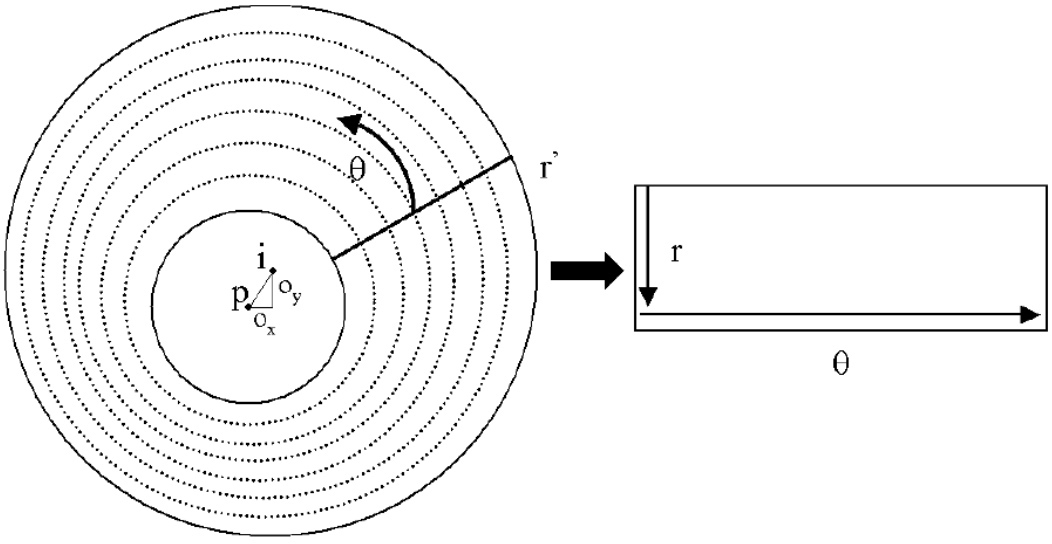

Figure 3.7: Normalization of the iris image through the Daugman rubber sheet.

The rubber sheet model assigns to each point on the iris, regardless of its size and pupillary dilation, a pair of real coordinates (r, θ), where r is on the unit interval $[0, 1]$ and (θ) is an angle in $[0, 2\pi]$. The remapping of the iris image $I(x, y)$ from raw Cartesian coordinates (x, y) to the dimensionless non concentric polar coordinate system (r, θ) can be represented as:

$$I\big(x(r,\theta), y(r,\theta)\big) \rightarrow I(r,\theta) \tag{3.29}$$

where $x(r, \theta)$ and $y(r, \theta)$, are defined as linear combinations of both the set of papillary boundary points $\big(x_p(\theta), y_p(\theta)\big)$ and the set of limbus boundary points along the outer perimeter of the iris $\big(x_s(\theta), y_s(\theta)\big)$ bordering the sclera, which are detected in the iris segmentation stage, as:

$$\begin{cases} x(r,\theta) = (1-r) * x_p(\theta) + r * x_s(\theta) \\ y(r,\theta) = (1-r) * y_p(\theta) + r * y_s(\theta) \end{cases} \tag{3.30}$$

3.5.2 Image Registration

The Wildes et al. system employs an image registration technique, which geometrically warps a newly acquired image, $I_a(x, y)$ into alignment with a selected database image $I_d(x, y)$. When choosing a mapping function $\big(u(x, y), v(x, y)\big)$ to transform the original coordinates, the image intensity values of the new image are made to be close to those of corresponding points in the reference image. The mapping function must be chosen so as to minimise

$$\int_x \int_y \big(I_d(x,y) - I_a(x-u, y-v)\big)^2 \, dx \, dy \tag{3.31}$$

While being constrained to capture a similarity transformation of image coordinates (x, y) to (x', y'), that is

$$\begin{pmatrix} x' \\ y' \end{pmatrix} = \begin{pmatrix} x \\ y \end{pmatrix} - sR(\phi) \begin{pmatrix} x \\ y \end{pmatrix} \tag{3.32}$$

With s a scaling factor and $R(\phi)$ a matrix representing rotation by ϕ. In implementation, given a pair of iris images I_a and I_d, the warping parameters s and ϕ are recovered via an iterative minimisation procedure.

3.5.3 Virtual Circles

In the Boles [23] system, iris images are first scaled to have constant diameter so that when comparing two images, one is considered as the reference image. This works differently to the other techniques, since normalisation is not performed until attempting to match two iris regions, rather than performing normalisation and saving the result for later comparisons. Once the two irises have the same dimensions, features are extracted from the iris region by storing the intensity values along virtual concentric circles, with origin at the centre of the

pupil. A normalisation resolution is selected, so that the number of data points extracted from each iris is the same. This is essentially the same as Daugman's rubber sheet model, however scaling is at match time, and is relative to the comparing iris region, rather than scaling to some constant dimensions. Also, it is not mentioned by Boles, how rotational invariance is obtained.

3.5.4 Implementation

For normalisation of iris regions a technique based on Daugman's rubber sheet model was employed. The centre of the pupil was considered as the reference point, and radial vectors pass through the iris region, as shown in Figure 3.7. A number of data points are selected along each radial line and this is defined as the radial resolution. The number of radial lines going around the iris region is defined as the angular resolution. Since the pupil can be non-concentric to the iris, a remapping formula is needed to rescale points depending on the angle around the circle. This is given by

$$r' = \sqrt{\alpha}\beta \pm \sqrt{\alpha\beta^2 - \alpha - r_I^2} \tag{3.33}$$

with

$$\alpha = o_x^2 + o_y^2 \tag{3.34}$$

$$\beta = \cos\left(\pi - \tan^{-1}\left(\frac{o_y}{o_x}\right) - \theta\right) \tag{3.35}$$

where displacement of the centre of the pupil relative to the centre of the iris is given by o_x, o_y , and r' is the distance between the edge of the pupil and edge of the iris at an angle, θ around the region, and r_I is the radius of the iris. The remapping formula first gives the radius of the iris region 'doughnut' as a function of the angle θ.

A constant number of points are chosen along each radial line, so that a constant number of radial data points are taken, irrespective of how narrow or wide the radius is at a particular angle. The normalised pattern was created by backtracking to find the Cartesian coordinates of data points from the radial and angular position in the normalised pattern. From the 'doughnut' iris region, normalisation produces a 2D array with horizontal dimensions of angular resolution and vertical dimensions of radial resolution. Another 2D array was created for marking reflections, eyelashes, and eyelids detected in the segmentation stage. In order to prevent non-iris region data from corrupting the normalised representation, data points which occur along the pupil border or the iris border are discarded.

Although the normalization method compensates variations due to scale, translation and pupil dilation, it is not inherently invariant to the rotation of iris. Rotation of an iris in the Cartesian coordinates is equivalent to a shift in the polar coordinates. In order to compensate the rotation of iris textures, a best of n test of agreement technique is proposed by Daugman in the matching process. In this method, iris templates are shifted and compared in n different directions to compensate the rotational effects.

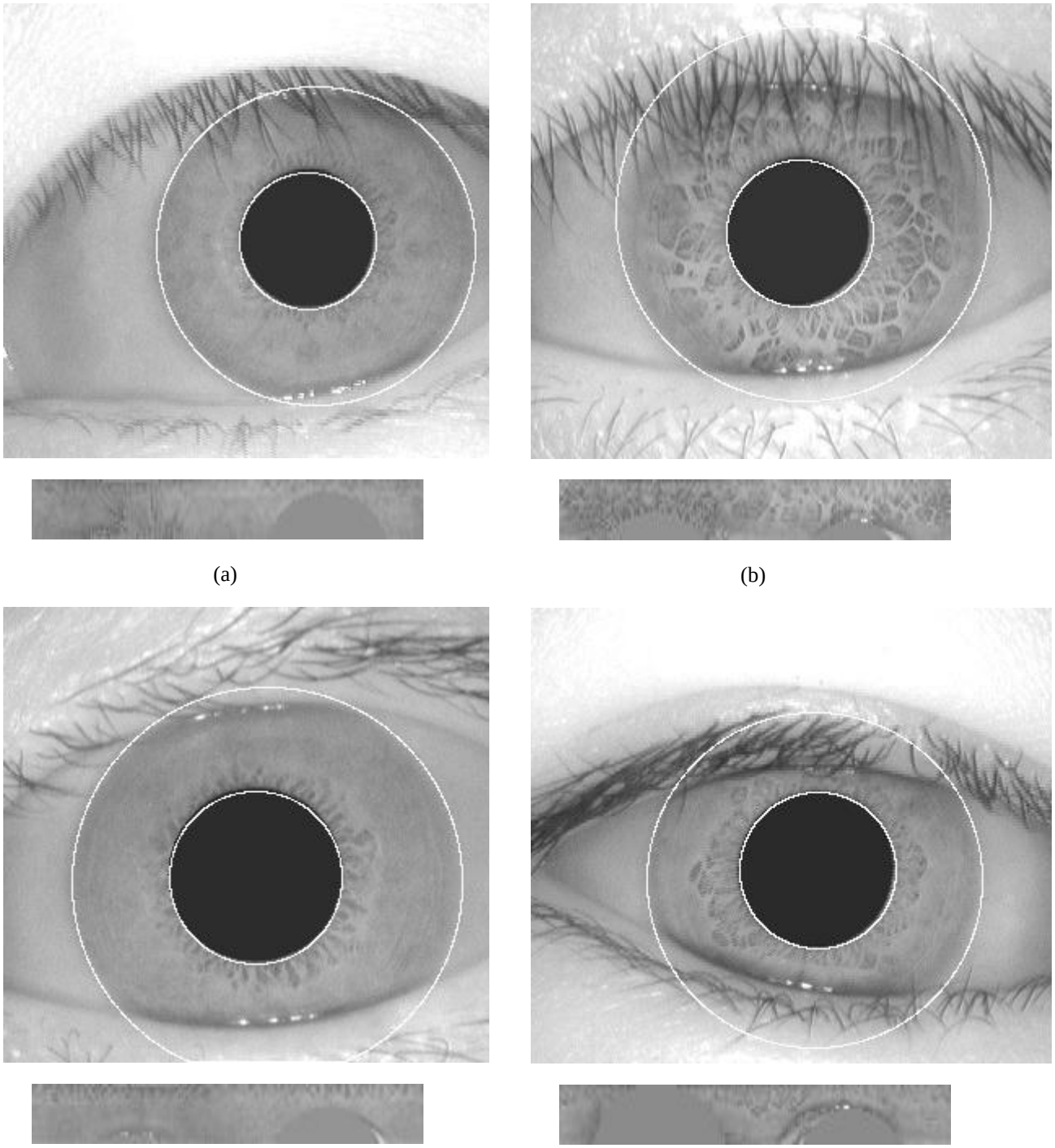

(a) (b)

(c) (d)

Figure 3.8: Segmented and corresponding normalized iris image using the Cartesian to polar transformation.

Chapter 4: Feature Encoding and Matching

In order to provide accurate recognition of individuals, the most discriminating information present in an iris pattern must be extracted. Only the significant features of the iris must be encoded so that comparisons between templates can be made. Most iris recognition systems make use of a band pass decomposition of the iris image to create a biometric template.

The template that is generated in the feature encoding process will also need a corresponding matching metric, which gives a measure of similarity between two iris templates. This metric should give one range of values when comparing templates generated from the same eye, known as intra-class comparisons, and another range of values when comparing templates created from different irises, known as inter-class comparisons. These two cases should give distinct and separate values, so that a decision can be made with high confidence as to whether two templates are from the same iris, or from two different irises.

4.1 Feature Encoding Algorithms

4.1.1 Wavelet Encoding

Wavelets can be used to decompose the data in the iris region into components that appear at different resolutions. Wavelets have the advantage over traditional Fourier transform in that the frequency data is localised, allowing features which occur at the same position and resolution to be matched up. A number of wavelet filters, also called a bank of wavelets, is applied to the 2D iris region, one for each resolution with each wavelet a scaled version of some basis function. The output of applying the wavelets is then encoded in order to provide a compact and discriminating representation of the iris pattern.

4.1.2 Gabor Filters

Gabor filters are able to provide optimum conjoint representation of a signal in space and spatial frequency. A Gabor filter is constructed by modulating a sine/cosine wave with a Gaussian. This is able to provide the optimum conjoint localisation in both space and frequency, since a sine wave is perfectly localised in frequency, but not localised in space. Modulation of the sine with a Gaussian provides localisation in space, though with loss of localisation in frequency. Decomposition of a signal is accomplished using a quadrature pair of Gabor filters, with a real part specified by a cosine modulated by a Gaussian, and an imaginary part specified by a sine modulated and odd symmetric components respectively.

The centre frequency of the filter is specified by the frequency of the sine/cosine wave, and the bandwidth of the filter is specified by the width of the Gaussian. Daugman makes uses of a 2D version of Gabor filters [22] in order to encode iris pattern data. A 2D Gabor filter over the an image domain (x, y) is represented as

$$G(x,y) = e^{-\pi[(x-x_0)^2/\alpha^2+(y-y_0)^2/\beta^2]} e^{-2\pi i[u_0(x-x_0)+v_0(y-y_0)]} \quad (4.1)$$

where (x_0, y_0) specify position in the image, (α, β) specify the effective width and length, and (u_0, v_0) specify modulation, which has spatial frequency $\omega_0 = \sqrt{u_0^2 + v_0^2}$.

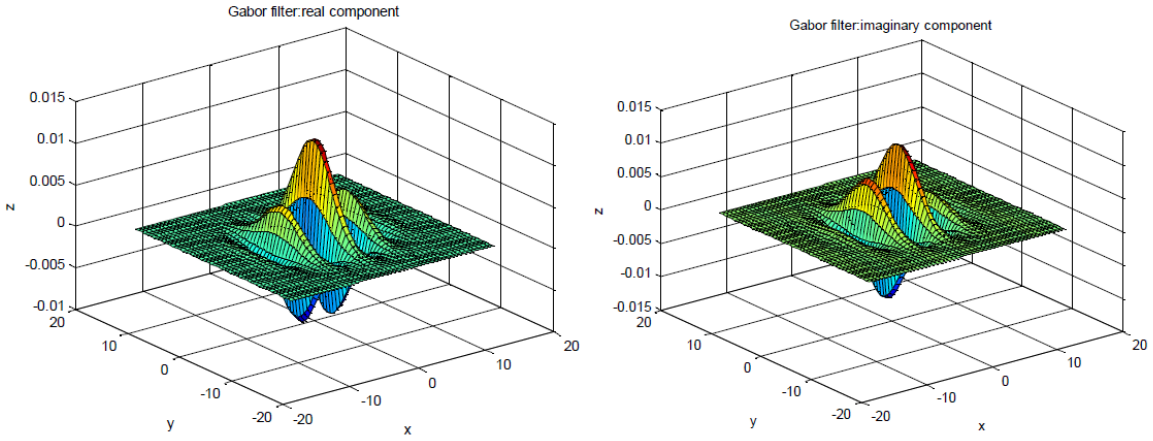

Figure 4.1: Shows the real and imaginary components of 2D Gabor filter.

Daugman demodulates the output of the Gabor filters in order to compress the data. This is done by quantising the phase information into four levels, for each possible quadrant in the complex plane. It has been shown by Oppenheim and Lim [42] that phase information, rather than amplitude information provides the most significant information within an image. Taking only the phase will allow encoding of discriminating information in the iris, while discarding redundant information such as illumination, which is represented by the amplitude component.

These four levels are represented using two bits of data, so each pixel in the normalised iris pattern corresponds to two bits of data in the iris template. A total of 2,048 bits are calculated for the template, and an equal number of masking bits are generated in order to mask out corrupted regions within the iris. This creates a compact 256-byte template, which allows for efficient storage and comparison of irises. The Daugman system makes use of polar coordinates for normalisation, therefore in polar form the filters are given as

$$H(r,\theta) = \frac{e^{-i\omega(\theta-\theta_0)} e^{-\frac{(r-r_0)^2}{\alpha^2}} e^{-i(\theta-\theta_0)^2}}{\beta^2} \tag{4.2}$$

where (α, β) are the same as in Equation 4.1 and (r_0, θ_0) specify the centre frequency of the filter.

The demodulation and phase Quantisation process can be represented as

$$h_{\{Re,Im\}} = sgn_{\{Re,Im\}} \int_{\rho} \int_{\phi} I(\rho,\phi) e^{-\omega(\theta_0-\phi)} e^{-(r_0-\rho)^2/\alpha^2} e^{-(\theta_0-\phi)^2/\beta^2} \rho d\rho d\phi \tag{4.3}$$

Where $h_{\{Re,Im\}}$ can be regarded as a complex valued bit whose real and imaginary components are dependent on the sign of the 2D integral, and $I(\rho,\phi)$ is the raw iris image in a dimensionless polar coordinate system.

4.1.3 Log-Gabor Filters

A disadvantage of the Gabor filter is that the even symmetric filter will have a DC component whenever the bandwidth is larger than one octave [51]. However, zero DC component can be obtained for any bandwidth by using a Gabor filter which is Gaussian on a logarithmic scale, this is known as the Log-Gabor filter. The frequency response of a Log-Gabor filter is given as:

$$G(f) = \exp\left(\frac{-(\log(f/f_0))^2}{2(\log(\sigma/f_0))^2}\right) \tag{4.4}$$

where $f_0$represents the centre frequency, and σ gives the bandwidth of the filter.

4.1.4 Zero-crossings of the 1D wavelet

Boles and Boashash [23] make use of 1D wavelets for encoding iris pattern data. The mother wavelet is defined as the second derivative of a smoothing function $\theta(x)$.

$$\psi(x) = \frac{d^2\theta(x)}{dx^2} \tag{4.5}$$

The zero crossings of dyadic scales of these filters are then used to encode features. The wavelet transform of a signal $f(x)$ at scale s and position x is given by :

$$W_s f(x) = f * \left(s^2 \frac{d^2\theta(x)}{dx^2}\right)(x) \tag{4.6}$$

$$= s^2 \frac{d^2}{dx^2}(F * \theta_s)(x) \tag{4.7}$$

where

$$\theta_s = (1/s)\theta(x/s) \tag{4.8}$$

$W_s f(x)$ is proportional to the second derivative of $f(x)$ smoothed by $\theta_s(x)$, and the zero crossings of the transform correspond to points of inflection in $F * \theta_s(x)$. The motivation for this technique is that zero-crossings correspond to significant features with the iris region.

4.1.5 Haar Wavelet

Lim et al. [42] also use the wavelet transform to extract features from the iris region. Both the Gabor transform and the Haar wavlet are considered as the mother wavelet. From multi-dimensionally filtering, a feature vector with 87 dimensions is computed. Since each dimension has a real value ranging from -1.0 to $+1.0$, the feature vector is sign quantised so

that any positive value is represented by 1, and negative value as 0. This results in a compact biometric template consisting of only 87 bits.

Lim et al. compare the use of Gabor transform and Haar wavelet transform, and show that the recognition rate of Haar wavelet transform is slightly better than Gabor transform by 0.9%.

4.1.6 Laplacian of Gaussian Filters

In order to encode features, the Wildes et al. system decomposes the iris region by application of Laplacian of Gaussian filters to the iris region image. The filters are given as

$$\nabla G = -\frac{1}{\pi\sigma^4}\left(1-\frac{\rho^2}{2\sigma^2}\right)e^{-\rho^2/2\sigma^2} \tag{4.9}$$

where σ is the standard deviation of the Gaussian and ρ is the radial distance of a point from the centre of the filter.

The filtered image is represented as a Laplacian pyramid which is able to compress the data, so that only significant data remains. Details of Laplacian Pyramids are presented by Burt and Adelson [53]. A Laplacian pyramid is constructed with four different resolution levels in order to generate a compact iris template.

4.2 Feature Matching Algorithms

4.2.1 Hamming Distance

The Hamming distance gives a measure of how many bits are the same between two bit patterns. Using the Hamming distance of two bit patterns, a decision can be made as to whether the two patterns were generated from different irises or from the same one.

In comparing the bit patterns X and Y, the Hamming distance, HD, is defined as the sum of disagreeing bits (sum of the exclusive-OR between X and Y) over N, the total number of bits in the bit pattern.

$$HD = \frac{1}{N}\sum_{j=1}^{N} X_j \otimes Y_j \tag{4.10}$$

Since an individual iris region contains features with high degrees of freedom, each iris region will produce a bit-pattern which is independent to that produced by another iris, on the other hand, two iris codes produced from the same iris will be highly correlated.

If two bits patterns are completely independent, such as iris templates generated from different irises, the Hamming distance between the two patterns should equal 0.5. This occurs because independence implies the two bit patterns will be totally random, so there is 0.5 chance of setting any bit to 1, and vice versa. Therefore, half of the bits will agree and half will disagree between the two patterns. If two patterns are derived from the same iris, the

Hamming distance between them will be close to 0.0, since they are highly correlated and the bits should agree between the two iris codes.

The Hamming distance is the matching metric employed by Daugman, and calculation of the Hamming distance is taken only with bits that are generated from the actual iris region.

4.2.2 Weighted Euclidean Distance

The weighted Euclidean distance (WED) can be used to compare two templates, especially if the template is composed of integer values. The weighting Euclidean distance gives a measure of how similar a collection of values are between two templates. This metric is employed by Zhu et al. [54] and is specified as

$$WED(k) = \sum_{i=1}^{N} \frac{\left(f_i - f_i^{(k)}\right)^2}{\left(\delta_i^{(k)}\right)^2} \tag{4.11}$$

where f_i is the ith feature of the unknown iris, and $f_i^{(k)}$ is the ith feature of iris template, k, and $\delta_i^{(k)}$ is the standard deviation of the ith feature in iris template k. The unknown iris template is found to match iris template k, when WED is a minimum at k.

4.2.3 Normalised Correlation

Wildes et al. make use of normalised correlation between the acquired and database representation for goodness of match. This is represented as

$$\sum_{i=1}^{n}\sum_{j=1}^{m}(p_1[i,j] - \mu_1)(p_2[i,j] - \mu_2) \Big/ nm\sigma_1\sigma_2 \tag{4.12}$$

where p_1 and p_2 are two images of size $n \times m$, μ_1 and σ_1 are the mean and standard deviation of p_1, and μ_2 and σ_2 are the mean and standard deviation of p_2.

Normalised correlation is advantageous over standard correlation, since it is able to account for local variations in image intensity that corrupt the standard correlation calculation.

4.3 Implementation

4.3.1 Feature Encoding

Feature encoding was implemented by convolving the normalised iris pattern with 1D Log-Gabor wavelets. The 2D normalised pattern is broken up into a number of 1D signals, and then these 1D signals are convolved with 1D Gabor wavelets. The rows of the 2D normalised pattern are taken as the 1D signal, each row corresponds to a circular ring on the iris region. The angular direction is taken rather than the radial one, which corresponds to columns of the normalised pattern, since maximum independence occurs in the angular direction.

The intensity values at known noise areas in the normalised pattern are set to the average intensity of surrounding pixels to prevent influence of noise in the output of the filtering. The output of filtering is then phase quantised to four levels using the Daugman method [22], with each filter producing two bits of data for each phasor. The output of phase quantisation is chosen to be a grey code, so that when going from one quadrant to another, only 1 bit changes. This will minimise the number of bits disagreeing, if say two intra-class patterns are slightly misaligned and thus will provide more accurate recognition. The feature encoding process is illustrated in Figure 4.3.

The encoding process produces a bitwise template containing a number of bits of information, and a corresponding noise mask which corresponds to corrupt areas within the iris pattern, and marks bits in the template as corrupt. Since the phase information will be meaningless at regions where the amplitude is zero, these regions are also marked in the noise mask. The total number of bits in the template will be the angular resolution times the radial resolution, times 2, times the number of filters used.

4.3.2 Matching

For matching, the Hamming distance was chosen as a metric for recognition, since bit-wise comparisons were necessary. The Hamming distance algorithm employed also incorporates noise masking, so that only significant bits are used in calculating the Hamming distance between two iris templates. Now when taking the Hamming distance, only those bits in the iris pattern that correspond to 0 bits in noise masks of both iris patterns will be used in the calculation. The Hamming distance will be calculated using only the bits generated from the true iris region, and this modified Hamming distance formula is given as

$$HD = \left(1 \Big/ N - \sum_{k=1}^{N} Xn_k (OR) Yn_k\right) * \sum_{j=1}^{N} X_j (XOR) Y_j (AND) Xn_j^{'} (AND) Yn_j^{'} \qquad (4.13)$$

where X_j and Y_j are the two bit-wise templates to compare, $Xn_j^{'}$and $Yn_j^{'}$are the corresponding noise masks for X_j and X_j, and N is the number of bits represented by each template.

Although, in theory, two iris templates generated from the same iris will have a Hamming distance of 0.0, in practice this will not occur. Normalisation is not perfect, and also there will be some noise that goes undetected, so some variation will be present when comparing two intra-class iris templates.

In order to account for rotational inconsistencies, when the Hamming distance of two templates is calculated, one template is shifted left and right bit-wise and a number of Hamming distance values are calculated from successive shifts. This bit-wise shifting in the horizontal direction corresponds to rotation of the original iris region by an angle given by the angular resolution used. If an angular resolution of 180 is used, each shift will correspond to a rotation of 2 degrees in the iris region. This method is suggested by Daugman [22], and corrects for misalignments in the normalised iris pattern caused by rotational differences during imaging. From the calculated Hamming distance values, only the lowest is taken, since this corresponds to the best match between two templates.

The number of bits moved during each shift is given by two times the number of filters used, since each filter will generate two bits of information from one pixel of the normalised region. The actual number of shifts required to normalise rotational inconsistencies will be determined by the maximum angle difference between two images of the same eye, and one shift is defined as one shift to the left, followed by one shift to the right. The shifting process for one shift is illustrated in Figure 4.4.

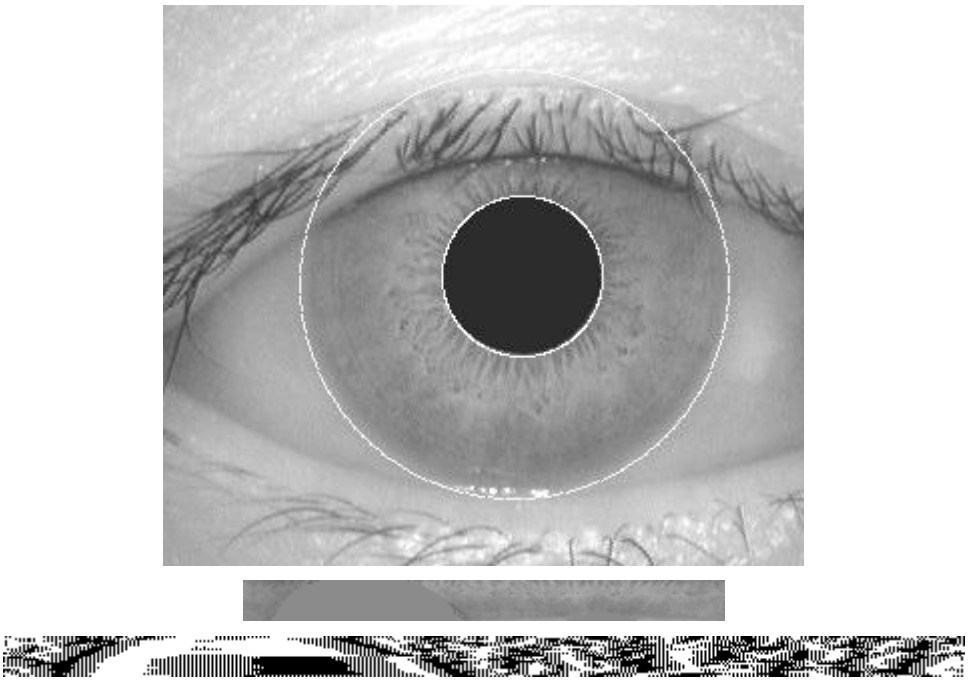

(a)

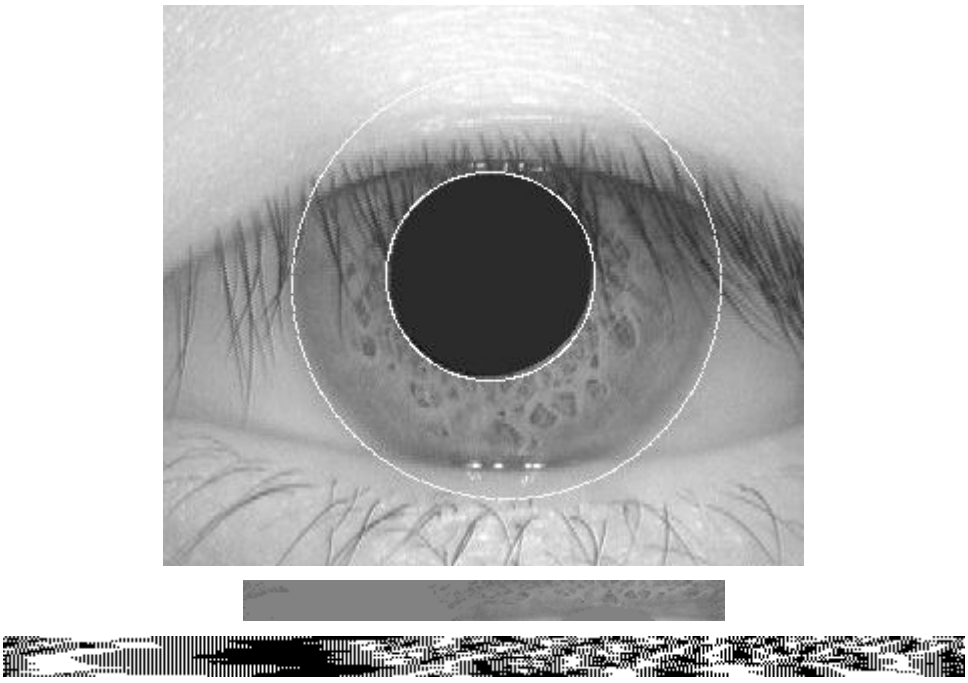

(b)

Figure 4.2: Segmented image with corresponding normalized image and iris code

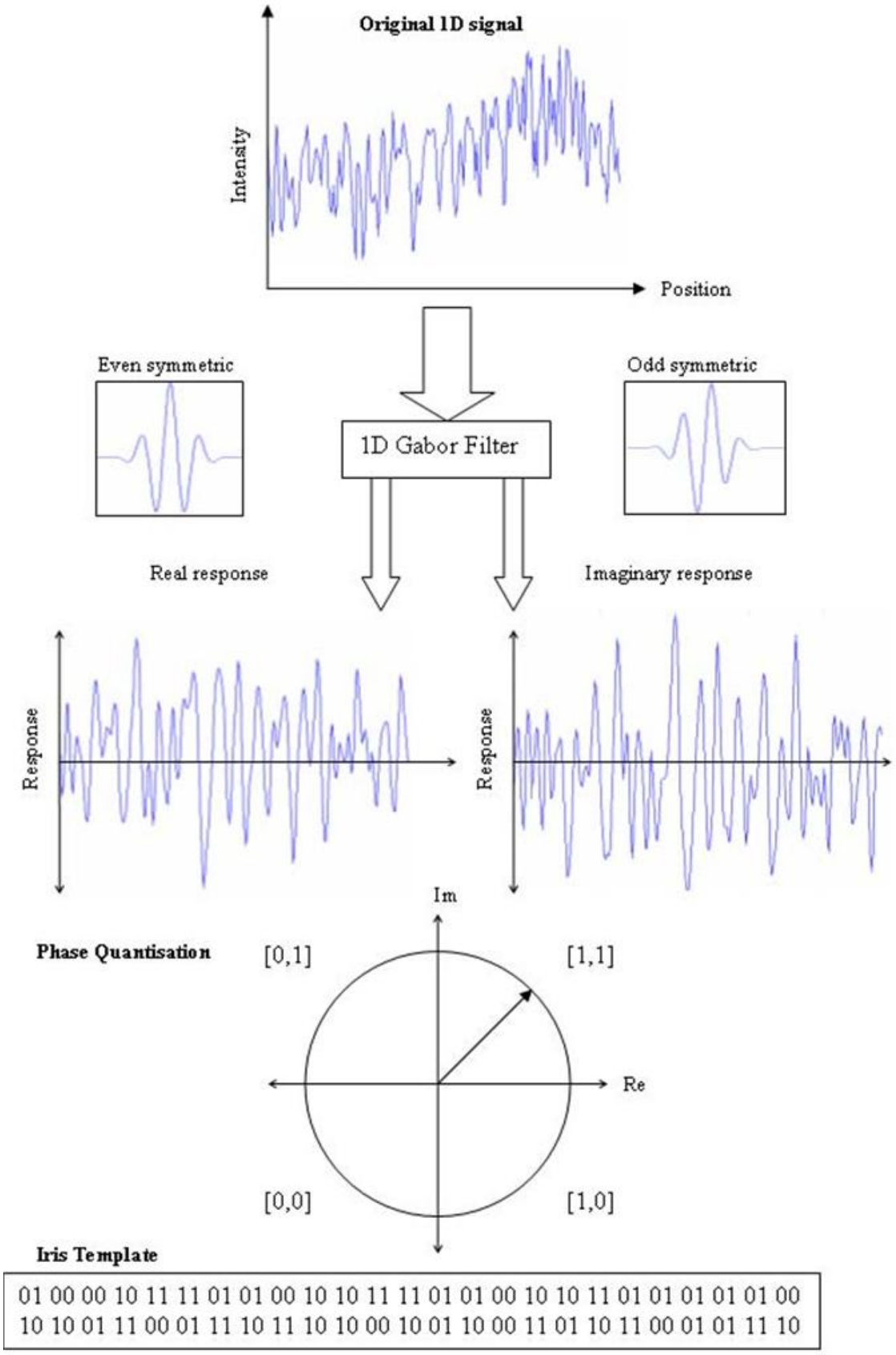

Figure 4.3: An illustration of the feature encoding process

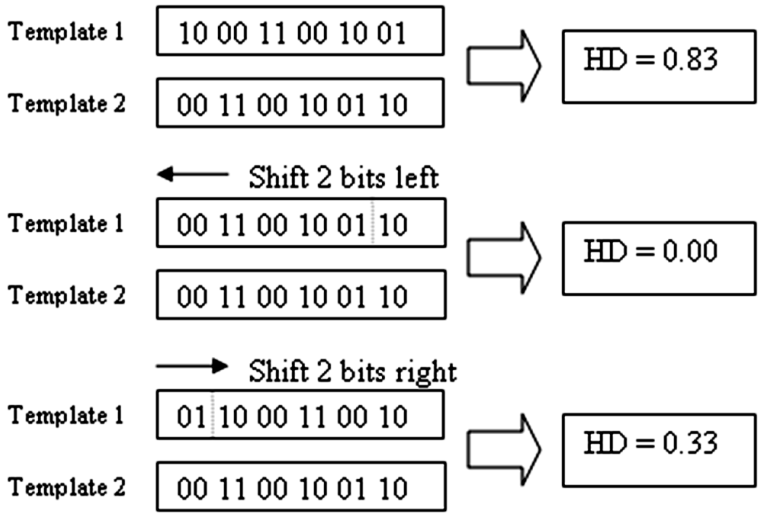

Figure 4.4: An illustration of the shifting process. One shift is defined as one shift left, and one shift right of a reference template. In this example one filter is used to encode the templates, so only two bits are moved during a shift. The lowest Hamming distance, in this case zero, is then used since this corresponds to the best match between the two templates.

Chapter 5: Results

5.1 Segmentation

The automatic segmentation model using Integrodifferential equations and Hough transform proved to be successful. The CASIA database provided good segmentation, since those eye images had been taken specifically for iris recognition research and boundaries of iris pupil and sclera were clearly distinguished. For the CASIA database, the Hough transform based segmentation technique managed to correctly segment the iris region from 658 out of 756 eye images, which corresponds to a success rate of around 87% as compared to the Hough transform based segmentation technique that managed to correctly segment the iris region from 624 out of 756 eye images, which corresponds to a success rate of around 83%.

Using Integrodifferential equations and Hough transform methods on locating the pupil and limbus assume that the boundaries are perfect circles. Although the approaches are different, all these methods consider pupil and limbus as circular curves. It has been noticed that the circular assumption of the contours can lead to inappropriate boundary detection. In Figures 5.1 and 5.3, some of the iris images from the CASIA database are shown that the pupil boundaries are not perfect circles.

The above methods of segmentation resulted in false detection due to noises such as strong boundaries of upper and lower eyelids. The strong eyelid boundaries and presence of eyelashes affected the limbus localization significantly.

We also implemented eyelashes and eyelids detection for the above two methods. The eyelid detection system proved quite successful, and managed to isolate most occluding eyelid regions. One problem was that it would sometimes isolate too much of the iris region, which could make the recognition process less accurate, since there is less iris information. However, this is preferred over including too much of the iris region, if there is a high chance it would also include undetected eyelash and eyelid regions.

The eyelash detection system implemented for the CASIA database also proved to be successful in isolating most of the eyelashes occurring within the iris region as shown in Figure 5.7. A slight problem was that areas where the eyelashes were light, such as at the tips were not detected. However, these undetected areas were small when compared with the size of the iris region.

The proposed method of active contour segmentation based on Level set evolution without re-initialization provided perfect segmentation results for the pupil and limbus boundaries with success rate of almost 100%. Only problem with this system was that the initial contour was to be defined for each eye image manually.

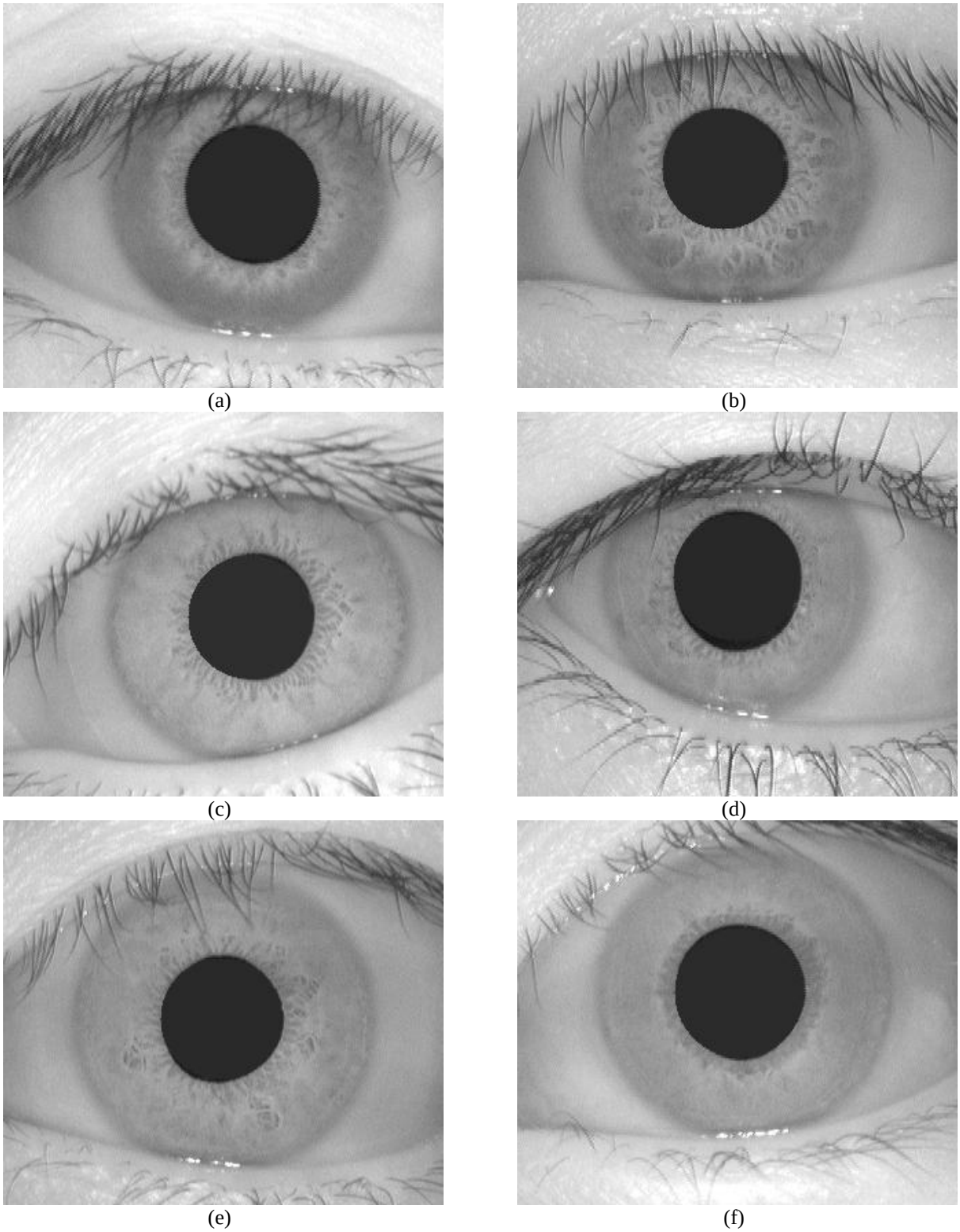

(a) (b)

(c) (d)

(e) (f)

Figure 5.1: Illustrates pupil that are not perfect circles.

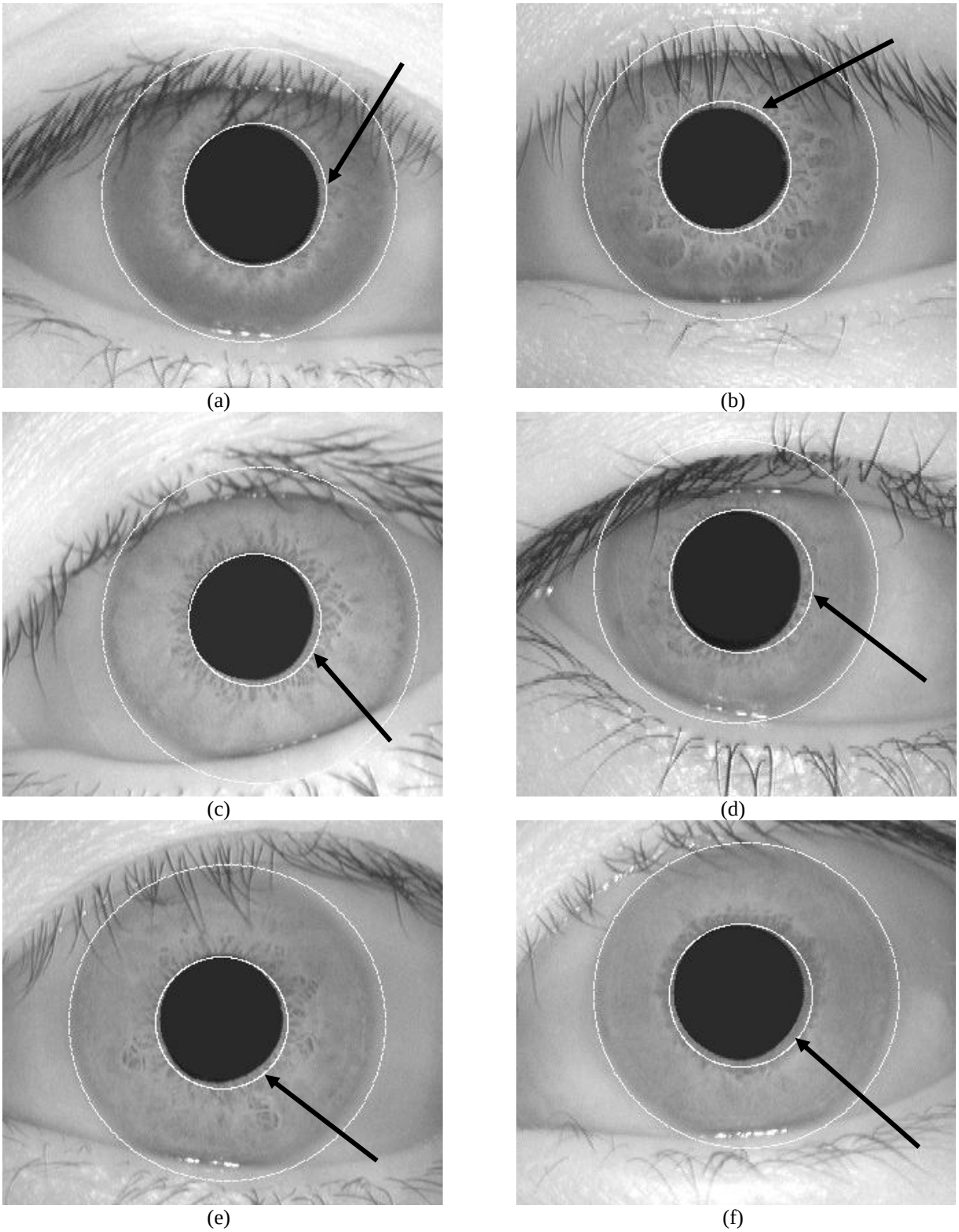

(a) (b) (c) (d) (e) (f)

Figure 5.2: Illustrate the results of the Integrodifferential operator over the pupils that are not perfect circles. The circular contour does not detect pupil boundaries accurately.

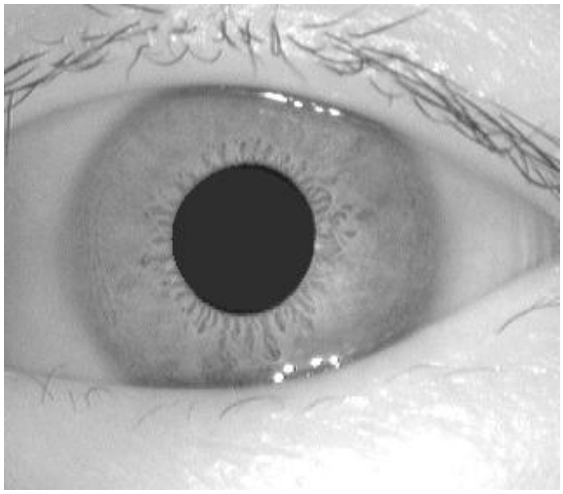

(a)

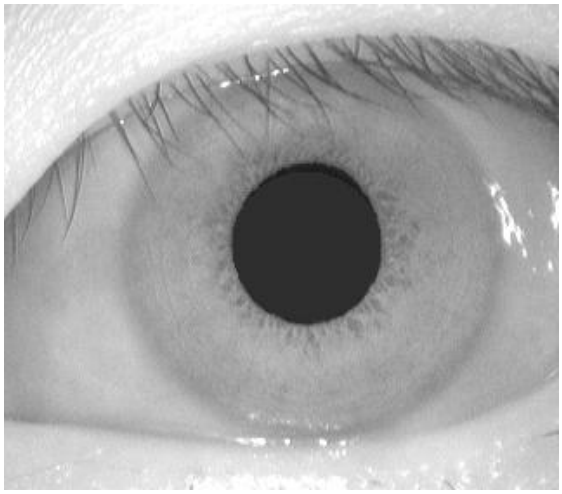

(b)

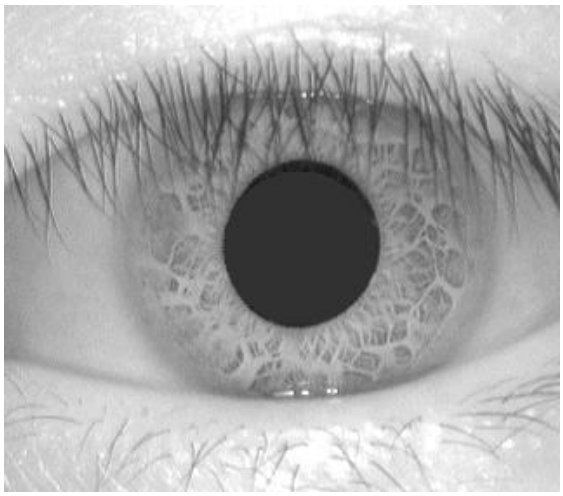

(c)

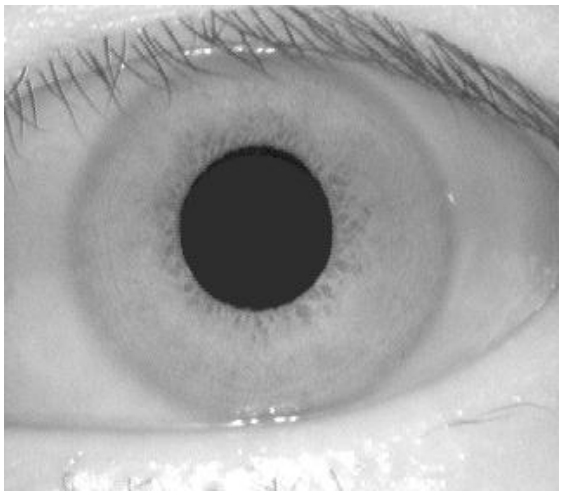

(c)

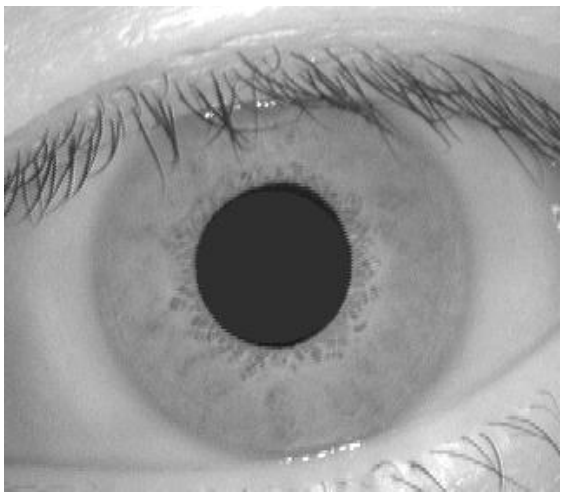

(e)

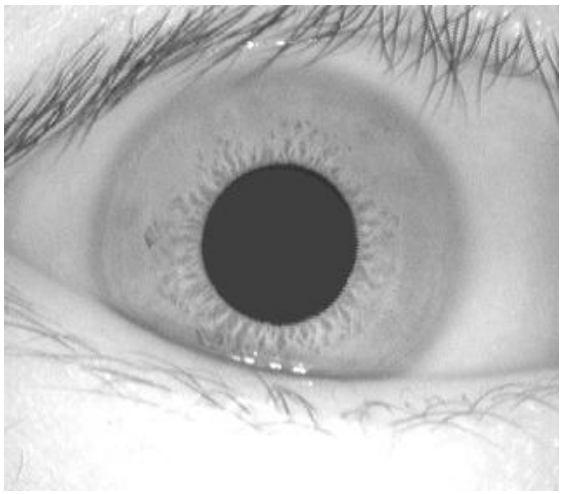

(f)

Figure 5.3: Illustrates pupil that are not perfect circles.

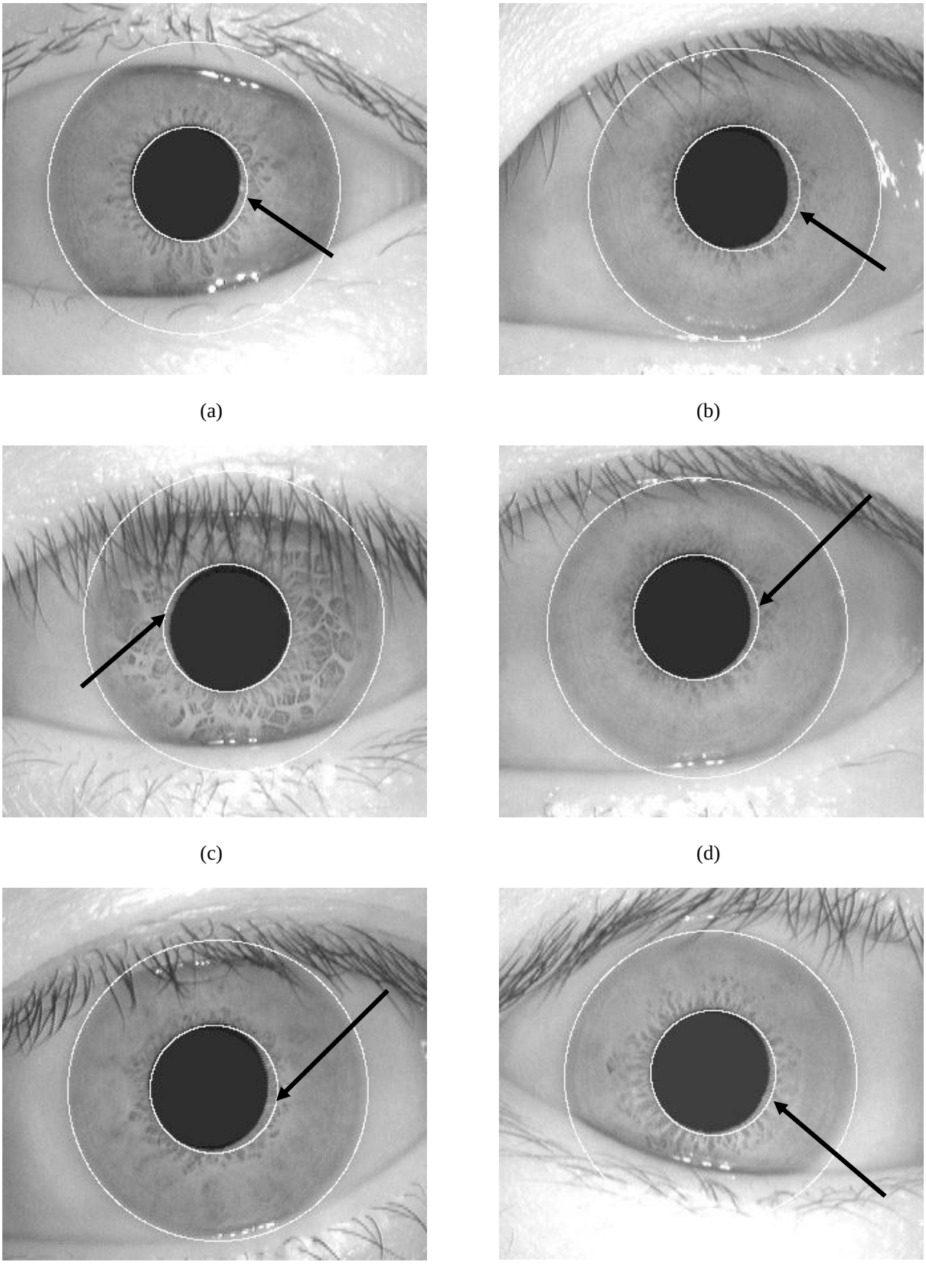

(a) (b)

(c) (d)

(e) (f)

Figure 5.4: Illustrate the results of the Hough transform operator over the pupils that are not perfect circles. The circular contour does not detect pupil boundaries accurately.

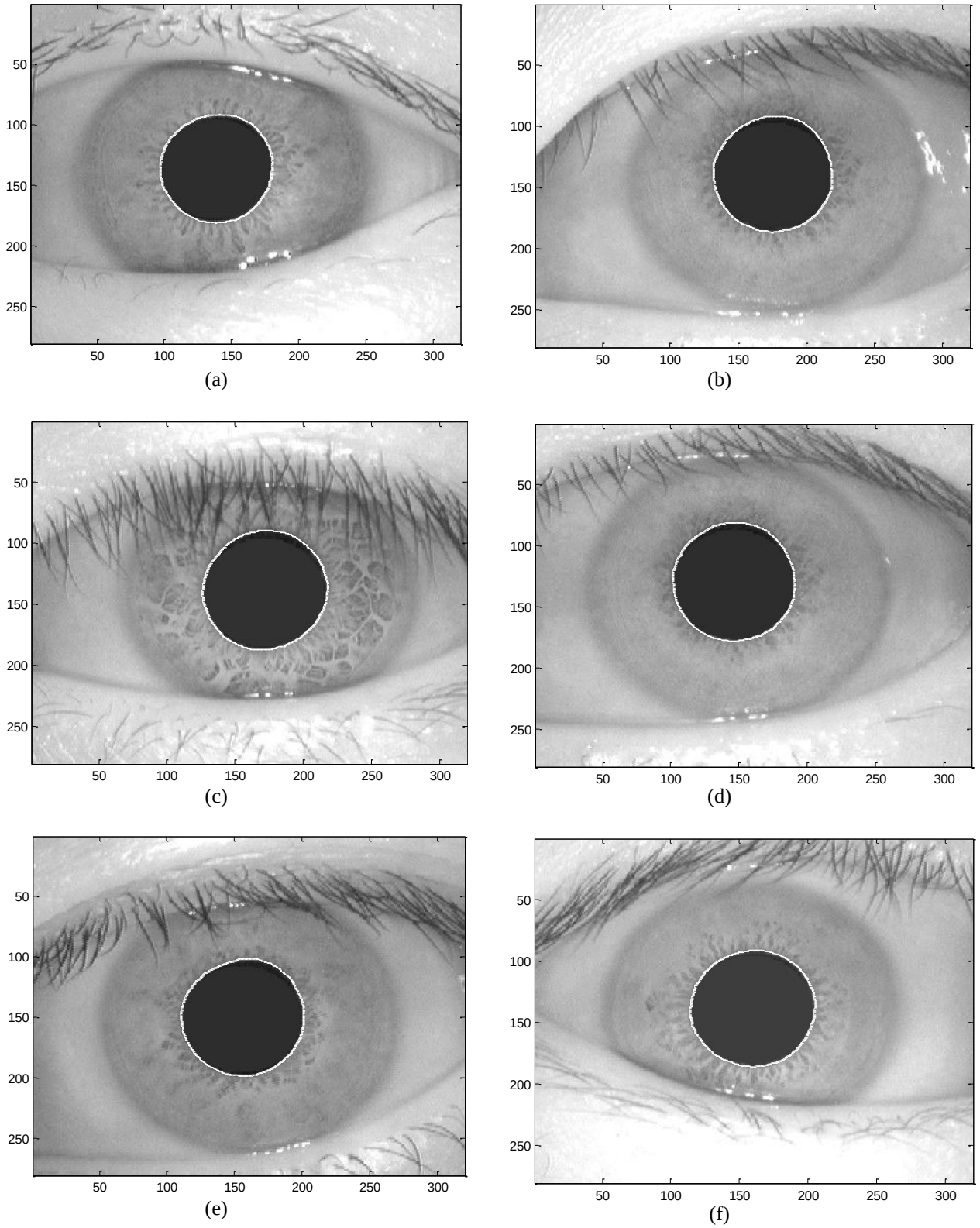

Figure 5.5: Illustrate the results of the active contour segmentation method based on Level set evolution without re-initialization over the pupils that are not perfect circles.

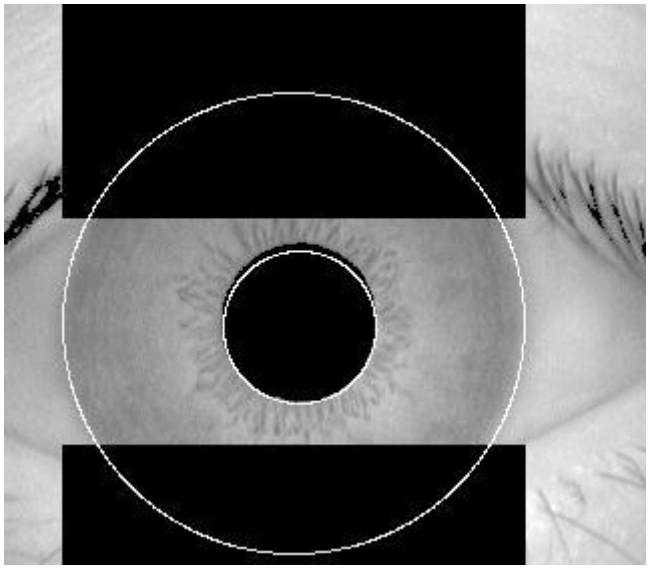

Figure 5.6: Automatic segmentation of image from CASIA database. Black region denote detected eyelid.

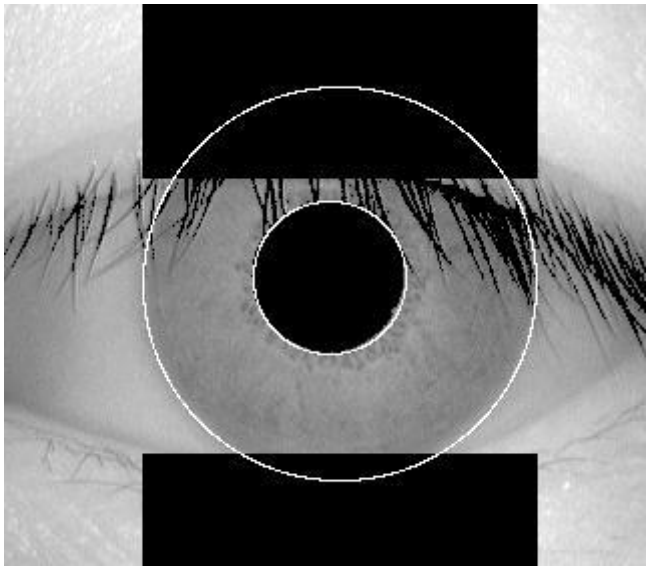

Figure 5.7: The eyelash detection technique, eyelash regions are detected using thresholding and denoted as black.

5.2 Normalization

The normalisation process proved to be successful and some results are shown in Figure 3.9. However, the normalisation process was not able to perfectly reconstruct the same pattern from images with varying amounts of pupil dilation, since deformation of the iris results in small changes of its surface patterns.

Normalisation of two eye images of the same iris is shown in Figure 5.9. The pupil is smaller in the bottom image, however the normalisation process is able to rescale the iris region so that it has constant dimension.

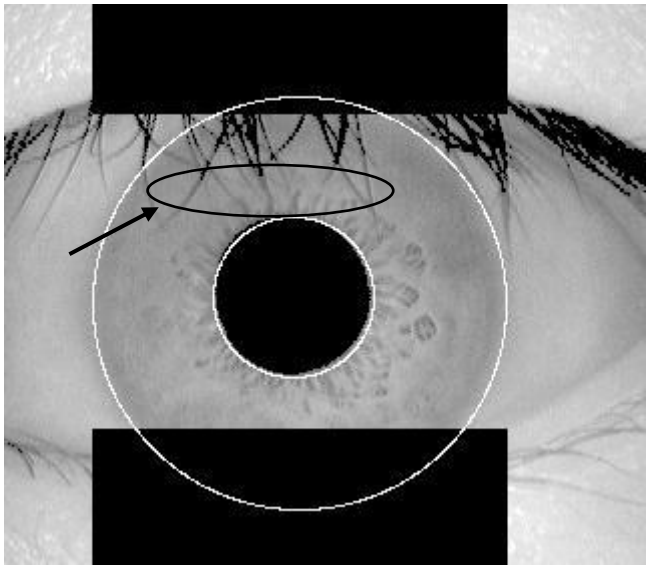

Figure 5.8: Eyelashes not detected because of their light colour at the tips.

.

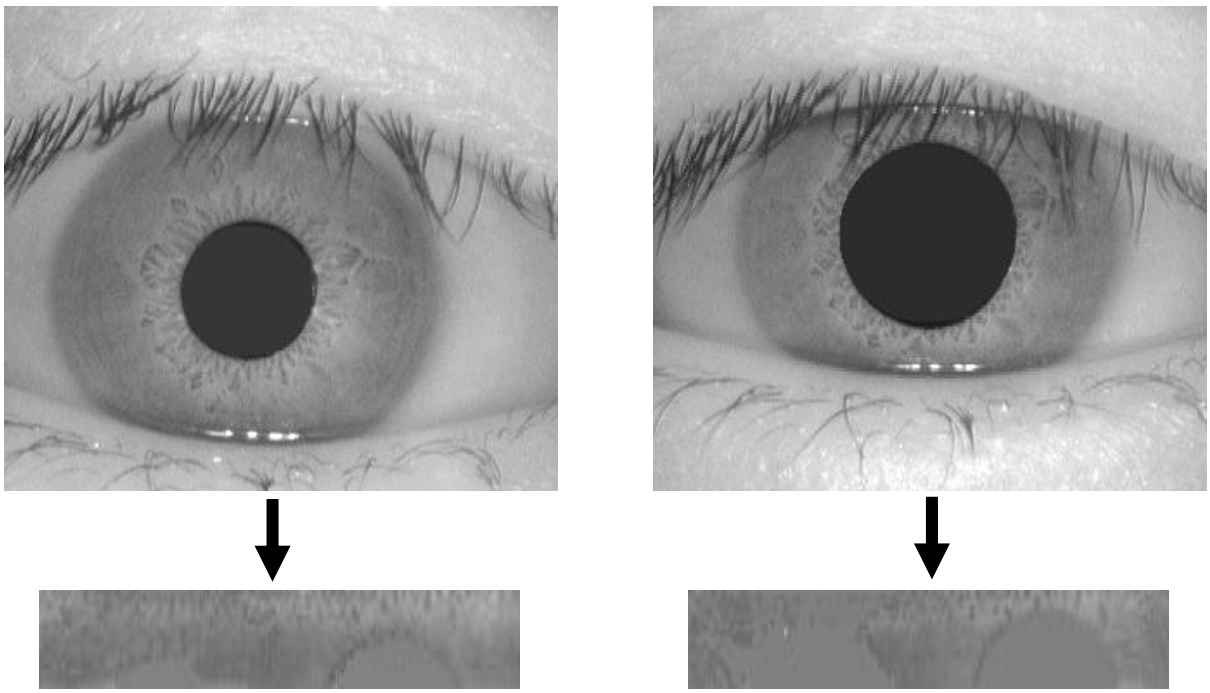

Figure 5.9: Illustration of the normalisation process for two images of the same iris taken under varying conditions.

Table 5.1: Comparison of different segmentation techniques.

Method	No. Of eye images	Properly Segmented	Accuracy
Daugman's Method	756	658	87%
Hough Transform	756	624	83%
Proposed Method	756	750	Approx: 100%

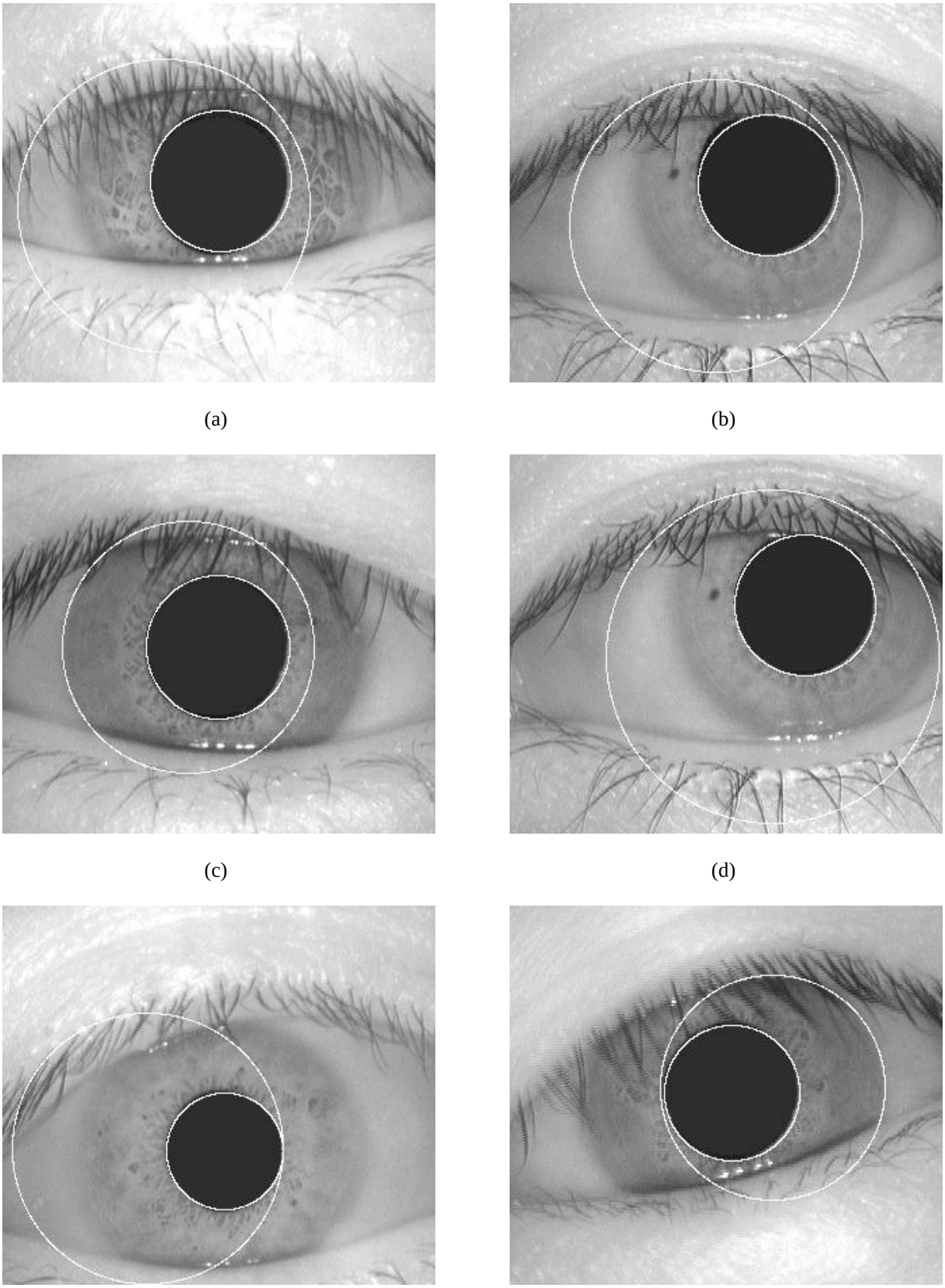

(a) (b)

(c) (d)

(e) (f)

Figure 5.10: Improper image segmentation using Hough transforms.

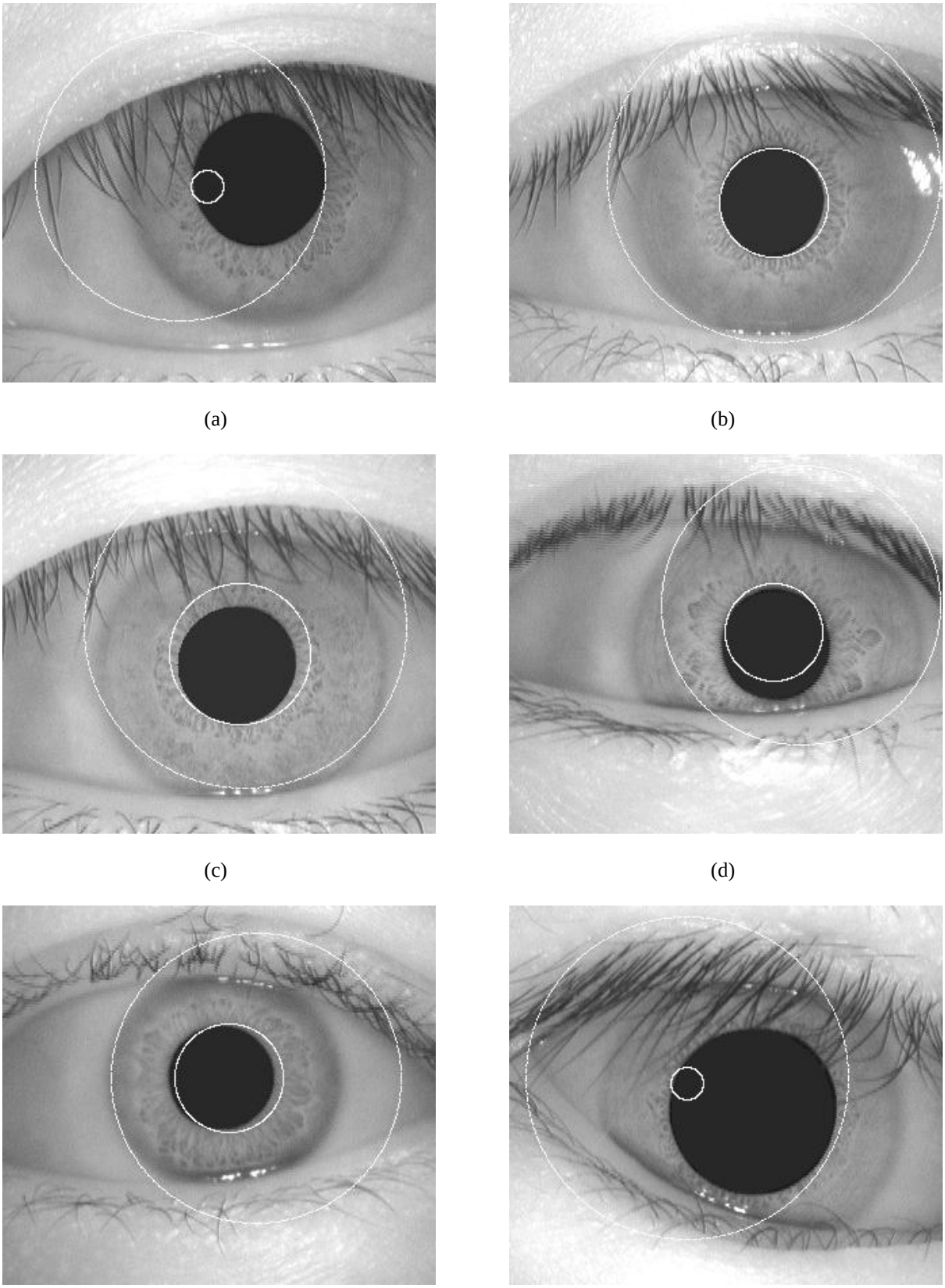

(a) (b)

(c) (d)

(e) (f)

Figure 5.11: Improper iris segmentation using Daugman's method.

Chapter 6: Conclusion

Comparison between the most common biometric traits was done based on the following seven parameters: uniqueness, universality, permanence, collectability, performance, acceptability and circumvention. Apart from being the biometric trait with highest average value between the seven analyzed parameters (84.42%), its simultaneous high levels for uniqueness, permanence, universality and circumvention turned the iris into the most appropriate for our work and a natural choice towards the biometric iris recognition.

In this thesis Daugman, Wildes and Active contour based algorithms were implemented in order to evaluate the impact of different segmentation and normalization methods on the overall performance, 756 properly localized iris images were used in all the experiments.

Daugman's method has one important advantage: it is not dependent of any parameter value. This fact may, in theory, potentiate its robustness, but the results showed that its accuracy is influenced by the images quality, namely the requirements of a sufficient separability between the intensities of the iris and sclera regions. Specially in the iris images with higher intensity values (blue or green irises), where the intensity difference between the iris and sclera regions is not as large, the method's seek strategy for the maximal difference between consecutive circumferences tends to identify regions tangent to the pupil region, which have considerable high contrast. Eyelids and eyelashes occlusion also degraded segmentation using Daugman's and Wildes's method.

For the CASIA database, the Hough transform based segmentation technique managed to correctly segment the iris region from 658 out of 756 eye images, which corresponds to a success rate of around 87% as compared to the Hough transform based segmentation technique that managed to correctly segment the iris region from 624 out of 756 eye images, which corresponds to a success rate of around 83%.

Properly detecting the inner and outer boundaries of iris texture is important for all iris recognition systems. The irregular boundary of pupil was the motivation of designing an active contour for detecting the boundary accurately. A new method was implemented based on variational formulation given by Chunming Li for geometric active contours, it takes into consideration that an actual pupil boundary is a near-circular contour rather than a perfect circle. The proposed method perfect segmentation results for the pupil and limbus boundaries with success rate of almost 100%. Only problem with this system was that the initial contour was to be defined for each eye image manually. The normalisation process proved to be successful but it was not able to perfectly reconstruct the same pattern from images with varying amounts of pupil dilation, since deformation of the iris results in small changes of its surface patterns.

REFERENCES

[1] R. Duda, P. Hart, and D. Stork, *Pattern Classification*, Wiley Interscience, New York, 2001.

[2] A. K. Jain, S. Pankanti, S. Prabhakar, Lin Hong, A. Ross, and J. L. Wayman, "Biometrics: A grand challenge," *Proceedings of the 17th International Conference on Pattern Recognition* (*ICPR*), pp. 935–942, Cambridge, December 2004.

[3] Wikipedia, http://en.wikipedia.org/wiki/Biometric.

[4] Data Core Technology, http://www.data-core.com/glossary-of-terms.htm, 2010.

[5] WhatIs Dictionary, http://whatis.techtarget.com/, 2010.

[6] M. Bromba, Biometrics FAQ's, http://www.bromba.com/faq/biofaqe.htm, 2010.

[7] J. D. Woodward, C. Horn, J. Gatune, and A. Thomas, *Biometrics: A look at facial recognition*, Rand Corporation, Santa Monica, 2003.

[8] The Bertillon System, http://criminaljustice.state.ny.us/ojis/history/ph_measr.htm, 2010.

[9] M. Bellis, "Inventors: Police technology and forensic science," http://inventors.about.com/library/inventors/blforensic.htm, 2010.

[10] V. Matyas and Z. Riha, "Toward reliable user authentication through biometrics," *IEEE Security and Privacy*, vol. 1, no. 3, pp. 45–49, 2003.

[11] J. G. Daugman, "Phenotypic versus genotypic approaches to face recognition," *Face Recognition: From Theory to Applications*, pp. 108–123. Heidelberg: Springer-Verlag, 1998.

[12] S. D. Fried, "Domain access control systems and methodology," http://www.itu.dk/courses/SIAS/E2005/AU2240 01.pdf, 2004.

[13] A. K. Jain, R. Bolle, and S. Pankanti, *Personal Identification in networked society*, 2nd edition. Kluwer Academic Publisher, E.U.A., 1999.

[14] A. K. Jain, A.Ross, and S. Prabhakar, "An introduction to biometric recognition," *IEEE Transactions on Circuits and Systems for Video Technology*, vol. 14, no. 1, pp. 4–19, January 2004.

[15] S. Liu and M. Silverman, "A practical guide to biometric security technology," *IT Professional*, vol. 3, no 1, pp. 27–32, January 2001.

[16] Biometrics and the courts, http://ctl.ncsc.dni.us/biomet%20web/BMIndex.html, 2010.

[17] Idesia's Biometric Technologies. Biometric comparison table, http://www.idesia-biometrics.com/technology/biometric_comparison_table.html, 2010.

[18] International Biometric Group, "Which is the best biometric technology?," http://www.biometricgroup.com/reports/public/reports/best_biometric.html, 2010.

[19] J. D. Woodward, K. W. Webb, E. M. Newton, M. A. Bradley, D. Rubenson, K. Larson, J. Lilly, K. Smythe, B. Houghton, H. A. Pincus, J. Schachter, and P. Steinberg, "Army Biometric Applications - Identifying and Addressing Socio-Cultural Concerns," Rand Corporation, Santa Monica, 2001.

[20] A. K. Khurana, *Comprehensive Ophthalmology*, New Age International (P) Ltd., 4th edition, 2007.

[21] L. A. Remington, *Clinical Anatomy of the Visual System*, Elsevier Inc., 2nd edition, 2005.

[22] J. G. Daugman, "High confidence visual recognition of persons by a test of statistical independence," *IEEE Transactions on Pattern Analysis and Machine Intelligence*, vol. 25, no. 11, pp. 1148–1161, November 1993.

[23] W. W. Boles and B. Boashash, "A human identification technique using images of the iris and wavelet transform," *IEEE Transactions on Signal Processing*, vol. 46, no. 4, pp. 1185–1188, April 1998.

[24] R. P. Wildes, "Iris recognition: an emerging biometric technology," *Proceedings of the IEEE*, vol. 85, no.9, pp. 1348–1363, U.S.A., September 1997.

[25] K. Nishino and S. K. Nayar, "Eyes for relighting," *ACM Trans. Graph.*, vol 23, no. 3, pp. 704–711, 2004.

[26] T.A. Camus and R. Wildes, "Reliable and fast eye finding in close-up images," *Proceedings of the IEEE 16th International Conference on Pattern Recognition*, pp. 389–394, Quebec, August 2002.

[27] D. Martin-Roche, C. Sanchez-Avila, and R. Sanchez-Reillo, "Iris recognition for biometric identification using dyadic wavelet transform zero-crossing," *IEEE Aerospace and Electronic Systems Magazine*, Mag. 17, no. 10, pp. 3–6, 2002.

[28] J. Cui, Y. Wang, T. Tan, L. Ma, and Z. Sun, "A fast and robust iris localization method based on texture segmentation," *Proceedings of the SPIE Defense and Security Symposium*, vol. 5404, pp. 401–408, August 2004.

[29] J. Huang, Y. Wang, T. Tan, and J. Cui, "A new iris segmentation method for recognition," *Proceedings of the 17th International Conference on Pattern Recognition* (*ICPR*), vol. 3, pp. 23–26, 2004.

[30] W. K. Kong and D. Zhang, "Accurate iris segmentation method based on novel reflection and eyelash detection model," *Proceedings of the International Symposium on Intelligent Multimedia, Video and Speech Processing*, pp. 263–266, Hong Kong, May 2001.

[31] L. Ma, Y. Wang, and T. Tan, "Iris recognition using circular symmetric filters," *Proceedings of the 25th International Conference on Pattern Recognition*, vol. 2, pp. 414–417, Quebec, August 2002.

[32] L. Ma, T. Tan, Y. Wang, and D. Zhang, "Personal identification based on iris texture analysis," *IEEE Transactions on Pattern Analysis and Machine Intelligence*, vol. 25, no. 12, pp. 2519–2533, December 2003.

[33] L. Ma, Y. Wang, and D. Zhang, "Efficient iris recognition by characterizing key local variations," *IEEE Transactions on Image Processing*, vol. 13, no. 6, pp. 739–750, June 2004.

[34] L. Liam, A. Chekima, L. Fan, and J. Dargham, "Iris recognition using self organizing neural network," *Proceedings of the IEEE Student Conference on Research and Developing Systems*, pp. 169–172, Malasya, June 2002.

[35] Y. Du, R. Ives, D. Etter, T. Welch, and C. Chang, "A new approach to iris pattern recognition," *Proceedings of the SPIE European Symposium on Optics/Photonics in Defence and Security*, vol. 5612, pp. 104–116, October 2004.

[36] J. Mira and J. Mayer, "Image feature extraction for application of biometric identification of iris - a morphological approach," *Proceedings of the 16th Brazilian Symposium on Computer Graphics and Image Processing*, pp. 391–398, Brazil, October 2003.

[37] J. Kim, S. Cho, and J. Choi, "Iris recognition using wavelet features," *Kluwer Academic Publishers, Journal of VLSI Signal Processing*, no. 38, pp. 147– 256, November 2004.

[38] A. P. Dempster, N. Laird, and D. Rubin, "Maximum likelyhood from incomplete data via the EM algorithm," *Journal of the Royal Statistic Society*, vol. 39, pp. 1–38, 1977.

[39] L. Ma, Y. Wang, and T. Tan, "Iris recognition based on multichannel Gabor filtering," Proceedings *of the 5th Asian Conference on Computer Vision*, pp. 279–283, Melbourne, Australia, January 2002.

[40] J. Ali and A. Hassanien, "An iris recognition system to enhance e-security environment based on wavelet theory," *Advanced Modeling and Optimization*, vol. 5, no. 2, pp. 93–104, 2003.

[41] L. Ma, T. Tan, Y. Wang, and D. Zhang, "Personal identification based on iris texture analysis," *IEEE Transactions on Pattern Analysis and Machine Intelligence*, vol. 25, no. 12, pp. 2519–2533, December 2003.

[42] S. Lim, K. Lee, O. Byeon, and T. Kim, "Efficient iris recognition through the improvement of feature vector and classifier," *ETRI Journal*, vol. 23, no. 2, pp. 61–70, June 2001.

[43] Y. Huang, S. Luo, and E. Chen, "An efficient iris recognition system," *Proceedings of the First International Conference on Machine Learning and Cybernetics*, pp. 450–454, China, November 2002.

[44] A. Muron, P. Kois, and J. Pospisil, "Identification of persons by means of the fourier spectra of the optical transmission binary models of the human irises," *Optics Communications*, vol. 192, no. 3, pp. 161–167, June 2001.

[45] K. Nam, K. Yoon, J. Bark, and W Yang, "A feature extraction method for binary iris code construction," *Proceedings of the 2nd International Conference on Information Technology for Application*, pp. 284–288, China, January 2004.

[46] C. Tisse, L. Martin, L. Torres, and M. Robert, "Person identification technique using human iris recognition," *Proceedings of the 25th International Conference on Vision Interface*, pp. 294–299, Calgary, July 2002.

[47] Y. Huang, S. Luo, and E. Chen, "An efficient iris recognition system," *Proceedings of the 1st International Conference on Machine Learning and Cybernetics*, pp. 450–454, China, November 2002.

[48] L. Ma, T. Tan, D. Zhang, and Y. Wang, "Local intensity variation analysis for iris recognition," *Pattern recognition*, vol. 37, no. 6, pp. 1287–1298, 2004.

[49] J. Ernst, Iris recognition homepage, http://iris-recognition.org, 2010.

[50] N. J. Ritter and J. R. Cooper, "Locating the iris: A first step to registration and identification," *Proceedings of 9th International Conference on Signal and Image Processing*, pp. 507-512, Aug. 2003.

[51] C. Li, C. Xu, C. Gui, and M. D. Fox, "Level Set Evolution Without Re-initialization: A New Variational Formulation," *IEEE Computer Society Conference on Computer Vision and Pattern Recognition*, vol. 1, pp. 430 – 436, 2005.

[52] D. Field, "Relations between the statistics of natural images and the response properties of cortical cells," *Journal of the Optical Society of America*, 1987.

[53] P. Burt, E. Adelson, "The Laplacian pyramid as a compact image code," *IEEE Transactions on Communications*, vol. 31, no. 4, pp. 532-540, 1983.

[54] Y. Zhu, T. Tan, Y. Wang, "Biometric personal identification based on iris patterns," *Proceedings of the 15th International Conference on Pattern Recognition*, Spain, vol. 2, 2000.

[55] Institute of Automation, Chinese Academy of Sciences, CASIA iris image database, http://www.sinobiometrics.com, 2010.

[56] K. Hollingsworth, K. W. Bowyer, P. J. Flynn, "Pupil dilation degrades iris biometric performance," *Computer Vision and Image Understanding*, vol. 113, pp. 150-157, 2009.

[57] L. Masek and P. Kovesi, MATLAB source code for a biometric identification system based on iris patterns, The University of Western Australia, http://www.csse.uwa.edu.au/~pk/studentprojects/libor/, 2003.

[58] A.N. Al-Raisi and A.M. Al-Khouri, "Iris recognition and the challenge of homeland and border control security in UAE," *Telematics and Informatics*, vol. 25, pp. 117–132, 2008.

[59] K. Hollingsworth, K. W. Bowyer, and P. J. Flynn, "The importance of small pupils: a study of how pupil dilation affects iris biometrics," *Proceedings of the 2nd IEEE International conference on Biometrics: Theory, Applications, and Systems*, pp. 1-6, September 2008.